Optoretinography for the Functional Assessment of the Human Retina in Health and Disease

Teng Liu

A dissertation

submitted in partial fulfillment of the

requirements for the degree of

Doctor of Philosophy

University of Washington

2025

Reading Committee:

Ramkumar Sabesan, Chair

Ivan Pelivanov

Jennifer R. Chao

Program Authorized to Offer Degree:

Bioengineering

©Copyright 2025

Teng Liu

University of Washington

Abstract

Optoretinography for the Functional Assessment of the Human Retina in Health and Disease

Teng Liu

Chair of the Supervisory Committee:

Ramkumar Sabesan

Department of Ophthalmology and Department of Bioengineering

Imaging retinal structure and function is crucial for detecting and diagnosing disease, guiding treatment strategies, and ultimately improving patient outcomes. Optoretinography (ORG) is an emerging paradigm capable of quantifying the light-evoked, nanometer-scale deformations of photoreceptors and offers a powerful, objective biomarker for retinal function. This dissertation introduces coarse-scale ORG (CoORG), an extended-field, line-scan OCT platform with high speed and phase sensitivity suitable for imaging retinal structure and function in a range of diseases. Normative data from healthy eyes reveal that cone ORG amplitude increases with retinal photon density and scales linearly with cone outer segment length. In healthy aging, ORG amplitudes decline, and the structure-function correction weakens compared to younger controls. Additionally, novel multi-layer ORG analyses extend the paradigm beyond photoreceptors and provide deeper physiological insight into outer retinal function. In patients with inherited retinal dystrophies (IRDs), ORG detects cone dysfunction even in areas with normal retinal structure and enables

significantly greater sensitivity in monitoring longitudinal progression over conventional clinical imaging. Overall, this dissertation demonstrates the potential of ORG as a rapid, sensitive, patient-friendly biomarker for disease progression and outcome measure for clinical trials.

TABLE OF CONTENTS

LIST OF FIGURES v

LIST OF TABLES xiii

ACKNOWLEDGEMENTS xiv

Chapter 1. Background 1

1.1 Retinal imaging of structure and function 1

1.1.1 Structural imaging modalities 1

1.1.2 Functional testing modalities 3

1.2 Clinical need for objective functional biomarkers 4

1.3 An overview of Optoretinography (ORG) 6

1.4 Rationale of ORG in human retina 8

1.4.1 Phase-based ORG 9

1.4.2 Intensity-based ORG 13

1.4.3 Cellular-scale ORG with adaptive optics (AO) 14

Chapter 2. Coarse-scale optoretinography (CoORG): system design, experiment protocol, and data workflow 16

2.1 Optical coherence tomography for structural and functional imaging 16

2.1.1 Axial resolution and coherence gating 18

2.1.2 Lateral resolution and depth of focus 20

2.2 Phase-resolved OCT modalities 22

2.2.1 Point-scan OCT 23

2.2.2 Full-field OCT 24

2.2.3 Line-scan OCT (chosen architecture) 26

2.3 Rationale for the CoORG platform 30

2.4 Coarse-scale optoretinography (CoORG): extended-field, line-scan OCT 31

2.5 System calibration 34

2.5.1 System optical alignment 34

2.5.2 Laser power (imaging beam) calibration 34
2.5.3 Stimulation calibration 35
2.6 Experimental protocol 37
2.7 Data processing pipeline 40
2.7.1 Segmentation and registration 40
2.7.2 Refined COST-band segmentation 40
2.8 Digital aberration correction (DAC) pipeline 41
2.8.1 Algorithm and validation on synthetic data 42
2.8.2 Performance on AO-OCT data 44
2.8.3 DAC performance on in-focus foveal AO-OCT images 46
2.8.4 Digital correction in CoORG datasets 47
2.8.5 Current limitations and future refinements 49
Chapter 3. Normative characterization of the ORG using CoORG system 51
3.1 Introduction 51
3.2 CoORG cross-sectional B-scan images 51
3.3 ORG trial-to-trial repeatability 52
3.4 ORG variability across retinal meridians 54
3.5 The comparison between CoORG and AO-based ORG 55
3.6 Inter-individual variation in ORG 56
3.6.1 Variation of ORG with photon density 58
3.6.2 Variation of ORG with outer segment (OS) length 59
3.6.3 Variation of ORG across different nominal photon densities 60
3.7 Summary of the key factors in the cone ORG 62
3.8 ORG as a function of age 64
3.8.1 ORG response reduces with age 65
3.8.2 Summary of age-related decrease of ORG response 69
Chapter 4. Multi-layer ORGs in the human outer retina 72
4.1 Introduction 72
4.2 Method 74
4.2.1 Study participants 74

4.2.2 ORG imaging systems with AO/non-AO modes 74
4.2.3 Protocol and analysis 75
4.3 Results 76
4.3.1 The categories of ORGs among different outer retinal layers 76
4.3.2 ORGs across eccentricities 78
4.3.3 Kinetics among α, β, and γ ORGs 79
4.3.4 ELM – RPE response analysis at the cellular scale using AO-ORG 81
4.3.5 Evidence for absolute movement direction between ELM/RPE layers 84
4.3.6 Modeling the ELM displacement near the fovea 89
4.3.7 Comprehensive characterization of γORG (ISOS - RPE) 91
4.3.8 Comprehensive characterization of αORG (ISOS – COST) 94
4.4 Discussion 96
Chapter 5. ORG characterization in retinitis pigmentosa (RP): functional assessment and longitudinal monitoring 99
5.1 Introduction 99
5.2 ORG in RP 99
5.2.1 The structure and function in RP 102
5.2.2 The ORG amplitudes in whole RP patients across eccentricities 104
5.2.3 Overlaying function on structure at different stages 106
5.3 An ORG longitudinal study of RP 107
5.3.1 Study participants 108
5.3.2 ORG in RP: protocol and analysis 111
5.3.3 Test-retest variability and statistical analysis 112
5.3.4 Follow-up results in ORG 113
5.3.5 Discussion 125
5.4 Multi-layer applications in RP 130
Chapter 6. ORG in Acute zonal outer occult retinopathy (AZOOR) patient with advanced scotoma 134
6.1 Introduction 134
6.2 Clinical background and study outline 135

6.3 Multimodal structural findings in an advanced-scotoma AZOOR eye 135
6.4 Functional assessments with ORG 138
Chapter 7. Conclusions and future work 142
BIBLIOGRAPHY 147

LIST OF FIGURES

Figure 1.1 Illustration of the phase difference across the cone outer segment. Red and blue rays (and their corresponding waveforms) represent the back-reflected optical phase from the inner/outer segment junction (IS/OS) and the cone outer-segment tips (COST), respectively, while the pink waveform depicts the differential phase between these two layers. 11
Figure 1.2 A typical ORG response vs. time. Change in optical path length (ΔOPL) between ISOS and COST as a function of time following a 5 ms, 528 ± 5 nm flash (green bar at $t = 0$). Data were acquired for 1.18 s at 20 Hz. 12
Figure 2.1 Different imaging modes: (A) point-scan OCT; (B) line-scan OCT; (C) full-field OCT. The single acquisitions in each exposure are labelled as the red dot, red line, and red rectangle shown in (A) – (C), respectively. 22
Figure 2.2 Schematic of line-scan imaging using a 2D camera. Raw data are acquired as a three-dimensional cube whose axes correspond to the line-illumination direction (fast axis), the slow scan dimension, and axial depth. A single exposure of the 2-D camera captures the interferometric fringe pattern for one line, yielding an instantaneous B-scan interferogram. Fourier reconstruction of each interferogram produces a structural B-scan, and sequential B-scans are stacked to form a volumetric dataset in which the principal retinal layers, summarized here as inner versus outer retina, are delineated. 29
Figure 2.3 CoORG system layout. The layout is not drawn to scale, and the beam follows the general path on the optical table. The beam is shown along one dimension in illumination where the linear field is focused on the pupil planes. The orthogonal view is not shown. The beam path in detection corresponds to the case where a mirror is placed at the eye's pupil. L: spherical lens, CL: cylindrical lens, M: mirror, GS: galvo scanner, BS: beam splitter, DG: dispersion compensation glass window, LSO: line-scan ophthalmoscope, OCT: optical coherence tomography, P: pupil plane, R: retinal plane, LED: light-emitting diode. 33
Figure 2.4 The relationship between pupil diameter and stimulated beam size on retina plane and measured power. The linear fit and polynomial fit are displayed in the plots. 37
Figure 2.5 Experimental flow. (A) Axial length was measured by Zeiss IOLMaster. (B) Clinical SLO and OCT were taken for registration and finding the foveola. (C) Pupil image was taken for measuring the pupil size. (D) CoORG system B-scan example. (E) Green circle shows the circular stimulus field. ORGs were extracted in annular ROI shown as superimposed on the stimulus field, the registered IS/OS *en face* image and clinical SLO image. The red asteroid indicates the center of the fovea. 39
Figure 2.6 Detection of the IS/OS junction and COST layer. In each sub-region, 100 compressed B-frames are overlaid, with their mean profile highlighted by a red curve (a). A moving-window peak-finding algorithm can be applied to improve layer localization, generating depth maps for the IS/OS junction (b) and the COST layer (c). En-face projections of the detected IS/OS (d) and COST (e) layers span the entire field of view. 41

Figure 2.7 Accuracy benchmark of the hybrid optimizer on an artificial dataset. (A) Synthetic object (“E”), ground-truth Zernike phase map, and the correspondingly blurred (aberrated) image. (B) Same triplet after optimization: recovered Zernike map and aberration-corrected image are virtually identical to the ground truth. (C) Convergence curve for the EPSO stage; RMSE after this global search is 7.0×10^{-4}. (D) Convergence curve for the subsequent SD stage; RMSE falls to 2.7×10^{-17}, confirming near-perfect phase retrieval. 43
Figure 2.8 Optimization procedure and results for the IS/OS layer in AO-OCT images. (a) The raw AO-OCT image stack was segmented axially into three distinct depth layers: upper, central, and bottom. (b) Each depth layer underwent independent optimization. (c–d) Maximum intensity projections (MIPs) were calculated from optimized sub-regions, each sized 128×128 pixels. (e) The entire imaging field measures 512×512 pixels, divided into 16 sub-regions (g). Optimization was thus performed separately for each of these 16 sub-regions. (f) Final composite image obtained after combining individually optimized sub-regions, demonstrating overall enhancement in image quality. 45
Figure 2.9 Raw (left) and digitally corrected (right) en-face IS/OS projections from a 1.43° AO-OCT volume. Dashed boxes (1–3, 0.20°) mark sub-regions shown enlarged above and below: blue = before correction, red = after. Cone photoreceptors are visibly sharpened, and inter-cone dark spaces deepen after DAC. Optimization used 65 Zernike modes on 128 × 128 tiles, confirming that software correction enhances even hardware-focused, central-fovea images. ... 47
Figure 2.10Digital aberration correction applied to CoORG data. (a) Raw e*n-face* projection with four ROIs (blue dashed boxes) at eccentricities spanning 1.1–2.5°; (b) projection after 36-term Zernike DAC, ROIs indicated in red; (c) side-by-side zooms (before, blue; after, red) for ROIs 1–4 illustrate the emergence of the cone mosaic post-correction (arrows highlight representative cones). Scale bar for insets: 0.20°. 49
Figure 3.1 Example of a B-scan acquired from the CoORG instrument. Eccentricities are indicated on the B-scan shown in (A), and the corresponding intensity profiles along the A-scan are shown in (B). The peaks correspond to the major outer retinal layers shown in the black arrows. 52
Figure 3.2 Light-evoked ΔOPL for a subject along the temporal meridian. Column A and column B show plots of 5 successive repeat trials at different eccentricities for high and low bleach levels, respectively where each curve represents a single trial. The high and low bleach correspond to 8.8×10^{6} and 4.4×10^{6} photons/μm^2 respectively for this subject. Plot C and D are the mean of the five repeat measurements for both bleach levels at each eccentricity. The shaded area surrounding the solid traces represent ±1 standard deviation. 54
Figure 3.3 Comparison of ΔOPL changes versus eccentricity for inferior and temporal meridians. 55
Figure 3.4 Comparison with AO and with CoORG in the same subjects S1 & S2 is shown in (A). (B) En face overlaying image of CoORG, AO-ORG, and AOSLO to facilitate alignment between them. The size of the red square is 0.3×0.3 deg^2. 56

Figure 3.5 Box and whisker scatter plots with averaged maximum ΔOPL from 12 subjects for high (A) and low (B) bleach levels. One subject's OPL was significantly lower than others (pink left triangle), due to a smaller pupil size and longer axial length translating effectively to a lower photon density on the retina. 57
Figure 3.6 The variation in maximum saturated ΔOPL vs. eccentricity for different photon density bins calculated specific to each subject. Data points are the mean in each bin, and error bars represent ± 1 standard deviation. 58
Figure 3.7 The variation in maximum saturated ΔOPL versus outer segment length for high (A) and low (B) bleach strengths. Each data point indicates measurement from a single subject & eccentricity, while markers and colors indicate different eccentricity bins. A linear regression fit to all data is shown in both plots, along with the coefficient of determination and the equation for the linear fit. 59
Figure 3.8 Relationship between retinal photon density and maximum cone ORG amplitude. Scatter plot of photon density at the x-axis versus max ΔOPL for 0.5° FOV interval recorded at eccentricities from 0.5° (yellow squares) to 5° (black pentagons); marker colors transition from yellow to violet with increasing eccentricity, as indicated in the legend. 60
Figure 3.9 Linear scaling of saturated ORG amplitude with cone OS length. Maximum optical path length change (max ΔOPL) plotted against measured OSL for three photon-density conditions: low (light green), middle (olive), and high (dark green). 62
Figure 3.10 Schematic summary of factors that shape the normal variability of the cone ORG. Pre-photoreceptor influences (left) govern the photon density reaching the retina: panel A illustrates how flash intensity, pulse duration (Δt) and spectral bandwidth (Δλ) and central wavelength (e.g., λ_0 = 528 nm) jointly define the incident photon dose, while panel B shows anterior-eye optics in which pupil size, axial length (q) and age- or cataract-related lens transmittance modulate that dose. Panel C plots represent ΔOPL traces from a control eye (blue) and a cataractous eye (red), demonstrating the amplitude reduction caused by diminished lens transmission. Photoreceptor-intrinsic factors (right) further modulate the response: panel D depicts eccentricity-dependent changes in cone morphology, notably shorter outer-segment (OS) lengths, and optical phenomena such as waveguide condensation and the Stiles–Crawford effect; together these structural and optical gradients influence both the fast mechanical and slower osmotic components of the ORG. 64
Figure 3.11 Effect of age on the relationship between ORG amplitude and OS length. Scatter plots comparing ORG amplitude (max ΔOPL) against photoreceptor OS length for two age groups—participants 20- 49 years (dark green squares, sample sizes indicated) and older than 50 years (light green circles)—in three stimulus conditions : (A) 4.4 × 10^6 photons/μm², (B) 8.8 × 10^6 photons/μm², and (C) 14.2 × 10^6 photons/μm² nominal retinal photon density. Solid lines represent linear fits for each group. 66
Figure 3.12 Impact of healthy aging on cone structure and ORG response. Left: Mean cone-density profiles versus eccentricity for the aging cohort (light-green circles, age range: > 50 years old) and the younger control group (dark-green squares, age range: 20 – 50 years old). Shaded

regions represent ±1 SD. Both groups show the expected decline in density with distance from the fovea, while the aging eyes exhibit a consistent downward offset across the parafoveal band. Right: Scatter-plot of ORG amplitude (max ΔOPL) versus OS length (eccentricity range: 1° to 5°) at the lowest nominal photon density stimulus condition (4.4×10^6 photons/μm²); solid lines are linear fits for each cohort. 68
Figure 4.1 Schematic representation of different ORG responses. (A) shows an example B-scan from the CoORG system with the outer retinal layers: external limiting membrane (ELM), inner segment/outer segment junction (ISOS), cone outer segment tips (COST), and retinal pigment epithelium (RPE) marked by green arrows, alongside the average A-line profile on the right. (B) illustrates the various ORG responses derived from differences between specific retinal layers: α ORG (ISOS–COST), β ORG (COST–RPE), γ ORG (ISOS–RPE), ε ORG (ELM–ISOS), and δ ORG (ELM–RPE). (C) presents representative ORG traces over time, highlighting how these signals evolve within each corresponding layer boundary. 77
Figure 4.2 (A) ISOS *en face* image extending from the central fovea out to 5° eccentricity. The dashed white circles indicate eccentricities binned at 0.5° intervals. (B) Saturated ORG amplitudes plotted as a function of eccentricity (0.25° to 5°) for α ORG (orange), β ORG (pink), γ ORG (light purple), ε ORG (dark purple), and δ ORG (cyan). (C) Comparison of the sum α ORG + β ORG (purple dash-dot line) with γ ORG (solid purple line), and the sum γ ORG + ε ORG (green dash-dot line) with δ ORG (solid green line), illustrating how these individual layer responses relate to one another. 79
Figure 4.3 The kinetics analysis among α, β, and γ ORGs. (A) The rate of change of the ΔOPL as a function of eccentricity for α ORG (ISOS–COST), β ORG (COST–RPE), and γ ORG (ISOS–RPE). Error bars represent ±1 standard deviation. (B) The purple dash-dot line indicates the sum (α ORG + β ORG), while the solid purple line shows γ ORG, allowing direct comparison of their maximum rates of change. 80
Figure 4.4 Adaptive Optics-based ORG (AO-ORG) near the fovea to assess the residual δ ORG amplitude. (A) En face SLO image from a commercial OCT, where the red and blue rectangles indicate the 0.5° temporal and 4° nasal eccentricities, respectively. (B) and (C) illustrate the spatial distribution of the saturated δ ORG amplitude at single-cone resolution, overlaid on the ISOS/COST MIP en face image for each location. The color scale indicates the saturated ΔOPL at individual cones, with 10 nm increments per bin. (D) A bar plot of the mean δ ORG amplitude compares the two regions, indicating a significant difference between them. 82
Figure 4.5 AO-based ORG with cone classification, featuring (A) a maximum intensity projection (MIP) of the ISOS/COST interface in a selected region of interest (ROI) and (B) the corresponding cone mosaic and distribution. In (C1), time-resolved α ORG traces are shown for L-, M-, and S-cones, with shaded regions indicating ±1 standard deviation, while (C2) presents the corresponding saturated α ORG amplitudes by cone type. Panels (D1) and (D2) illustrate the time-resolved δ ORG traces and their associated amplitude bar plots, respectively. 83
Figure 4.6 An auxiliary demonstration of RPE movement. (A) An exemplary A-line profile, where the dashed arrow indicates the BrM layer within the indistinguishable RPE–BrM complex.

(B) Time-resolved δ ORG traces across eccentricities ranging from 0.25° to 5° for a typical single subject. (C) and (D) show the ORG responses for ELM–BrM and RPE–BrM, respectively, as a function of eccentricity. For comparison, (E) presents a non-stimulus RPE–BrM response, with a consistent legend applied to all four panels. 86
Figure 4.7 Mechanical movement of distinct retinal layers after light-evoked activity. (A) A color-coded amplitude map overlaid on a representative OCT B-scan, illustrating how the movement amplitude transitions from central fovea (red- larger movement) to peripheries (green-smaller movement). In peripheral regions, the ELM and RPE remain relatively stable with minimal displacement. However, within approximately 1.5° of the fovea, there is a pronounced elongation between the ELM and RPE, while the COST displaces downward substantially, and the ISOS shifts upward more mildly. (B) & (C) Plots depicting these displacements in more detail, confirming that the near-foveal region exhibits significantly greater mechanical movement than the retinal periphery, particularly in ELM layer. 88
Figure 4.8 Comprehensive characterization of the γ ORG, showing repeatability, stimulus sensitivity, eccentricity dependence, and structure–function relationships. (A) presents representative γ ORG traces recorded at eccentricities ranging from 0.25° to 3.5°, while (B) shows box-and-whisker plots of γ ORG amplitudes from 10 subjects across 0.25° to 5°. In (C), γ ORG traces acquired at varying photon densities, measured at 5° temporal eccentricity, illustrate stimulus-dependent responses, and the corresponding relationship between saturated γ ORG amplitude and photon density is plotted in (D). Finally, (E) displays the structure–function correlation between saturated γ ORG amplitude and outer retinal thickness (ORT), with a linear fit shown in red. 93
Figure 4.9 Corresponding cone (α, ISOS - COST) ORG characterizations. Comprehensive characterization of the α ORG, showing repeatability, stimulus sensitivity, eccentricity dependence, and structure–function relationships. (A) presents representative α ORG traces recorded at eccentricities ranging from 0.25° to 3.5°, while (B) shows box-and-whisker plots of α ORG amplitudes from 10 subjects across 0.25° to 5°. In (C), α ORG traces acquired at varying photon densities, measured at 5° temporal eccentricity, illustrate stimulus-dependent responses, and the corresponding relationship between saturated α ORG amplitude and photon density is plotted in (D). Finally, (E) displays the structure–function correlation between saturated γ ORG amplitude and outer segment length, with a linear fit shown in red. 95
Figure 5.1 A typical RP patients' structural and control's image and corresponding ORG traces. (A) & (B) The IS/OS structural en *face* image of a normal subject and an RP patient. (C) The ORG traces between RP & control in same eccentricities (0.5° & 1.5°, respectively). The annuli expand in increments of 0.5 degrees centered at the fovea. 103
Figure 5.2 Plot of saturated ΔOPL vs. eccentricities ranging from 0.5° to 3° across seven RP patients and controls (n=8). The panel below shows the TZ onset, indicating the start of the transition zone in each patient. An arrow signifies that the range extends beyond 5° eccentricity. The purple left triangle RHO is RP05-RHO patient. 105

Figure 5.3 Scatter plot of maximum ΔOPL for control cones (green squares), Stage I (light-blue circles) and Stage II (dark-blue triangles) RP patients. Solid and dashed regression lines give group SF-slopes of 29.2, 17.6*, and 7.7* nm/μm, respectively (*p < 0.05 versus control; ANCOVA). The progressive flattening of the SF-slope illustrates the loss of length-dependent ORG gain with advancing disease. 107
Figure 5.4 Overview of study design, illustrating the advanced structure-function assessment. OCT volumes along with the segmented en face image at the inner/outer segment-ellipsoid zone (ISOS-EZ) and outer segment tips (COST) help visualize the retinal structure (A). A zoomed-in view of OCT B-scans provides the outer retinal profile (red line) from which the OS length is obtained and plotted as a function of eccentricity in a color map (B). Warmer and cooler colors represent longer and shorter OS lengths respectively. Retinal function is assessed by measuring the change in outer segment optical path length (ΔOPL) evoked by a light stimulus (shaded green) – denoted as the ORG amplitude (D). The saturated ORG amplitude is obtained from the time evolution of the functional response, shown in (D) for a near-foveal (gray) and parafoveal (black) retinal location. The shaded areas around the solid lines indicate the standard-deviation of repeat measurements. The variation of the saturated ORG is plotted as a function of eccentricity in a color map (E). Test-retest (left) and Bland-Altman analysis (right) shows high repeatability for both OS length (C) and ORG (F). Red line is the y=x identity line. Data points in (C) and (F) represent measurements (ORG or OS length) from same retinal locations of size 0.25° × 0.25° in the same subject taken 6 months apart.....110
Figure 5.5 Example longitudinal study analysis pipeline for RP01. (A) Clinical OCT B-scans from baseline (top) and follow-up (bottom) visit. Red arrows indicate the fovea. Red & yellow dashed lines mark the EZ width boundaries at baseline and follow-up respectively. (B) Fundus autofluorescence (FAF) from baseline (top) and follow-up (bottom) visit. The white dashed ellipse outlines the EZ area, while the blue rectangle marks the region selected for further OCT-ORG analysis. (C) En face images for baseline (top) and follow-up (bottom), with the corresponding EZ area from (B) marked as a white dashed ellipse. The yellow ellipse highlights the area chosen for OSL and ORG analysis, based on the preservation of all outer retinal layers. Maps of (D) OS length and (E) ORG amplitude are shown for baseline (top) and follow-up (bottom). The difference maps between the follow-up visits are displayed for OS length and ORG. An outline (yellow) is drawn in all OS length and ORG maps, as reference for comparison between baseline and follow-up visits. The scale bar in (D-E) is 200 μm. 115
Figure 5.6 Longitudinal follow-up in RP03, RP04, and RP05, displaying the progression from the initial baseline visit to the most recent follow-up. (A) Baseline and follow-up *en face* images at the ISOS-EZ band and the corresponding ROIs (red) selected for OS length and ORG analysis. Maps of OS length and ORG are shown in (B) and (C) respectively. Their corresponding color bars denote the variation in OS length and ORG response amplitude. The difference maps between the follow-up visits for OS length and ORG are shown for each patient. Yellow dashed lines and arrows indicate the same location for reference across follow-up visits. The scale bar is 200 μm. 119

Figure 5.7 Quantification of RP disease progression. (A) The ORG maps are divided into regions-of-interest (ROIs) (white circles) to allow regional comparison of photoreceptor dysfunction. ORGedge and ORGcent are derived as the mean of 10 ROIs in the border region surrounding the structurally intact central island and the central region, respectively, while ORGtot is obtained as the mean of 17 ROIs across the entire ORG map. The fovea is indicated by a red star. (B) Comparison of regional metrics derived from ORG, including ORGtot, ORGedge, and ORGcent (C) The corresponding metrics for OS length, including OSLtot, OSLedge, and OSLcent are shown. The colors of legend in (B) & (C) are identical, representing the center, total, edge regions respectively in each subject. Error bars in (B) & (C) represent the standard deviation of values obtained from the different ROIs (10 ROIs each for center and edge, 17 ROIs for total). (D) Scatter and bar plots show the progression of ORGedge amplitude over time. The different colors represent baseline, first and second follow-up visits, respectively. Connecting lines illustrate ORGedge changes for the same location across the different follow-ups. 121
Figure 5.8 Comparison of different biomarkers for measuring RP disease progression. Percent reduction in ORG, OS length, and EZ-width between baseline and the latest follow-up visit for the five RP patients is shown. The ORG and OSL values are those obtained from the edge of the central island, ORGedge and OSL*edge* respectively. Statistical significance values obtained from the Wilcoxon signed-rank test are noted. Error bars for ORG & OS length represent the standard deviation of values obtained from different ROIs (10 ROIs each for ORG*edge* and OSL*edge)*. For EZ-width, the error bar represents the standard deviation of repeat measurements from three independent graders. 123
Figure 5.9 Defining ORG*edge*, TZ*start* and TZ*end* in the OCT A-scans and B-scans. The ORGedge is defined as the most peripheral retinal location where all three outer retinal bands are intact in the CoORG system. The TZstart is defined as the location in Heidelberg OCT B-scan where the COST reflection is absent while ISOS-EZ and RPE bands are visible. The TZend is defined as the location in Heidelberg OCT B-scan where only the RPE band is visible. 125
Figure 5.10 Clinical application of the γ ORG in RP patients. (A) Illustrates the definition of healthy zone (HZ), transition zone (TZ), and diseased zone (DZ) based on a representative A-line profile and an ISOS *en face* image, where the yellow dashed circle denotes the boundary of HZ at approximately 1.4deg in the temporal meridian (blue dash vertical line). (B) Shows the corresponding γ ORG traces, with blue bins indicating the HZ and red bins the TZ. (C) Compares the saturated γ ORG amplitudes in the HZ of RP patients versus matched eccentricities in controls, while (D) presents box-and-whisker plots highlighting differences in both the HZ and TZ between RP patients and normal subjects. 132
Figure 6.1 Multimodal structural images of the AZOOR patient, (A) fundus autofluorescence (FAF), (B) scanning laser ophthalmoscopy (SLO), and (C) OCT B-scan acquired along the blue dashed line in (B). Panel (D) shows an AOSLO cone photoreceptor montage spanning the central 6°. (E) zoomed-in foveal AOSLO images corresponding to the red dashed rectangle in (D), where both confocal reflectance and non-confocal split-detector (phase-contrast) images are

shown. In the split-detector image, circular structures corresponding to putative inner segments are visible, where corresponding confocal images show ambiguous reflections (E, yellow arrows). 137
Figure 6.2 Functional characterization of the AZOOR patient. (A) MAIA microperimetry sensitivity map. (B) adaptive optics microperimetry (AOMP), where three orange crosses mark test locations within the central island and four dark purple crosses indicate locations outside the island (DNS: “did not see”). (C) ORG traces, represented as the change in OS length over time (optical path length, ΔOPL) in a normal control & AZOOR patient for ROIs corresponding to the locations in (B). The rightmost panel is a zoomed-in view of the early OS contraction. In panel (C), the three distinct stages of the ORG are delineated with shading: pre-stimulus (gray), photoisomerization (blue), and phototransduction (green). (D) ORG *en face* map in same location as (B), where ORG magnitude is derived from the saturated amplitude of the last 0.3 seconds of the ORG traces in (D). 140

LIST OF TABLES

Table 2.1 System specification 34
Table 3.1 The potential factors between aging and young control 69
Table 3.2 A comprehensive summary for age-related parameters 71
Table 4.1 The parameters of cone structures between fovea and periphery 90
Table 5.1 The information of all RP patients 102
Table 5.2 Characteristics of longitudinal study participants 108
Table 5.3 Comparison of ORG and OS length between RP patients and normal controls in the central island 117
Table 5.4 Annual rate of progression, as defined by the reduction in different biomarkers 124
Table 5.5 Disease progression of patients diagnosed with RP 125

ACKNOWLEDGEMENTS

First and foremost, I owe my deepest gratitude to Dr. Ramkumar Sabesan, my PhD advisor. From my first day in Sab lab, he demonstrated what it means to practice rigorous, principled science—emphasizing careful experimental design, honest data interpretation, and clear communication. He taught me how to ask the right questions and, just as importantly, to remain open to unexpected answers. By continually encouraging me to explore alternative hypotheses and push past comfortable assumptions, Dr. Ramkumar Sabesan fostered both my independence and creativity. His patience, insightful feedback, and unwavering enthusiasm have shaped not only this dissertation but also the way I will approach scientific inquiry throughout my career.

I am equally thankful to my dissertation committee: Dr. Ivan Pelivanov, Dr. Jennifer R. Chao, Dr. Johnathan T. Liu, Dr. Mike Averkiou, for their keen questions, constructive critiques, and steadfast support. Their collective expertise broadened my perspectives and strengthened the rigor of this work.

Sincere appreciation goes to my collaborators: Dr. Debarshi Mustafi. Dr. Tong Ling, Huakun Li, whose complementary skills and generous sharing of ideas made many of the results herein possible. I also extend heartfelt thanks to every member of the Sab lab—Benjamin Wendel, Dr. Palash Bharadwaj, Dr. Vimal Prabu Pandiyan, Keyu Chen, Dr. Sierra Schleufer, Connor Weiss, Samson Darrah, Dr. Emily Slezak, Dr. Ayoub Lassoued, and Jenna Huey—for the stimulating discussions, technical assistance, and the camaraderie that made long hours in the lab genuinely enjoyable.

I also gratefully acknowledge my former advisor, Dr. Honghui He, for introducing me to research and instilling the curiosity that ultimately led me to pursue a doctorate.

I am likewise indebted to my mentors and friends, Dr. Chao He, Dr. Qinghua He, and Xin Xu, for their encouragement, wise counsel, and friendship throughout this journey.

Finally, none of this would have been possible without the unwavering love and support of my wife and parents. Their patience, sacrifice, and belief in me provided the foundation on which all of my academic pursuits have been built. To them, I dedicate this thesis with boundless gratitude.

Chapter 1. Background

1.1 Retinal imaging of structure and function

In ophthalmology, evaluation of the retina has traditionally relied on a combination of structural imaging techniques and functional tests. Structural retinal examination techniques provide direct visualization of ocular anatomy, allowing clinicians to detect morphological changes in the retina and supporting tissues. Functional assessments evaluate the performance of the visual system, and how the various stages of the visual pathways respond to stimuli. This section surveys the range of structural and functional retinal examination methods, from classic fundus photography to modern innovations, and outlines how advances in ophthalmic imaging techniques have begun to bridge the gap between structure and function in retinal imaging.

1.1.1 Structural imaging modalities

Early retinal examinations were performed with direct and indirect ophthalmoscopy[1], but the advent of photography revolutionized documentation of retinal structure. Color fundus photography[2,3], first achieved in the late 19th century and widely adopted by the mid-20th century, remains a fundamental tool for capturing retinal anatomy in vivo[4]. A single fundus photograph provides a broad view of the optic disc, macula, and retinal vessels, and it became the standard method for screening diseases like diabetic retinopathy and macular degeneration. Over the years, fundus cameras have improved in field of view and resolution, enabling increasingly detailed images of the retina[5]. Even today, conventional fundus photography is valued for its simplicity, cost-effectiveness, and diagnostic utility[5]. Its limitations, however, include a two-dimensional

representation of a three-dimensional tissue and limited ability to visualize subtle transparent structures.

To gain more detailed structural insights, especially into the retina's transparent layers, different imaging methodologies were introduced. Fluorescein angiography (FA)[6], developed by Novotny and Alvis in 1961[7], allowed dynamic imaging of the retinal circulation by injecting a fluorescent dye and photographing its transit through retinal vessels[7]. FA provided unprecedented views of the retinal vasculature and blood–retina barrier function, highlighting leaks or non-perfusion, and became a cornerstone for diagnosing vascular retinal conditions. However, it is an invasive procedure requiring dye injection and carries risks of side effects. In the 1970s–1980s, scanning laser technology brought further advancements[8,9]. The scanning laser ophthalmoscope (SLO)[10] uses a laser beam raster-scanned to form an image of the fundus, and the introduction of confocal optics by Webb and colleagues in 1987 greatly enhanced image clarity by rejecting out-of-focus light. The confocal SLO improved the visualization of fine retinal details (e.g. nerve fiber layer defects[11]) with high contrast[12]. It also facilitated new imaging modes – notably, fundus autofluorescence (FAF) imaging, which was first demonstrated in 1995 using a confocal SLO[13]. FAF captures the faint natural fluorescence emitted by lipofuscin accumulations in the retinal pigment epithelium, providing a metabolic map of retinal health[14]. By revealing regions of RPE stress or degeneration (which manifest as abnormal autofluorescence), FAF has become a noninvasive way to assess functional integrity of the outer retina in diseases such as macular degeneration[15]. Other structural imaging innovations include indocyanine green angiography[16,17] (for choroidal circulation) and ultrawide-field imaging[18,19] (capturing the peripheral retina); these have expanded our structural view of the eye. Each of these tools – fundus photography,

angiography, SLO/FAF, and others, offers unique advantages for visualizing anatomy, but they do not directly measure how well the retina functions.

1.1.2 Functional testing modalities

Because structural imaging alone cannot reveal the health of the retina, ophthalmologists also employ a battery of functional tests. The most ubiquitous is visual acuity, which measures the eye's resolving power using charts like the Snellen or LogMAR[20,21]. Visual acuity (typically reported as 20/20, 20/40 or 6/6, 6/12 etc.) is the gold-standard metric of central visual function and is critical for gauging the impact of macular diseases. However, it is a subjective test that requires the patient's cooperation. If a patient cannot understand or respond, the measurement may not reflect true retinal function. Likewise, contrast sensitivity assesses the ability to discern low-contrast patterns and can detect functional deficits not evident in high-contrast acuity; it too is subjective and influenced by cognitive factors. Perimetry (visual field testing) maps the sensitivity of the retina across the visual field, often using automated static perimeters (e.g. Humphrey field analyzer). This test is essential for detecting peripheral or generalized retinal dysfunction (for example, in glaucoma or retinitis pigmentosa). Yet, standard perimetry is also a subjective method prone to variability – patient attentiveness, learning effects, and response criteria can all affect results. High test–retest variability in visual fields is well documented, which can complicate disease monitoring [22]. Moreover, perimetry provides only a coarse spatial sampling of retinal function, typically on the order of several degrees of visual angle between test points, meaning subtle or very localized defects can be missed.

For a more objective evaluation of retinal health, clinicians use electrodiagnostic tests like the electroretinogram (ERG) [23]. The full-field ERG (also called flash ERG) measures the summed electrical response of the entire retina to a brief flash of light [24]. Pioneering work established the

ERG as an objective indicator of retinal function, independent of patient feedback [25]. In a standard ERG, a contact lens or skin electrode records retinal potentials (a-wave, b-wave, etc.) generated by photoreceptors and inner retinal cells in response to light stimuli. ERGs are invaluable for detecting diffuse retinal disorders (e.g. inherited retinal degenerations) and for separating rod vs. cone system function by using dark-adapted (scotopic) and light-adapted (photopic) test conditions. The strength of the ERG is its objectivity and sensitivity to early dysfunction. However, a conventional full-field ERG has very low spatial resolution – it reflects the global or average response of the retina. Small pathologic areas can be drowned out by signals from healthy regions; for instance, a small macular lesion might barely influence the full-field ERG. To address this limitation, the multifocal ERG was introduced by Sutter and Tran in 1992, allowing simultaneous recording of localized ERG responses from many retinal subfields [25]. The multifocal ERG (mfERG) produces a topographic map of retinal function (a typical mfERG stimulus array of 61 hexagonal elements covering ~ 50° of the central visual field) [26,27], but its spatial resolution is relatively coarse – each stimulus element aggregates signals from hundreds of photoreceptors – so subtle, highly localized dysfunction can go undetected. Other objective tests like visual evoked potentials (which measure cortical responses) are similarly limited in retinal specificity [28]. In summary, traditional functional assays either rely on subjective patient input (e.g. acuity, visual fields) or provide only a coarse, aggregate measure of retinal activity (ERG). The link between structural imagery and functional testing has long been a challenge – clinicians often infer functional status from anatomical findings or vice versa.

1.2 Clinical need for objective functional biomarkers

As discussed above, existing functional assessment methods such as perimetry and ERG are limited by their subjectivity, reliance on patient cooperation, and relatively coarse spatial

resolution. Visual acuity and perimetry tests are subjective and heavily dependent on patient cooperation, and their accuracy can be compromised when patient compliance is limited. Moreover, these conventional assessments provide relatively coarse spatial information: visual acuity primarily evaluates central vision, and perimetry generates broad maps of visual field sensitivity. With advances in high-resolution retinal imaging and precise eye-tracking, it has become possible to correlate single cone photoreceptor activity directly with visual perception [29]. Adaptive optics microperimetry (AOMP)[30] greatly improves spatial resolution, even enabling stimuli targeting at the individual-photoreceptor level, but still relies on subjective psychophysical responses, requiring substantial patient attention and cooperation. ERG offers an objective measure of retinal electrical activity but lacks fine spatial resolution; full-field ERG aggregates signals from the entire retina, and even multifocal ERG achieves far lower spatial resolution than imaging-based approaches. Additionally, ERG requires contact electrodes placed directly on the eye, making the procedure invasive and uncomfortable for patients. Conventional functional tests such as Goldmann/Humphrey perimetry and ERG typically remain within or near-normal range until the photoreceptor is already severely deleted, making them insensitive, late-stage biomarkers of the retinal degeneration [31,32]. This limitation highlights the need for an imaging modality capable of detecting early functional impairment before significant structural degeneration becomes apparent.

These limitations - subjectivity, limited spatial resolution, invasiveness, substantial patient burden, and poor localization of dysfunction at the cellular level, and “end-stage” detection - present significant barriers for early disease detection and precise retinal disease monitoring. Considering the limitations outlined above, there is a clear motivation to develop optoretinography (ORG) as an advanced functional metric that is both objective and spatially precise for assessing retinal health. In detail, ORG addresses these critical gaps by offering non-invasive, objective, and

spatially precise measurements of photoreceptor function. Using advanced optical imaging techniques such as phase-resolved OCT combined with adaptive optics, ORG maps light-induced responses from individual photoreceptors, providing cellular resolution. This approach enables accurate localization of retinal dysfunction and detection of subtle, preclinical photoreceptor deficits, without relying on subjective patient responses. Consequently, ORG has potential as a powerful functional biomarker, overcoming the limitations of traditional retinal assessment methods. The following section (1.3) provides an overview of ORG's principles and discusses its potential applications in vision research and clinical ophthalmology.

1.3 An overview of Optoretinography (ORG)

ORG refers to optical imaging of retinal activity evoked by visual stimuli. Generally, functional retinal imaging methods, including ORG, rely on associating measurable variations in stimulus-induced optical signals—such as scattering, absorption, intensity, phase, and fluorescence changes—with established physiological retinal processes like phototransduction, bleaching, structural remodeling, and calcium dynamics. While the term ORG is relatively recent in ophthalmology and vision science, attempts to detect functional retinal changes induced by light stimuli have a longstanding history, beginning with early studies of electroretinography. The first empirical observations of retinal responses to visual stimuli date back to 1865, when electrical currents elicited by retinal light exposure were measured in frog eyes [33]. Similar findings were soon reported for human eyes in 1877 [34], ultimately termed the ERG. Subsequent foundational studies further clarified the origins and anatomical sources of these electrical signals , with pharmacological and physiological investigations providing precise localization within the retina .

Parallel efforts to detect optical signals corresponding to neuronal activity also emerged early in the 20th century. Initial investigations demonstrated ultraviolet (UV) and visible light effects on peripheral nerve fibers during action potentials[35]. Studies of frog nerve fibers subsequently documented UV absorption changes induced by repetitive stimulation[36]. Concurrently, changes in white-light scattering properties of nerve fibers, initially observed in crustaceans[37] were later attributed to transient volumetric fluctuations during neuronal excitation[38]. The light-evoked change in volume was explained as resulting from osmotic pressure alterations driven by sodium-potassium ion exchanges across the nerve fiber membrane[39]. Comprehensive research using crustacean nerve models provided further evidence, highlighting transient and persistent scattering changes linked to neuronal swelling [40-42]. High-sensitivity laser interferometry later confirmed these volumetric fluctuations occurred at angstrom-scale resolutions[43].

Specific studies on retinal photoreceptors established a clearer link between neural activity and optical signals. Experiments on vertebrate rods identified multiple components in scattering signals, each differing in amplitude, temporal characteristics, and sensitivity to illumination. These differences correlated with distinct physiological events such as phototransduction amplification, photoisomerization, and bleaching[44]. Related investigations revealed structural alterations in rod outer segments (OS), including changes in length, width, and volume, upon exposure to varied ionic environments and light stimuli, further connecting cellular shape changes with optical scattering responses [45]. Similar research with toad rods demonstrated near-infrared transmission changes upon intense visual stimulation, aligning spectrally with rhodopsin's known absorption profile and exhibiting distinct temporal phases linked to photopigment bleaching [46]. Drawing from these observations and their conceptual parallels to ERG, the term "optoretinogram" was coined to describe the optical measurement of retinal functional changes[47]. Although early

implementations did not achieve favorable results, improvements in imaging sensor technology and optical configurations were anticipated to enhance fidelity for routine in vivo retinal functional imaging.

To date, ORG, in its various configurations described in later chapters, is an ascendant technology that overcomes many of the limitations of established modes of structural and functional imaging, providing a non-invasive, objective biomarker of retinal function. The development of adaptive optics (AO)-enhanced retinal imaging in 1997 laid the groundwork for advanced functional retinal imaging, correcting ocular optical imperfections and enabling visualization of individual photoreceptors and their spatial distribution in vivo [48,49]. Combining AO with scanning laser ophthalmoscopy (SLO) and optical coherence tomography (OCT) provided unprecedented spatial resolution and contrast for human and animal retinal studies, facilitating significant advances in both basic science and clinical retinal research [50-53]. ORG has directly benefited from these technological innovations, and its initial feasibility was built upon advances in high-resolution retinal imaging.

1.4 Rationale of ORG in human retina

Having established the principles and foundational methods of ORG, we now turn to its specific application and rationale within the human retina. ORG detects minute intrinsic optical changes in retinal tissue following a visual stimulus and is implemented with advanced imaging tools such as OCT and SLO. These standard imaging tools are often enhanced with adaptive optics (AO) to capture these cell-specific changes in vivo. ORG can be categorized into two complementary approaches: phase-based and intensity-based methods. Phase-based ORG measures stimulus-induced shifts in the phase of backscattered light, which correspond to nanometer-scale physical

displacements in the retina. Intensity-based ORG (iORG), by contrast, tracks changes in the reflectance or scattering intensity from retinal layers or cells. Both methods exploit the fact that retinal cells undergo small changes in their optical properties (shape, refractive index, length) when they respond to light. Here, we will focus on photoreceptors in this dissertation.

A key concept in phase-based detection is the optical path length (OPL), defined as the product of refractive index and physical distance:

$$OPL = n \times d, \tag{1.1}$$

where the n is refractive index while the d is the thickness. Changes in OPL lead to proportional phase changes Δφ, which can be described:

$$\Delta\phi = \frac{2\pi}{\lambda} \times OPL, \tag{1.2}$$

where OPL is represented by the phase change in the interferometric signal. In essence, ORG allows the optical tracking of retinal function by measuring tiny light-induced changes in OPL (via phase) or in reflectance intensity. The result is a noninvasive "optophysiological" assay of retinal health, enabling functional assessment at a cellular scale that complements traditional structural imaging.

1.4.1 Phase-based ORG

Phase-resolved ORG leverages OCT to detect extremely small axial motions or optical length changes in the retina that occur upon photoreceptor activation. By repeatedly acquiring OCT scans and computing phase differences over time, phase-based ORG can measure displacements on the order of nanometers. When a photoreceptor outer segment elongates or shortens in response to a light stimulus, the phase of the back-scattered OCT signal shifts, indicating a nanometer-scale

change in the round-trip (double-pass) optical path. The time-varying OPL change denoted by phase difference between two reflectors (e.g., the two ends of the photoreceptor outer segment, inner/outer segment junction, ISOS, and cone outer segment tips, COST, shown in Figure 1.1) is expressed as below, with an extra factor of 2 due to the round trip of the OCT light:

$$\Delta OPL\ (t) = \lambda_0 \times \frac{\Delta\phi_{ISOS/COST(t)}}{4\pi} \tag{1.3}$$

Previous study[54] demonstrated that a phase-sensitive OCT extension can detect nanometer-scale changes in optical path length (ΔOPL), resolving displacements on the order of 1 nm in living cells. They calibrated the system's displacement sensitivity and derived a shot-noise-limited detection floor, validating that OCT phase measurements achieve nanometer-scale displacement sensitivity. Thus, it can be detected by measuring changes in phase, providing a highly sensitive assay of photoreceptor activity [55]. This interferometric sensitivity to tiny path length changes is the hallmark of phase-based ORG.

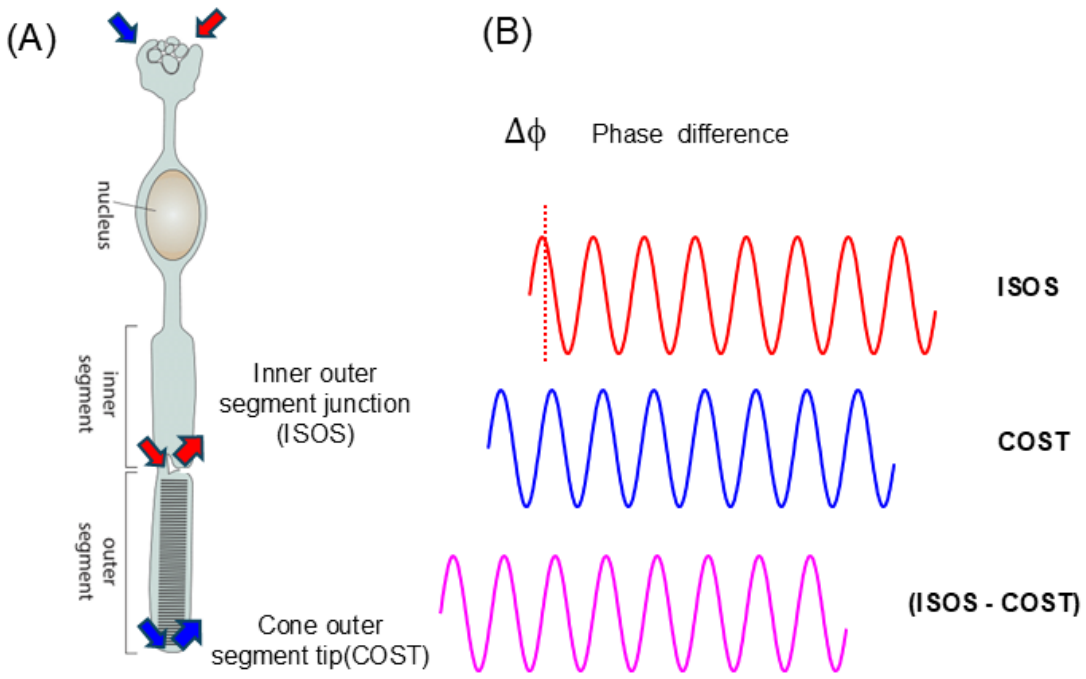


Figure 1.1 Illustration of the phase difference across the cone outer segment. Red and blue rays (and their corresponding waveforms) represent the back-reflected optical phase from the inner/outer segment junction (IS/OS) and the cone outer-segment tips (COST), respectively, while the pink waveform depicts the differential phase between these two layers.

A typical ORG traces vs. time is shown in Figure 1.2 [56]. We can see after a short contraction, the OPL increases sharply in 300ms, and then slowly reaches a plateau. Immediately after the 5 ms green flash (528 ± 5 nm) the change in OPL between ISOS and COST shows a brief negative deflection of ~ 20 nm, the contraction correlated to the early receptor potential (ERP). This is followed by a rapid rise that reaches ~ 300 nm within the first 300 ms, reflecting stimulus-driven osmotic swelling in the outer segment [56]. Beyond 0.3 s, the growth rate slows, and the response gradually approaches a plateau (~320 nm at 1.1 s). The trace was recorded over 1.18 s at a volume rate of 20 Hz, illustrating the temporal dynamics that can be resolved with modern high-speed ORG acquisition.

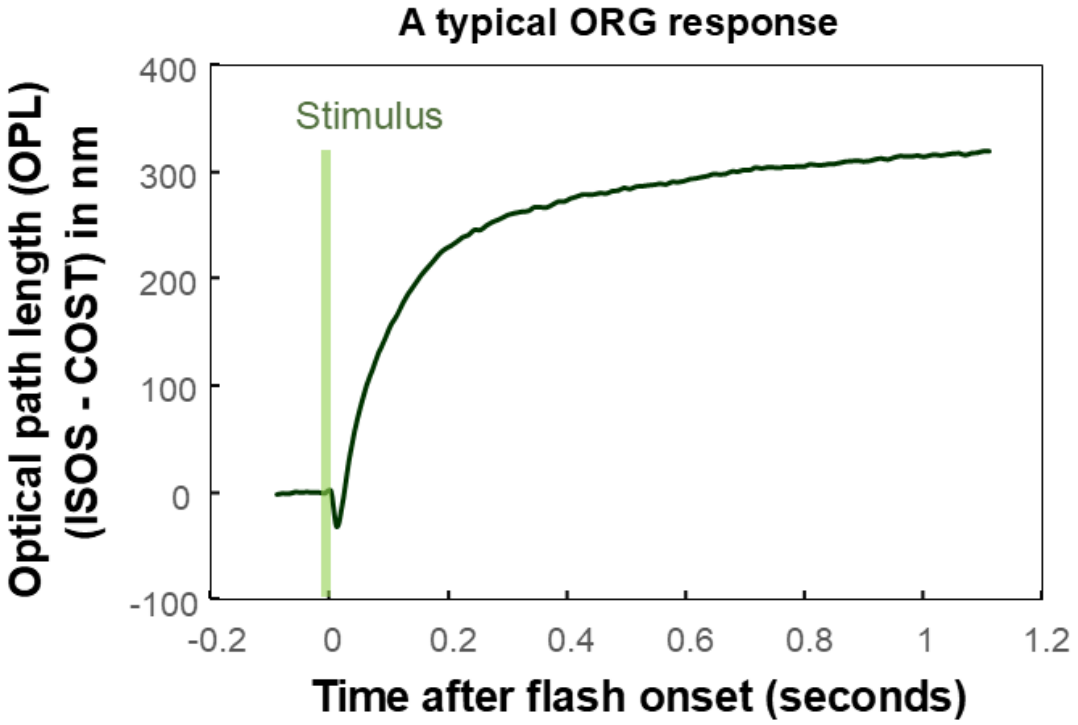


Figure 1.2 A typical ORG response vs. time. Change in optical path length (ΔOPL) between ISOS and COST as a function of time following a 5 ms, 528 ± 5 nm flash (green bar at $t = 0$). Data were acquired for 1.18 s at 20 Hz.

However, it should be noted that achieving reliable phase-based ORG signals poses significant technical challenges. The interferometric phase must remain stable over the recording period, which can be undermined by eye motion or optical system drift. Even tiny involuntary eye movements or tissue vibrations can produce phase noise that obscures the functional signal. To figure out those hurdles, different implementations are applied such as precise image and volume registration with point-scan AO-OCT to minimize the effects of involuntary motion and further enhance image fidelity in the living human eye [57]. Moreover, parallel imaging techniques such as line-scan and full-field imaging offer an effective compromise between acquisition speed and image quality. Despite these difficulties, phase-based ORG has yielded profound insights. It can

detect OPL changes on the order of a few nanometers, revealing phenomena like photoreceptor elongation during the phototransduction cascade. Recent studies have shown that ORG functional signatures under different experimental paradigms can be instructive for a wide-range of cellular insights in ways that were previously impossible in vivo, for example, differentiating cone subtypes based on differential spectral sensitivity [55], and assessing dysfunction in retinal disease[58,59]) .

1.4.2 Intensity-based ORG

Intensity-based optoretinography (iORG) detects light-induced reflectance changes mainly from photoreceptors using adaptive optics scanning laser ophthalmoscope (AOSLO) [60]. The reflectivity of photoreceptors changes dynamically during phototransduction, and iORG can capture stimulus-induced intensity fluctuations at single-cell resolution. In this mode, the backscattered light from individual cone photoreceptors is tracked before and after a stimulus, revealing intrinsic optical signals that originate from the phototransduction process [60,61]. The precise origin of the iORG signal is linked to activity-dependent changes in the photoreceptor outer segments – for example, alterations in refractive index, scattering from discs, or nanometer-scale physical length changes that modulate the amount of reflected light. Such changes may arise from osmotic swelling or other structural consequences of phototransduction. Even slight shifts in outer segment optical path length can produce constructive or destructive interference that alters reflectance [60].

The iORG response exhibits clear stimulus-dependence and functional specificity. Experiments show that the cone iORG amplitude grows systematically with stimulus intensity and has an action spectrum matching the luminous efficiency function, confirming that photopigment absorption triggers these optical changes [61]. Compared to phase-based ORG (pORG), which directly measures optical path length changes, iORG provides a complementary view by quantifying intensity

(scatter) changes. Notably, the time course of intensity-based signals closely parallels that of pORG, indicating both modalities reflect the same underlying physiological events. However, pORG offers direct nanometric displacement readouts and a 3D cross-sectional view of the retina, while iORG may be simpler to implement in *en face* imaging and still achieves high spatial resolution. Together, intensity- and phase-based ORG approaches enable a comprehensive characterization of photoreceptor function at the cellular level.

1.4.3 Cellular-scale ORG with adaptive optics (AO)

Combined with the last two sections, the advent of AO has transformed ORG from a mesoscopic assay into a single-cell functional readout. AO corrects for the eye's intrinsic aberrations, facilitating single-cell resolution in an AO-OCT system. AO-OCT captures phase changes with nanometer sensitivity. High-speed AO-OCT systems can acquire essentially "freeze" ocular motion, so stimulus-locked optical-path-length shifts as small as ~5 nm are resolved from the inner/outer-segment junction to the cone outer-segment tip, revealing fast mechanical transients and slower osmotic elongation in single cones [56]. In practice, achieving such sensitivity requires a high degree of phase stability and fast imaging. Many implementations employ AO to correct ocular aberrations and isolate individual cells, as well as high-speed acquisition to sample rapid phase dynamics [55,62,63]. Using AO-OCT, researchers can thus monitor the optical phase of specific retinal layers (e.g. cone outer segments) before and after a stimulus at a single cell level. Moreover, by using AO line-scan OCT to record phase-resolved optoretinograms from single human cones, it has been shown that cones undergo rapid nanometer-scale deformations immediately after photon absorption[56]. This provided direct optical evidence of the very first steps of phototransduction in the living eye. These and other adaptive optics implementations have firmly established phase-ORG as an ultra-sensitive method to monitor photoreceptor function at the

cellular level. With the implementation of AO module, phase-ORG traces exhibit cone-type–specific kinetics and amplitudes that scale linearly with stimulus intensity, providing objective in vivo classification of L, M and S cones as well as early markers of dysfunction in inherited retinal disease[55,56,58,59,62].

AOSLO, in turn, measures stimulus-evoked reflectance modulations under the intensity-based ORG (iORG) paradigm. High-speed confocal and split-detector AOSLO reveal reproducible brightness[64] changes that follow the photopigment activation and offer insight into phototransduction machinery.

Together, AO-OCT phase ORG and AO-SLO intensity ORG furnish complementary, co-registered metrics: the former gives absolute nanometric displacements, the latter highlights the potential utility as a simpler, low-cost method to detect cone dysfunction in all stages of disease progression[65]. Combined in multimodal platforms, they deliver a holistic, label-free assessment of photoreceptor physiology at unprecedented spatial and temporal resolution, positioning AO-ORG as a powerful biomarker for early disease detection and therapeutic monitoring[58,59,66].

Chapter 2. Coarse-scale optoretinography (CoORG): system design, experiment protocol, and data workflow

2.1 Optical coherence tomography for structural and functional imaging

The development of optical coherence tomography (OCT) in the 1990s fundamentally transformed retinal imaging and began to close the gap between structure and function [67]. OCT is a noninvasive interferometric imaging modality that generates high-resolution cross-sectional views of the retina, akin to "optical biopsies" of tissue in vivo [67]. With its ability to visualize retinal layers (nerve fiber layer, photoreceptor layers, etc.) and pathological features like fluid, edema, or membrane traction, OCT has become an indispensable structural imaging tool in both clinical and research ophthalmology [68].

In summary, retinal examination has evolved from simple visual inspection to a sophisticated array of structural and functional tests. Conventional structural tools such as fundus photography, angiography, SLO, FAF, and others, provide detailed maps of ocular anatomy and pathology. Functional assessments like visual acuity, perimetry, and ERG, probe how well the retina works but have limitations in subjectivity and resolution. OCT has been a pivotal innovation, initially giving ophthalmologists an unprecedented 3D view of retinal microstructure, and now serving as a platform for functional imaging advances. With ultrahigh-resolution, noninvasive imaging, OCT has largely bridged the historical gap: in clinical practice, it correlates structural findings to visual function (for example, restoring outer retinal layers on OCT often predicts visual acuity

improvement, and in research, it is extending into direct measurement of retinal function via techniques like optoretinography. This convergence of structural and functional retinal imaging is enriching our understanding of retinal diseases and may ultimately enable earlier detection and better tracking of dysfunction at the cellular level, fulfilling a key goal of modern ophthalmic diagnosis.

OCT is a noninvasive imaging technique that provides high-resolution cross-sectional views of biological tissue using the interference of low-coherence light. Conceptually, it employs a Michelson interferometer with a short-coherence-length light source, typically a broadband near-infrared source, to achieve axial sectioning. In the interferometer, light is split into a reference arm (usually reflecting off a mirror) and a sample arm (backscattered from tissue). When the returning light from both arms is recombined, they produce an interference signal (an interferogram) only when the optical path length difference is within the source's coherence length. The resulting intensity I at the detector is given by the two-beam interference formula:

$$I = I_1 + I_2 + 2\sqrt{I_1 I_2}\cos(\Delta\varphi), \tag{2.1}$$

where I_1 and I_2 are the intensities from the sample and reference arms, respectively, and $\Delta\varphi$ is the phase difference between them. The first two terms $I_1 + I_2$ represent the non-coherent intensities, while the last term is the interference fringe term, which oscillates with phase $\Delta\varphi$. This phase is proportional to the optical path difference between the arms. Thus, interference fringes (modulation) are observed only when the path length difference is close to zero within the coherence gate, allowing depth-resolved detection of reflections. In practice, the sample reflectivity profile as a function of depth is obtained by scanning this path length difference and detecting the interference envelope.

In Time-Domain OCT (TD-OCT), the reference mirror is mechanically scanned in time, and interference intensity is recorded as a function of reference arm delay. Peaks in the interferogram envelope correspond to reflective structures at specific depths in the sample. The depth (z-location) of a reflector is measured when the reference delay matches the sample delay to within the coherence length, producing a fringe burst at that position. Early demonstrations of OCT used TD detection, achieving micrometer-scale axial resolution in biological tissues [67]. In Fourier-Domain OCT (FD-OCT), depth information is obtained without mechanical scanning by analyzing the interference spectrum. Two implementations exist: spectral-domain OCT (SD-OCT), which uses a dispersive spectrometer to measure the interference intensity as a function of wavelength, and swept-source OCT (SS-OCT), which uses a tunable laser to acquire spectral data over time [69]. Because the interference signal encodes depth as frequency (wavelength) oscillations (via the Fourier shift theorem), the sample's reflectivity vs. depth (A-scan) is recovered by computing the inverse Fourier transform of the acquired spectrum [70,71]. This Fourier-based decoding relies on the Wiener–Khinchin relation, which states that the Fourier transform of the interferogram (spectral power) corresponds to the autocorrelation of the sample reflections in depth. A key advantage of FD-OCT is its higher sensitivity and speed: since all depths are measured simultaneously, FD-OCT can be ~ 10-100 times faster and provides a ~ 20-30 dB signal-to-noise ratio improvement over TD-OCT. This sensitivity gain arises from not having to discard most of the light during time-scanning, as well as from the multiplex advantage of Fourier detection. FD-OCT has become the predominant mode in modern systems due to these benefits [72-74].

2.1.1 Axial resolution and coherence gating

The axial resolution of OCT is determined by the coherence length of the light source. In essence, the short coherence length of a broadband source acts as a gate that confines the interference to a

narrow depth range, decoupling axial resolution from the imaging optics. For a source with central wavelength λ_0 and full-width-at-half-maximum (FWHM) bandwidth $\Delta\lambda$, the coherence length l_c (defined as the FWHM of the source's autocorrelation) is approximately:

$$lc = \frac{2\,ln2}{\pi}\frac{{\lambda_0}^2}{\Delta\lambda} \tag{2.2}$$

assuming a Gaussian spectral profile. This coherence length corresponds to the axial resolution Δz (in air) of the OCT system, i.e. the smallest discernible separation between two reflecting layers along depth. In practice one often uses $\Delta z \approx l_c$ for the axial resolution criterion (sometimes quoted as the full-width at half-maximum of the axial point-spread function). For example, a source with 840 nm central wavelength and $\Delta\lambda$ = 50 nm has lc on the order of a few microns, enabling ~ 4.45 μm axial resolution in tissue imaging (given the refractive index in tissue n = 1.4). This ultra-small coherence gate is what allows OCT to differentiate fine layers similarly to histology. Notably, axial resolution is independent of the focusing optics or numerical aperture (NA) of the imaging probe – it is purely a function of the source's optical bandwidth. Broader bandwidth ($\Delta\lambda$) yields shorter coherence length and hence finer axial resolution, at the expense of signal strength (since optical power is spread over more frequencies). In contrast to confocal microscopy (where axial resolution is limited by the physical pinhole and objective NA), OCT's use of coherence gating means even a low-NA beam can achieve high axial resolution, as long as the source is broadband. In summary, the axial resolution Δz in OCT can be estimated by the coherence length formula above, which highlights that using a shorter central wavelength λ_0 and/or a larger spectral bandwidth $\Delta\lambda$ will improve depth resolution. Typical OCT systems in the 840 nm range achieve 3–10 μm axial resolution in air, whereas ultra-broadband sources (including visible light OCT) can reach sub-micron axial resolution at the cost of penetration depth.

2.1.2 Lateral resolution and depth of focus

The lateral (transverse) resolution in OCT is determined by the focusing of the sample arm beam and behaves similarly to a conventional optical microscope. It is often defined as the smallest spot size (or minimum distance between two points laterally) that the system can resolve. For a diffraction-limited Gaussian beam, the lateral resolution (e.g. the FWHM of the intensity point-spread-function at focus) can be approximated as:

$$\Delta x \approx 0.37 \frac{\lambda}{NA} \tag{2.3}$$

Where the λ is the vacuum wavelength of the light and NA is the numerical aperture of the sample objective (with n the refractive index of the medium, n ≈1.3 – 1.4 in tissue). This relation is essentially the diffraction limit for a focused beam (0.37 is a factor corresponding to the FWHM of a focused Gaussian, slightly smaller than the 0.51–0.61 factor used for Rayleigh two-point resolution criteria). A higher NA (i.e. a larger beam convergence angle Δθ or tighter focus) yields a smaller spot and thus improves lateral resolution. Unlike axial resolution, the lateral resolution is coupled to the optics and is independent of the source coherence length (provided the beam is roughly collimated over the coherence range). This decoupling of axial and transverse resolutions is a unique feature of OCT systems, allowing, for example, a low-NA beam to maintain high axial clarity (due to low coherence) at the cost of blurrier lateral details.

One practical consequence of high lateral resolution (high NA) in any optical imaging system is a reduction in the depth of focus (DOF) – the axial distance over which the beam remains tightly focused. In OCT, the depth of focus is often defined as the range over which the lateral resolution does not degrade significantly (commonly taken as the distance between the points where the beam

diameter doubles, equivalent to twice the Rayleigh range of the beam). For a Gaussian beam, the DOF is approximately:

$$DOF \approx \frac{\lambda}{NA^2} \tag{2.4}$$

on the order of a millimeter or more for typical OCT optics. This inverse-square dependence means that achieving very high transverse resolution (large NA) dramatically shortens the in-focus depth range. OCT systems generally use low NA objectives (e.g. 0.05–0.1) to obtain a long depth of focus (1–3 mm) that matches or exceeds the penetration depth in tissue. With low NA, lateral resolution might be a few tens of microns, but the extended focus allows uniform imaging over the full depth range of interest without the need for refocusing. In specialized forms of OCT like optical coherence microscopy (OCM), a high NA objective (0.5–1.0) is used to attain ~1 μm lateral resolution, at the expense of a very shallow DOF (only tens of microns). This trade-off can be mitigated by dynamic focus tracking or advanced optical designs (e.g. Bessel beams or optical beam shaping) to extend the focus, but these add complexity. In summary, the lateral resolution Δx is governed by classical diffraction optics and improves with higher NA, whereas the depth of focus shrinks as $1/NA^2$. Optimal OCT imaging often balances these parameters: using an NA just high enough to resolve the features of interest, while still providing a DOF that covers the sample thickness. Importantly, because OCT's axial resolution is independent of NA, one can obtain high axial detail even with a low-NA beam, a key advantage over confocal imaging. This flexibility allows the design of OCT systems that penetrate millimeters deep with micrometer-scale axial slicing, and moderate lateral resolution, ideal for biomedical imaging in vivo. Future developments in OCT optics continue to explore methods to achieve high lateral resolution over an extended DOF (so-called "extended focus" OCT) to approach isotropic resolution volumetric imaging.

2.2 Phase-resolved OCT modalities

Traditional OCT systems were designed to maximize structural imaging performance, but detecting functional signals (which are often small phase changes) imposes additional requirements on speed and stability. Over time, several OCT modalities have been developed or adapted to improve the detection of phase-resolved changes in the retina. In particular, the method of acquiring OCT signals, whether by scanning a focused beam or capturing an entire field at once, has significant implications for spatial resolution, imaging speed, and phase stability. This section outlines the evolution of three main OCT acquisition strategies and their relevance for functional (phase-resolved) retinal imaging: point-scan OCT, full-field OCT, and line-scan OCT. The Figure 2.1 shows the different imaging modes. Each modality represents a different trade-off between lateral resolution and parallelization of signal acquisition, with consequences for how well nanometer-scale phase shifts (such as those in optoretinography) can be measured amidst ocular motion and noise.

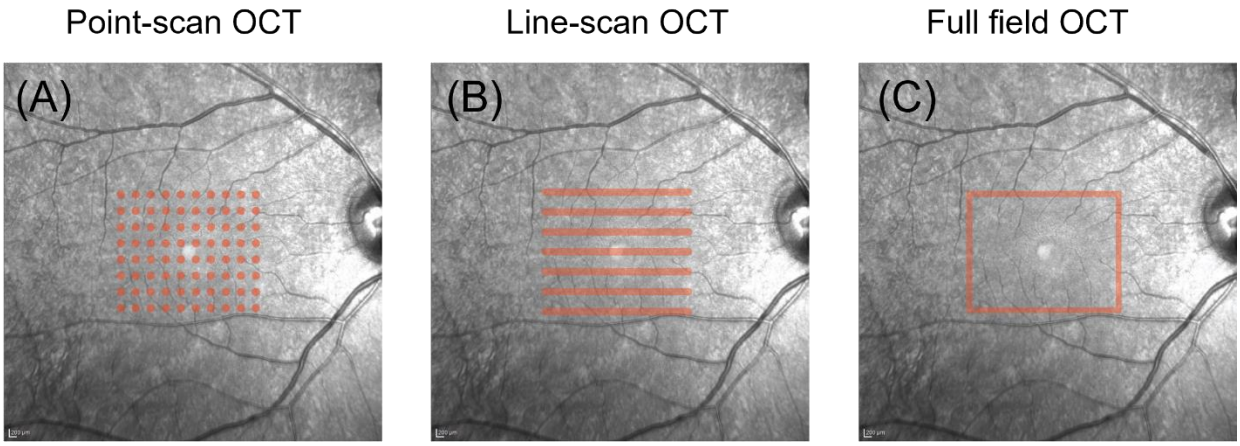


Figure 2.1 Different imaging modes: (A) point-scan OCT; (B) line-scan OCT; (C) full-field OCT. The single acquisitions in each exposure are labelled as the red dot, red line, and red rectangle shown in (A) – (C), respectively.

2.2.1 Point-scan OCT

Point-scanning OCT is the conventional method employed in most commercial and research OCT systems. In a point-scan configuration, a single tightly focused light beam is scanned across the sample point-by-point (typically using galvanometric mirrors for the X and Y axes) to build up an image. The interference signal from one point (one A-scan line) is detected at a time, and the system sequentially samples adjacent locations to form a two-dimensional cross-section. This approach inherently maintains confocal gating in both lateral dimensions, the detection is only sensitive to the small focal volume where the beam is currently focused, rejecting out-of-focus light, which contributes to high image contrast and axial sectioning quality [75]. Point-scan OCT can be implemented in time-domain (moving reference mirror) or Fourier-domain (spectral or swept-source) configurations, but in either case only one spatial location is measured at a given instant.

The point-scan approach offers excellent lateral resolution (often ~10–20 μm in the human retina with standard optics, and as fine as ~2–3 μm with adaptive optics correction [76,77]) and high signal-to-noise ratio for each A-scan, since all the light is concentrated into one spot. It also allows flexible adjustment of scanning density and region of interest. However, a fundamental limitation is speed. Even with modern high-speed detectors and lasers, point scanning must raster across thousands of points to cover a 3D volume, leading to volume acquisition rates on the order of a few tens of hertz (for a 3D cube of the retina) in typical systems. This means that eye motion (saccades, microsaccades, drift) can cause misalignment or phase noise between sequentially acquired lines. In structural imaging, this manifests as motion artifacts that can be corrected by post-processing or eye tracking. But in functional phase-resolved imaging, such motion is especially problematic: tiny phase shifts due to neural activity could be swamped by phase changes from even slight involuntary motions between frames. Point-scan OCT systems, when used for functional studies,

therefore demand extremely stable fixation or active motion correction to achieve the phase stability needed for detecting nanometer-scale changes. Despite these challenges, point-scanning OCT has been successfully used in pioneering functional experiments. For example, early adaptive optics OCT (AO-OCT) systems (which are point-scan based) managed to visualize intrinsic reflectance changes in individual cone photoreceptors [78]. Moreover, phase-resolved Doppler OCT, a functional extension of point-scan OCT, has long been used to measure blood flow by repeated scanning of the same location and analyzing phase shifts [79]. These applications illustrate that point-scan OCT can probe function, but to do so reliably for optoretinography signals, it faces an uphill battle against the limits of timing and motion. In summary, point-scanning remains the workhorse of OCT with high spatial resolution and flexibility, but its sequential nature imposes speed and phase stability constraints that have led researchers to explore alternative imaging geometries for functional retinal imaging.

2.2.2 Full-field OCT

Full-field OCT (FF-OCT) takes a very different approach: instead of scanning a point across the sample, it illuminates and captures an entire field of view in parallel, using a camera to record interference images from all points simultaneously. In a typical full-field OCT setup, a broadband light source (often a white light lamp or LED) illuminates the sample (e.g. the retina or a tissue specimen) uniformly. The backscattered light from the sample interferes with reference light, and this interference pattern is imaged onto a two-dimensional detector array (such as a CCD or CMOS camera) [80]. By varying the reference path length or using phase-shifting techniques, one can retrieve tomographic information from these en face interference images. Essentially, FF-OCT acquires en face (transverse) slices of the sample at a given depth, rather than the conventional B-scan orientation [81]. By capturing many pixels in parallel, FF-OCT can achieve ultrahigh resolution

and avoid the need for raster scanning. One of the motivations for full-field OCT is to achieve microscope-like resolution and an "optical biopsy" capability. Because it often uses short-coherence broadband light and high-NA microscope objectives, FF-OCT has demonstrated sub-micron resolution in laboratory settings [82]. This allows imaging of cellular structures with a clarity approaching histology, which is valuable for examining tissue samples or small animal retinas. Additionally, since FF-OCT collects data from all points simultaneously, it can in principle be very fast, capturing an entire 2D frame in one camera exposure. Researchers have leveraged this parallelism to push imaging speeds: for instance, ultra-fast full-field OCT systems have been demonstrated, achieving unprecedented acquisition speeds for en face OCT frames [81]. This speed is important for in vivo use, as the entire volume must be acquired quickly to minimize motion blur. Despite its promise, full-field OCT presents some challenges, especially for living human retinal imaging. One issue is motion: because FF-OCT typically acquires volumetric data by recording a sequence of *en face* images at different depths (e.g. by stepping the reference mirror or via Fourier volume reconstruction), any slight eye movement between frames can disrupt the coherence of the volume. Even with high frame rates, the eye's motion can be a limiting factor; as noted by Dubois and Boccara, in vivo imaging with FF-OCT is difficult due to object motion, and significant effort has been directed at overcoming this limitation [83]. Another challenge is detection sensitivity. Spreading light over a full field means each camera pixel receives a weaker signal compared to focused point detection, and camera noise can further reduce sensitivity. Indeed, while full-field OCT can produce stunning images in static samples, achieving the same sensitivity as point-scan OCT for deep, weakly reflective retinal structures is non-trivial. Researchers have worked to improve camera technology and optical setups (for example, using synchronized optical choppers or multi-shot averaging) to boost sensitivity. For functional imaging, full-field OCT

offers an intriguing advantage: by capturing the whole scene at once, it avoids the sequential sampling delays that plague point-scan stability. Any global stimulus-induced change (say, a transient change in photoreceptor reflectance across the field) could be recorded simultaneously for all pixels, potentially improving the detection of fast intrinsic optical signals. Additionally, FF-OCT readily produces *en face* functional maps that align with other imaging modalities. There have been demonstrations of FF-OCT detecting functional contrasts – for example, changes in the sample's optical properties under different conditions – though this has mostly been explored in ex vivo tissues or animal models. The high lateral resolution of FF-OCT is particularly useful for en face visualization of photoreceptors and capillaries, which could be leveraged to monitor subtle changes at the cellular level [84]. In summary, full-field OCT represents a high-resolution, parallel-imaging approach that excels in providing en face structural images and has potential for functional imaging due to its simultaneous capture of the entire field. Ongoing advancements in speed and sensitivity are bringing FF-OCT closer to practical in vivo retinal applications, but it remains somewhat niche compared to scanning OCT. Understanding its principles, however, provides a useful reference point for the hybrid strategies like line-scan OCT that combine advantages of both paradigms.

2.2.3 Line-scan OCT (chosen architecture)

Line-scan OCT can be viewed as a hybrid between point-scanning and full-field approaches. Instead of illuminating a single point or the entire field, line-scan OCT illuminates a line across the sample and detects the backscattered light from that line in parallel. In practice, this is often achieved by focusing a narrow line-shaped beam on the retina and using a high-speed camera or line-sensor to capture the interference signal from all points along that line simultaneously. Each camera exposure thus records a full B-scan (a cross-sectional slice) of the retina in one snapshot

[55,63,85,86]. The OCT system then scans this line illumination across the retina in the direction perpendicular to the line, building up a volume. Because an entire B-scan is acquired at once (rather than assembling it from sequential A-scans), line-scan OCT greatly increases the frame rate of cross-sectional imaging and improves phase synchronization across each B-scan.

The line-scan geometry preserves confocal detection in one dimension (along the scan dimension) but parallelizes detection in the orthogonal dimension [55]. This means it retains some of the high contrast and optical sectioning benefits of point-scan (since the line of illumination is still tightly focused and rejects out-of-focus light in that direction), while achieving a major boost in speed akin to full-field in the other direction. Notably, acquiring multiple A-lines simultaneously by a line-scan reduces the time differences and relative motion between neighboring A-lines. As a result, the phase differences between adjacent points along the line are inherently stable, since they are recorded in the same camera frame. In other words, line-scan OCT offers excellent phase stability within each B-scan, a critical feature for functional imaging where one is looking for tiny phase shifts. In fact, experimental studies have shown that the line-scan configuration provides sufficient phase stability to detect minute stimulus-induced changes in photoreceptor outer segments that would be difficult to resolve with a conventional point-scan system [55,63]. One research team concluded that line-scan OCT achieved the combination of high speed and phase repeatability needed to reliably capture optoretinography signals in the living human eye [55].

Speed is a key advantage of line-scan OCT. Since each frame is a full B-scan, frame rates in the kilohertz range are attainable with modern high-speed cameras and light sources. For instance, line-field spectral-domain OCT systems have demonstrated B-scan rates of 2500 – 16000 Hz with adaptive optics, resolving individual cones in cross-section [55,63]. Such rapid B-scanning means an entire 3D volume can be acquired in a few hundred milliseconds or faster, substantially “freezing”

eye motion. Simulations and experiments have suggested that volume rates above a few kHz are ideal to avoid phase decorrelation from ocular motion, and line-scan approaches are pushing towards that regime. In terms of spatial resolution, line-scan OCT can achieve the same optical resolution as point-scan, since it uses similar optics, and it can be combined with adaptive optics for cellular-level lateral resolution [55,63]. There is a slight compromise in that one dimension of the camera is used for spectral dispersion (in spectral-domain implementations) which can impose some trade-off between axial range and lateral field size. However, clever optical designs (such as anamorphic optics to independently optimize sampling in the line vs. spectral dimensions) have been employed to balance these factors [55,63]. Swept-source versions of line-field OCT also exist, which use a rapidly tunable laser and a line detector array, further mitigating the constraints of 2D cameras [87,88]. For functional retinal imaging, especially optoretinography, line-scan OCT appears to hit a sweet spot. It provides high enough speed to capture fast photoreceptor responses with minimal motion noise, high enough lateral resolution to resolve individual photoreceptors (with AO assistance), and stable phase relationships across each frame to detect small optical path length changes. It also produces data in the familiar format of cross-sectional images and volumes, which can be advantageous for co-registration with traditional OCT and clinical workflows. In Figure 2.2, there is schematic of how line-scan SD-OCT works. A cylindrical lens converts the point focus into a line focus at the sample plane. A one-dimensional galvanometer sweeps this line laterally, while a 2-D camera records the line-illumination interferogram in a single exposure. Applying a fast Fourier transform (FFT) to each camera row yields a depth-resolved profile, assembling a B-scan that spans from the inner to the outer retina. Successive galvo positions generate sequential B-scans which, when stacked, form a three-dimensional retinal volume.

In summary, line-scan OCT emerged as a means to bridge the gap between slow, high-contrast point scanning and fast, parallel full-field acquisition. By doing so, it has enabled new possibilities in phase-resolved retinal imaging, notably the reliable capture of optoretinographic signals that reflect the function of retinal neurons. The next section will discuss the concept of optoretinography in detail and why these technical advancements in OCT are so crucial for measuring photoreceptor function noninvasively.

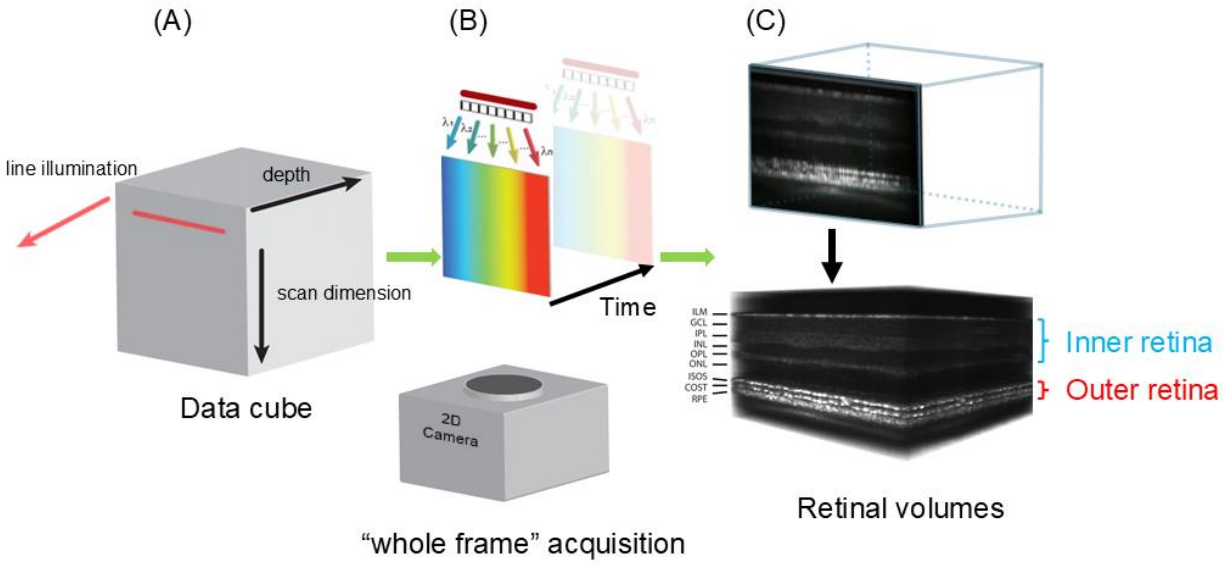


Figure 2.2 Schematic of line-scan imaging using a 2D camera. Raw data are acquired as a three-dimensional cube whose axes correspond to the line-illumination direction (fast axis), the slow scan dimension, and axial depth. A single exposure of the 2-D camera captures the interferometric fringe pattern for one line, yielding an instantaneous B-scan interferogram. Fourier reconstruction of each interferogram produces a structural B-scan, and sequential B-scans are stacked to form a volumetric dataset in which the principal retinal layers, summarized here as inner versus outer retina, are delineated.

2.3 Rationale for the CoORG platform

While most ORG imaging systems incorporate adaptive optics (AO) to achieve cellular-level resolution of retinal activity, the inclusion of AO often restricts the field of view (FOV) and limits the range of patient populations that can be effectively imaged. To address these constraints, we developed a coarse-scale optoretinography (CoORG) system that operates without an AO module, thereby enabling rapid imaging across an extended FOV in a user-friendly manner. Furthermore, by eliminating the AO module, the CoORG system is more tolerant of typical ocular motions (such as microsaccades and fixational instability) and can accommodate challenging conditions (such as dry eye or extremely small pupils). These design choices make the system more patient-friendly and improve its suitability for clinical translation. Specifically, the CoORG system is based on a first-generation lens-based AO line-scan spectral-domain OCT system (described in ref [55]) and has been modified to provide a wider imaging field and to minimize the burden on subjects. We then detail the calibration procedures, including optical alignment, beam dosimetry, and stimulus verification, that ensure safe, reproducible measurements across imaging sessions. Next, we outline a comprehensive experimental workflow, followed by an automated pipeline for data segmentation, registration, and precise ORG extraction. Given the absence of AO and subsequent residual aberrations, we introduce a digital aberration-correction (DAC) algorithm, validating its accuracy using synthetic phantoms and demonstrating its effectiveness on both AO-assisted and non-AO foveal datasets. Collectively, these advancements result in a practical, versatile platform that serves as the foundation for normative and clinical ORG studies presented in subsequent chapters.

2.4 Coarse-scale optoretinography (CoORG): extended-field, line-scan OCT

The CoORG system is an adaptation of the first-generation lens-based AO line-scan spectral domain OCT previously detailed [55], modified for a wider imaging field. Unlike its predecessor, CoORG omits the AO module, specifically the deformable mirror and wavefront sensor. Designed with a 3 mm diameter entrance pupil, the system employs larger 2-inch diameter achromatic lens-based telescopes to prevent beam vignetting. Anamorphic optimization, previously used to improve light collection and resolution in the AO system, was deemed unnecessary here due to the prioritization of a broader field over cellular precision.

Figure 2.3 illustrates the system configuration. The light source, an 840 ± 25 nm super luminescent diode, is collimated to form an 8.5 mm beam, then shaped into a line illumination using an achromatic cylindrical lens. The beam splitter divides the beam between the sample and reference arms. The sample arm beam, relayed by three sets of afocal telescopes, progresses through various optical components to the eye. Back reflections are mitigated by tilting L1 to L6 lenses. Trial lenses correct system and eye refractive errors. In the reference arm, the beam is re-collimated and adjusted for diffraction. A dispersion-compensating window and axially translatable mirror ensure path length equivalence between the sample and reference arms. The detection arm combines the beams, and irises regulate beam diameter. To reduce back reflections, a slit is introduced at the imaging plane. Switching between modalities (LSO/OCT) is facilitated by an interchangeable mirror. Spectral dispersion for the OCT signal is achieved with a diffraction grating, while separate cameras capture OCT and LSO signals. Finally, an LED provides a light stimulus for ORG studies, overlaying the imaging field of 5.5°.

Line-scan OCT emerged as an optimal choice when compared with other phase-resolved OCT modalities considering its tradeoffs of imaging speed, contrast/resolution, and phase stability. While point-scan OCT offers high resolution, it has low scanning speeds. Full-field OCT, although fast with reliable phase stability, tends to underperform in its contrast and resolution due to multiple scattering artifacts. Line-scan OCT, however, bridges these gaps. In spectral domain operation, a line illumination is scanned via a 1D scanner, and the backscattered light from the sample/retina is captured onto a 2D camera after being diffracted by a transmissive grating. This provides high speed and phase stability given that one cross-sectional image or B-scan is captured in a single camera snapshot.

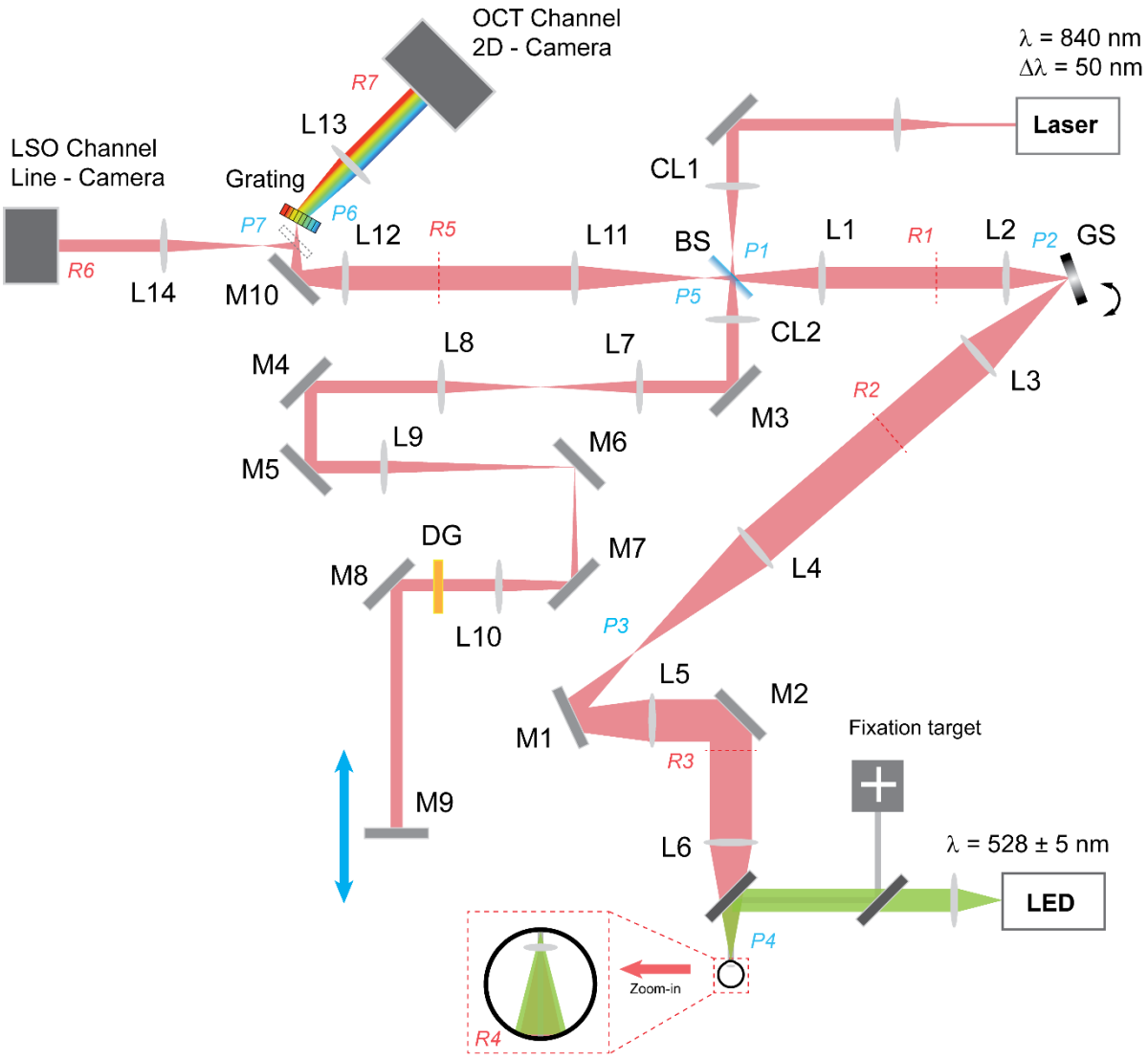


Figure 2.3 CoORG system layout. The layout is not drawn to scale, and the beam follows the general path on the optical table. The beam is shown along one dimension in illumination where the linear field is focused on the pupil planes. The orthogonal view is not shown. The beam path in detection corresponds to the case where a mirror is placed at the eye's pupil. L: spherical lens, CL: cylindrical lens, M: mirror, GS: galvo scanner, BS: beam splitter, DG: dispersion compensation glass window, LSO: line-scan ophthalmoscope, OCT: optical coherence tomography, P: pupil plane, R: retinal plane, LED: light-emitting diode.

For the system described above, the calibrated specifications are summarized in Table. 2.1.

Table 2.1 System specification

Lateral resolution	3.6 μm
Axial resolution in air	6.23 μm
Axial depth in air	2 mm
FOV	5.5 deg

2.5 System calibration

To ensure safe and repeatable imaging, the CoORG platform is calibrated before every experimental session. Two elements are verified: (i) system optical alignment and (ii) radiant-exposure compliance (imaging beam and visual stimulus).

2.5.1 System optical alignment

In order to align the CoORG system (Figure 2.3), we would put the entrance pupil (P1) as our target, mount the pupil camera at P4 and to adjust steering mirrors until the beam is centered and concentric with the 4-mm reference circle on the camera display. Then, inserting a slit at relay conjugate R1. A uniform top-hat image on the pupil camera confirms that both illumination and detection paths clear all irises and that conjugate planes remain coaxial.

2.5.2 Laser power (imaging beam) calibration

U.S. laser products are regulated by the FDA Center for Devices and Radiological Health (CDRH) under *21 CFR 1040.10 & 1040.11* (laser classification) and must meet the ocular maximum permissible exposure (MPE) limits defined in ANSI Z136.1-2022 and ISO 15004-2:2017 for ophthalmic instruments.

- For a scanning near-infrared OCT beam ($\lambda \approx 840$ nm, hazard dominated by retinal thermal loading), ISO 15004-2 class-1 permits a corneal power ≤ 4.0 mW for scan angles $\leq 40°$ over unlimited durations [89].
- Commercial retinal OCT systems typically operate at 0.7–2.5 mW; we adopt 3.0 mW ±0.2 mW as a conservative compromise between SNR and safety.

With the model eye in place and the scanner running, measure the power with a calibrated power meter aligned normal to the beam. Adjust the source attenuator until the reading is 2.9–3.2 mW; lock the attenuator and log the value in the experiment sheet.

2.5.3 Stimulation calibration

A model eye is placed at the entrance pupil, and the visual-stimulus path is aligned exactly as for the OCT power check. An adjustable iris upstream of the pupil plane sets the effective pupil diameter D_p, which determines the stimulus spot size on the retina. For a telecentric projector the retinal half-angle θ satisfies

$$\theta = \arctan\left(\frac{D_{beam}}{2f_{eye}}\right), \tag{2.5}$$

where D_{beam} is the collimated beam diameter at the pupil and $f_{eye} = 125$ mm is the paraxial focal length of the model eye. Varying D_p from 3 to 8 mm therefore produces retinal fields of 8.4°–9.0°, generally larger than the 5 × 5° imaging raster. The deliberate oversizing provides lateral tolerance so that minor eye motions or residual mis-registration cannot displace the stimulus outside the recorded field.

Stimulus power is measured with a calibrated silicon photodiode placed at the model-eye pupil while the projector delivers a continuous 530 ± 5 nm beam. Figure 2.4 shows that the measured

power P follows a near-quadratic dependence on D_p ($P \propto D_p^2$), confirming that the irradiance at the cornea remains constant over the tested aperture range. Combining the measured power with the stimulus bandwidth and retinal spot area permits calculation of the photon density:

$$\Phi = \frac{P\lambda}{hcA_{ret}}, \tag{2.6}$$

where h is Planck's constant and $A_{ret} = \pi(f_{eye} \tan\theta)^2$. All stimulus settings are well below the ANSI Z136.1 and ISO 15004-2 photochemical MPE limits for 530 nm light, providing a >2× safety margin for every experiment.

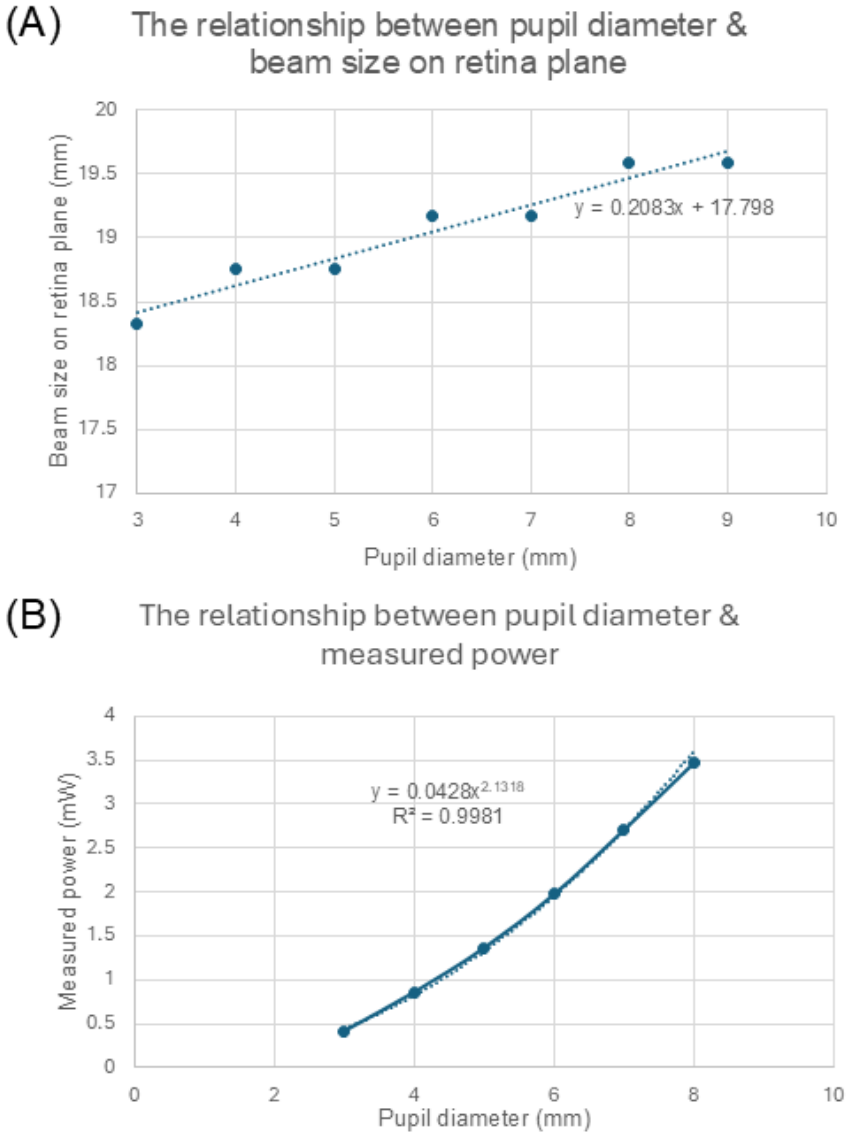


Figure 2.4 The relationship between pupil diameter and stimulated beam size on retina plane and measured power. The linear fit and polynomial fit are displayed in the plots.

2.6 Experimental protocol

The normal subjects and clinical patients were recruited for the study after an informed consent. The research was approved by the University of Washington institutional review board and

conducted according to the tenets of the Declaration of Helsinki. The pupil was dilated using Tropicamide 1% ophthalmic solution (Akorn Inc.). Without dilation, pupil miosis due to the bright stimulus light impairs comparative analysis between subjects. Instead, a maximally dilated pupil was used for all measurements, and its diameter (along with axial length) was measured to incorporate into the stimulus photon density calculation for each subject.

ORG signal characteristics crucially depend on the retina's stimulus photon density. To account for variations between individuals, photon density was calculated for each subject. The LED's spectrum and power were measured with a spectrometer and power meter, and the stimulus field's angular subtends were calculated based on its absolute size at a specific distance from the entrance pupil. These parameters remained constant for each subject. Since the LED beam size at the entrance pupil was larger than the largest dilated pupil, power was adjusted according to each subject's pupil area (Figure 2.5(C)). Power, measured in Watts, was integrated across the spectrum, and converted to photons s−1 using the speed of light ($c = 3.0\times10^{8}$ m/s in air) and Planck's constant ($h = 6.626\times10^{-34}$ J·s). Absorption by the lens [90] and macular pigment [91] were factored in using published values, providing an estimate of quanta reaching the retina per second. This value, divided by the stimulus area in angular units, yielded an estimate of photons/(s·deg^2). With the LED pulse width (10 or 20 ms) and the subject's axial length, this unit was converted to photons/μm^2, assuming a 291 μm per degree scaling factor for a 24 mm axial length.

The experimental procedure, depicted in Figure 2.5, began with axial length measurement using Zeiss IOL Master. Then, a 15°×5° FOV OCT and a 30°×30° SLO image were captured with Heidelberg OCT Spectralis to identify the CoORG data acquisition region (Figure 2.5(B)). Subjects were aligned to the CoORG system's exit pupil where pupil diameter was measured

(Figure 2.5(C)). A live LSO image stream helped locate the ROI and optimize retinal image focus, followed by line-scan OCT mode for ORG recording. The OCT image at the IS/OS was aligned with the clinical SLO image, with ORG signals extracted from ROIs surrounding the fovea (0.5° to 4.5–5°). Eye movements affected the available field for reliable ORG averaging, causing variations in ROI sizes among participants.

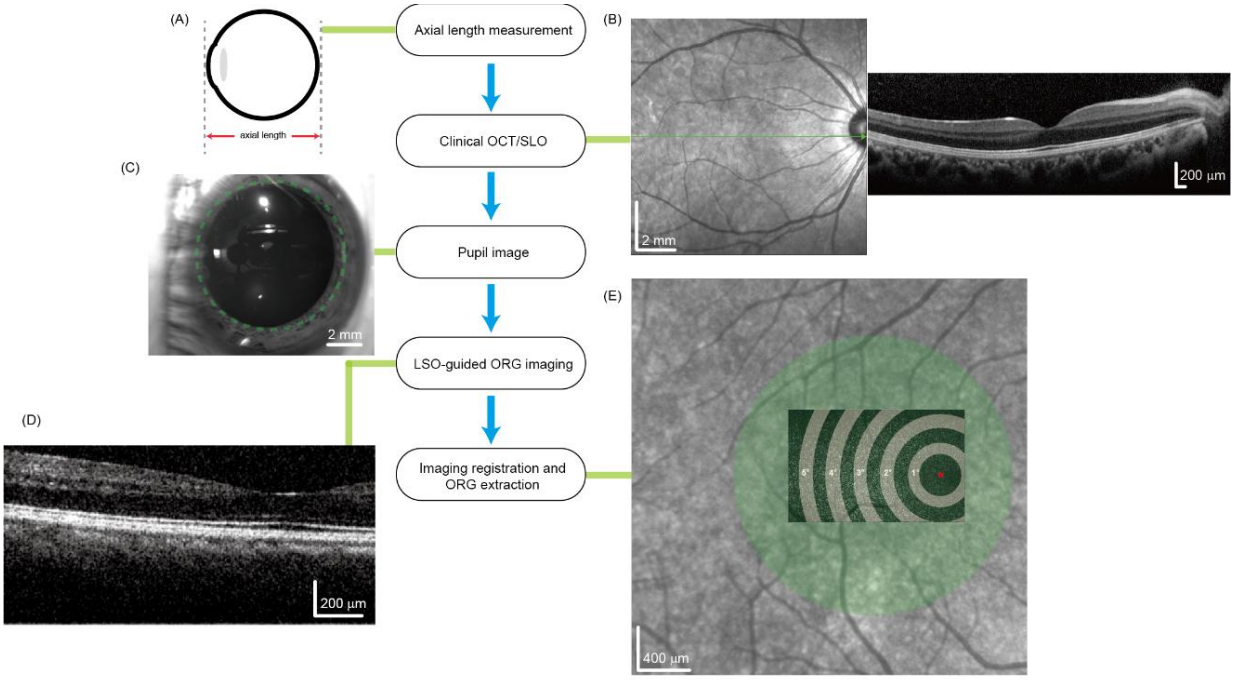


Figure 2.5 Experimental flow. (A) Axial length was measured by Zeiss IOLMaster. (B) Clinical SLO and OCT were taken for registration and finding the foveola. (C) Pupil image was taken for measuring the pupil size. (D) CoORG system B-scan example. (E) Green circle shows the circular stimulus field. ORGs were extracted in annular ROI shown as superimposed on the stimulus field, the registered IS/OS *en face* image and clinical SLO image. The red asteroid indicates the center of the fovea.

2.7 Data processing pipeline

2.7.1 Segmentation and registration

For data processing, open-source segmentation software [92] was utilized for outer retinal layers identification, optimized for our purposes for line-scan OCT. Five repeat trials were co-registered using a strip-based image registration algorithm [93] based on the en face of inner-outer segment junction (ISOS) layer image. Extracted ISOS and cone outer segment tips (COST) en face images from the registered volume were manually checked for accurate segmentation and registration. The fovea's center, marked red in Figure 2.5(E), was identified in clinical SLO and en face IS/OS images, and correlated with the OCT B-scan foveal pit location. This served as the zero-degree eccentricity reference for computing the dependence of ORG vs. eccentricity. ORG signals were averaged in each 0.5° annular ring, with 0.5° eccentricity step size, illustrated by five rings in Figure 2.5(E). ORG processing steps, based on stimulus-induced phase difference analysis between ISOS and COST, followed previous work [55].

2.7.2 Refined COST-band segmentation

Since the axial separation between the IS/OS junction and COST varies with retinal eccentricity[94], a secondary segmentation step is necessary to accurately localize the COST layer within the 5° FOV acquired by CoORG. To achieve this, the total of 500 B-scans was divided into five subsets (each containing 100 B-scans, representing approximately 1° of FOV), and these subsets were averaged to generate representative A-line profiles (Figure 2.6A, the bold red line is the averaged A-line across all 100 B-scans while the multiple thin colored lines are individual averaged A-line from different B-scans). From these averaged profiles, precise pixel depths for the IS/OS junction and COST layers were determined, producing corresponding depth maps (Figure 2.6B–C). En-

face projections of these layers ((Figure 2.6D–E) further verify the accuracy of the segmentation and confirm reliable layer detection throughout the imaging field.

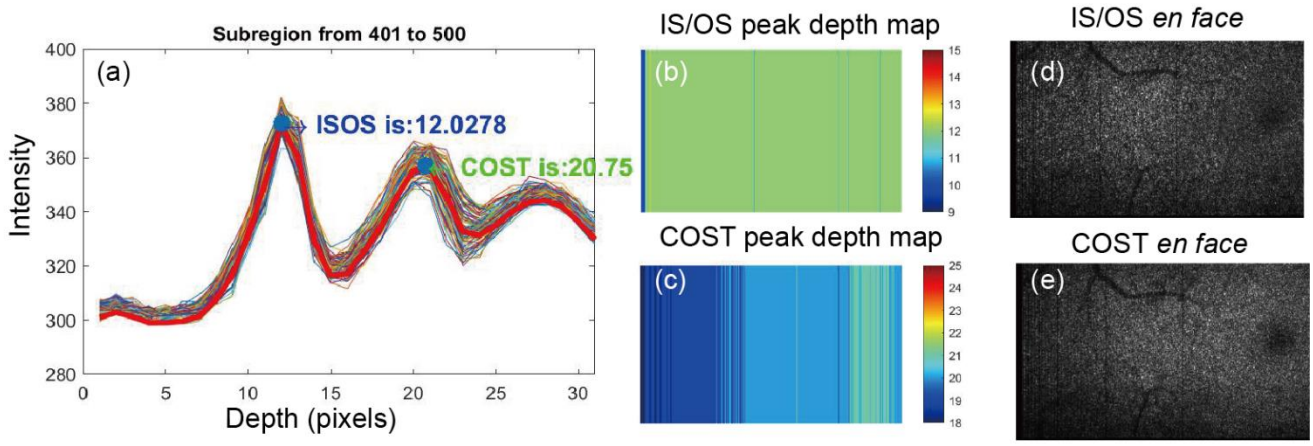


Figure 2.6 Detection of the IS/OS junction and COST layer. In each sub-region, 100 compressed B-frames are overlaid, with their mean profile highlighted by a red curve (a). A moving-window peak-finding algorithm can be applied to improve layer localization, generating depth maps for the IS/OS junction (b) and the COST layer (c). En-face projections of the detected IS/OS (d) and COST (e) layers span the entire field of view.

2.8 Digital aberration correction (DAC) pipeline

During ORG imaging, various optical aberrations, such as defocus, astigmatism, and higher-order aberrations, can significantly degrade image quality. To mitigate these effects, especially in cases where hardware AO are either limited or absent (as in CoORG imaging), similar to the ocular aberration correction algorithm in full-field swept source OCT [95], we developed a novel digital aberration correction algorithm: Evolutionary Particle Swarm Optimization–Steepest Descent–Conjugate Gradient (EPSO–SD–CG). This algorithm enhances image quality by iteratively searching for the global maximum of an image sharpness metric, effectively correcting aberrations described using Zernike polynomials. Selecting an appropriate number of Zernike terms is crucial

to balance optimization effectiveness with computational efficiency, enabling improved imaging performance in both AO-based and non-AO (CoORG) systems.

2.8.1 Algorithm and validation on synthetic data

The digital aberration-correction module employs a three-stage, hybrid optimizer (EPSO–SD–GBA) that reliably converges to the pupil phase producing the sharpest image without requiring a user-supplied starting guess. First, an evolutionary particle-swarm optimization (EPSO) performs a rapid global search, driving the image-quality metric down by roughly two orders of magnitude (from ~10^{-2} to 10^{-3} in normalized error) and positioning the solution near the basin of the true minimum. The algorithm then switches to a steepest-descent (SD) routine that exploits gradient information to achieve a finer local refinement, pushing the error a further two orders of magnitude (≈10^{-5}). Finally, a gradient-based accelerated (GBA) line search executes a series of damped corrections that quickly oscillate about the optimum, delivering sub-10^{-5} stability in only a few dozen function evaluations. This cascading strategy, coarse global exploration followed by progressively finer local optimization, combines robustness against local minima with the efficiency of deterministic methods, making it well-suited for real-time aberration correction in high-resolution retinal imaging.

To quantify the accuracy of the two-stage optimizer, we applied it to a synthetically blurred test image containing the letter “E” convolved with a known Zernike-mode phase screen, shown in Figure 2.7. In the first stage, evolutionary particle-swarm optimization (EPSO) produced a coarse estimate of the aberration, reducing the objective function from its initial value to 1.9×10^{-3} and yielding a root-mean-square error (RMSE) of 7.0×10^{-4} between the estimated and ground-truth Zernike coefficients. In the second stage, steepest-descent (SD) refinement drove the error down

by an additional four orders of magnitude, achieving a final RMSE of 2.7×10^{-17} and a function value below 3×10^{-3}. The restored image after SD is visually indistinguishable from the ground-truth object, demonstrating that the hybrid EPSO–SD pipeline can recover both the phase aberration and the diffraction-limited image with numerical precision in idealized conditions.

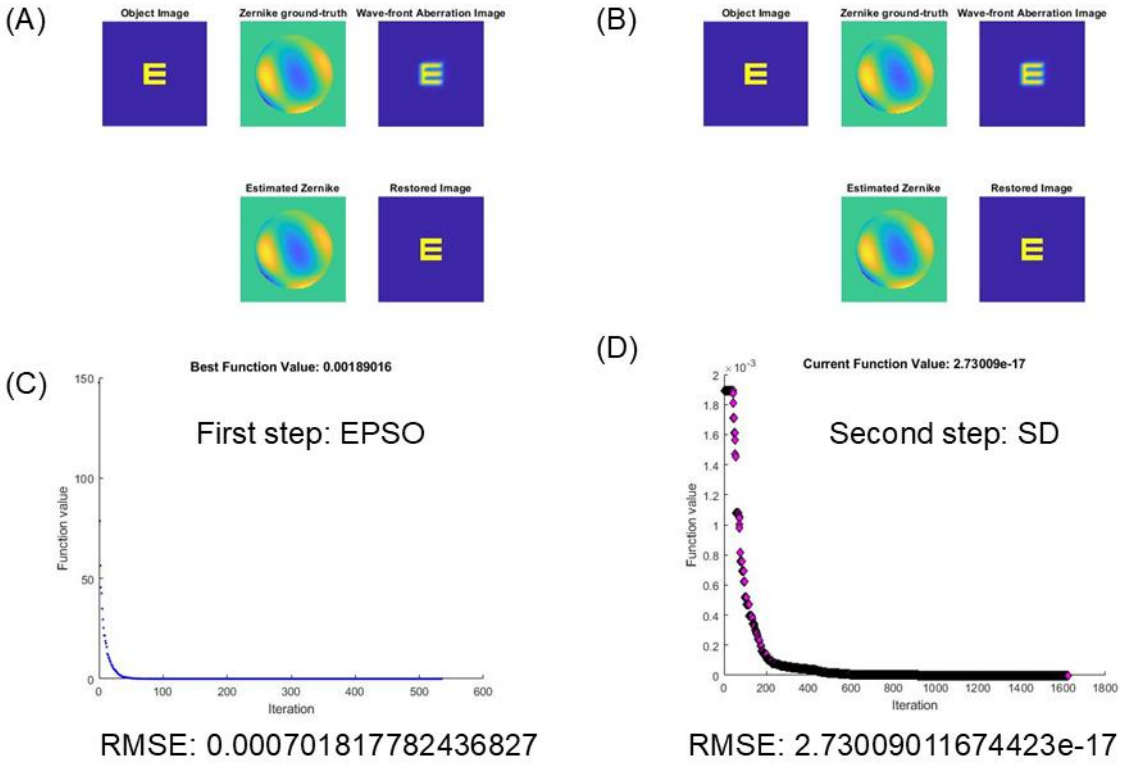


Figure 2.7 Accuracy benchmark of the hybrid optimizer on an artificial dataset. (A) Synthetic object ("E"), ground-truth Zernike phase map, and the correspondingly blurred (aberrated) image. (B) Same triplet after optimization: recovered Zernike map and aberration-corrected image are virtually identical to the ground truth. (C) Convergence curve for the EPSO stage; RMSE after this global search is 7.0×10^{-4}. (D) Convergence curve for the subsequent SD stage; RMSE falls to 2.7×10^{-17}, confirming near-perfect phase retrieval.

2.8.2 Performance on AO-OCT data

To validate the optimizer on real data, we applied it to an AO-OCT volume of the human retina, targeting the reflection intensity-rich ISOS band (Figure 2.8). The raw 512 × 512 × N voxel stack was first partitioned axially into three slabs, upper, central, and bottom, to accommodate depth-dependent aberrations and varying signal levels (Figure 2.8a). Each slab was further divided into sixteen 128 × 128-pixel sub-regions. The hybrid EPSO–SD algorithm was independently executed in each sub-region, employing a 24-term Zernike basis to determine the local wavefront corrections that maximized a spatial-frequency–weighted sharpness metric. Optimization typically converged in fewer than 200 iterations per sub-region, after which the individually corrected sub-volumes were recombined through seamless stitching (Figure 2.8g) into a fully corrected stack. Maximum-intensity projections (MIP) of the ISOS slab before (Figure 2.8c) and after correction (Figure 2.8d) demonstrate the effectiveness of local optimization: the uncompensated MIP shows only mottled speckle, whereas the corrected MIP clearly resolves the cone mosaic across the entire 1.2-deg² field. Compared to global optimization (Figure 2.8f), this sub-region-based method uniformly preserves high-frequency detail, highlighting the importance of spatially adaptive correction for mitigating isoplanatic variations in AO-OCT data.

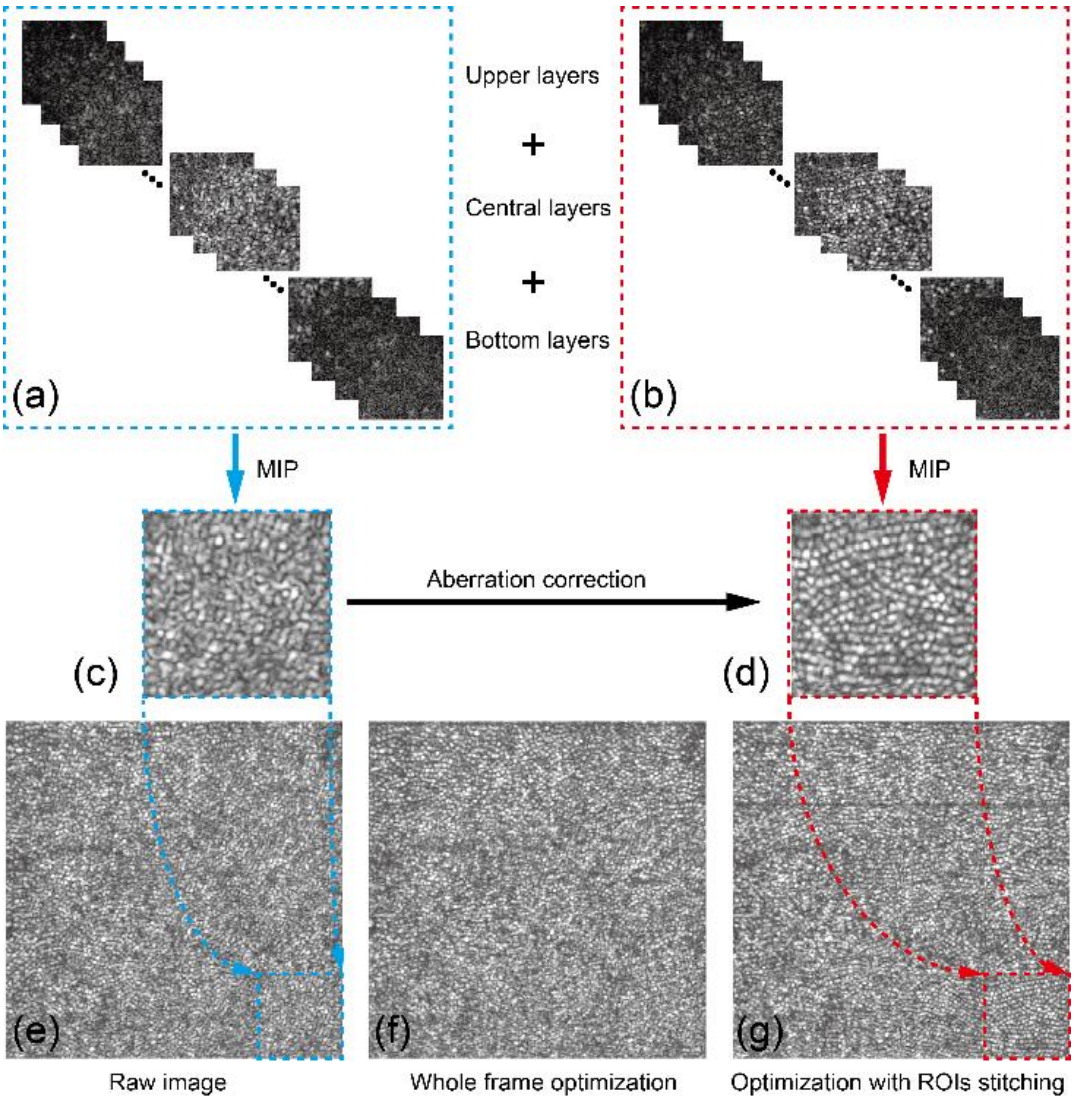


Figure 2.8 Optimization procedure and results for the IS/OS layer in AO-OCT images. (a) The raw AO-OCT image stack was segmented axially into three distinct depth layers: upper, central, and bottom. (b) Each depth layer underwent independent optimization. (c–d) Maximum intensity projections (MIPs) were calculated from optimized sub-regions, each sized 128×128 pixels. (e) The entire imaging field measures 512×512 pixels, divided into 16 sub-regions (g). Optimization was thus performed separately for each of these 16 sub-regions. (f) Final composite image obtained after combining individually optimized sub-regions, demonstrating overall enhancement in image quality.

2.8.3 DAC performance on in-focus foveal AO-OCT images

Furthermore, to evaluate whether digital aberration correction (DAC) provides measurable improvements even under nominally diffraction-limited conditions, we applied the 65-term Zernike optimizer to an in-focus, fovea-centered AO-OCT volume covering a 1.4° field. Although the raw AO-OCT image already displayed a visible cone mosaic, subtle blur and inter-cone speckle obscured clear delineation of cell boundaries across the 512 × 512-pixel frame (Figure 2.9, left). After tile-based DAC, the corrected image exhibited uniformly sharper cone cores and darker inter-cone spaces, as illustrated by improved contrast in three representative 0.20° sub-regions spanning the field, confirming that residual higher-order aberrations were present even in the nominally optimized AO system and effectively removed through digital correction. These results indicate that DAC offers significant benefits for enhancing image quality even in high-quality, on-axis foveal AO-OCT data, complementing and extending hardware-based AO.

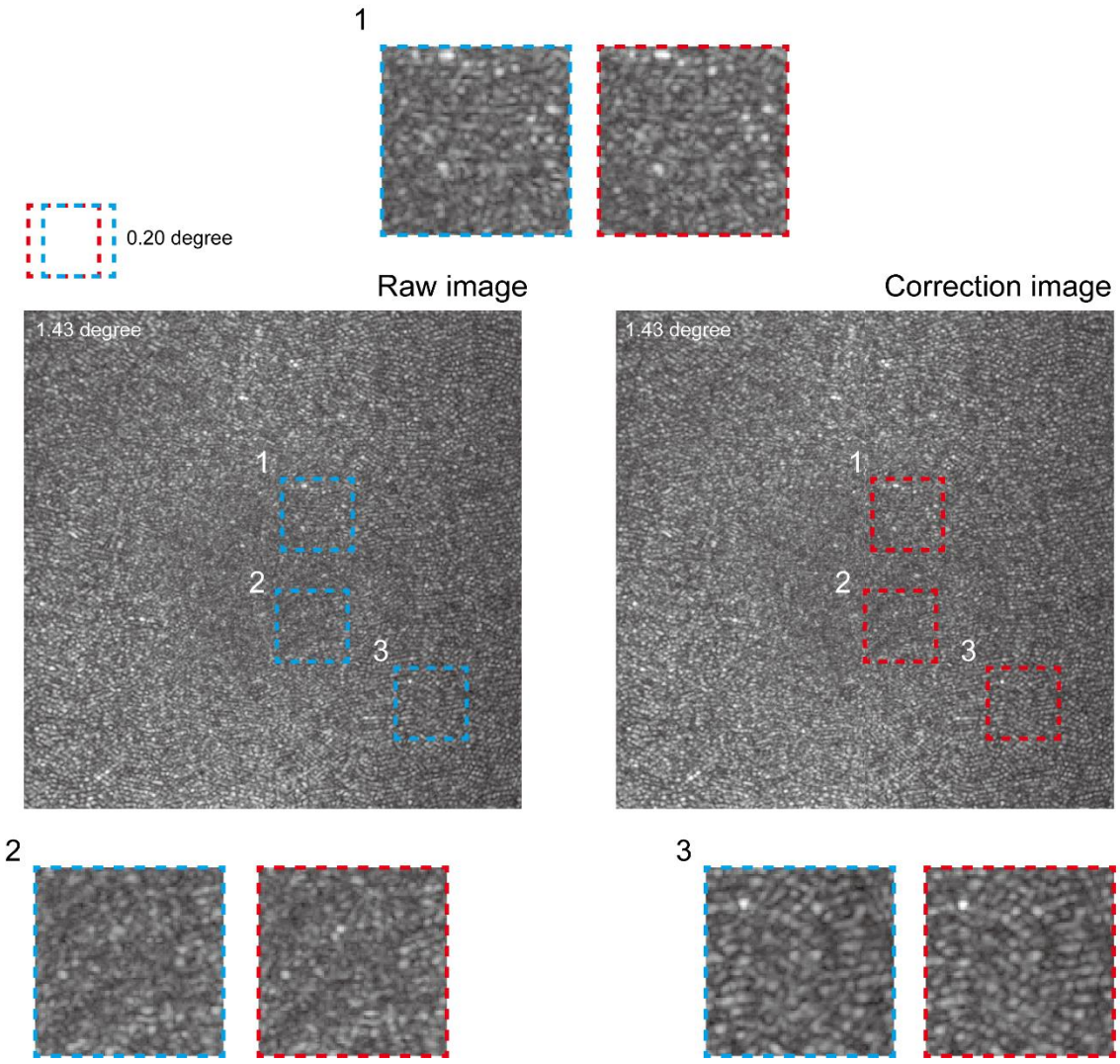


Figure 2.9 Raw (left) and digitally corrected (right) en-face IS/OS projections from a 1.43° AO-OCT volume. Dashed boxes (1–3, 0.20°) mark sub-regions shown enlarged above and below: blue = before correction, red = after. Cone photoreceptors are visibly sharpened, and inter-cone dark spaces deepen after DAC. Optimization used 65 Zernike modes on 128 × 128 tiles, confirming that software correction enhances even hardware-focused, central-fovea images.

2.8.4 Digital correction in CoORG datasets

To determine whether software-based correction alone can restore cellular-level detail in images obtained without hardware adaptive optics, we applied the 36-term Zernike optimizer to CoORG dataset of the parafoveal cone mosaic (Figure 2.10). Four representative 0.20° regions of interest

(ROIs), labeled 1–4 and spanning areas of varying signal quality, were selected for qualitative comparison. In the uncorrected projection (blue boxes), images are difficult to distinguish due to speckle noise and residual ocular aberrations. Following DAC (red boxes), cone clusters become clearly visible as bright, regularly spaced spots separated by darker inter-cone gaps, markedly enhancing overall image contrast across the full 2.5° field. Slight variations in the retrieved local wavefront among the ROIs confirm the presence of isoplanatic differences even within small fields of view. These results suggest that digital aberration correction can partially enhance image quality, enabling the extraction of reliable optoretinograms from CoORG datasets. This improvement might potentially broaden access to functional retinal imaging beyond specialized AO-equipped laboratories.

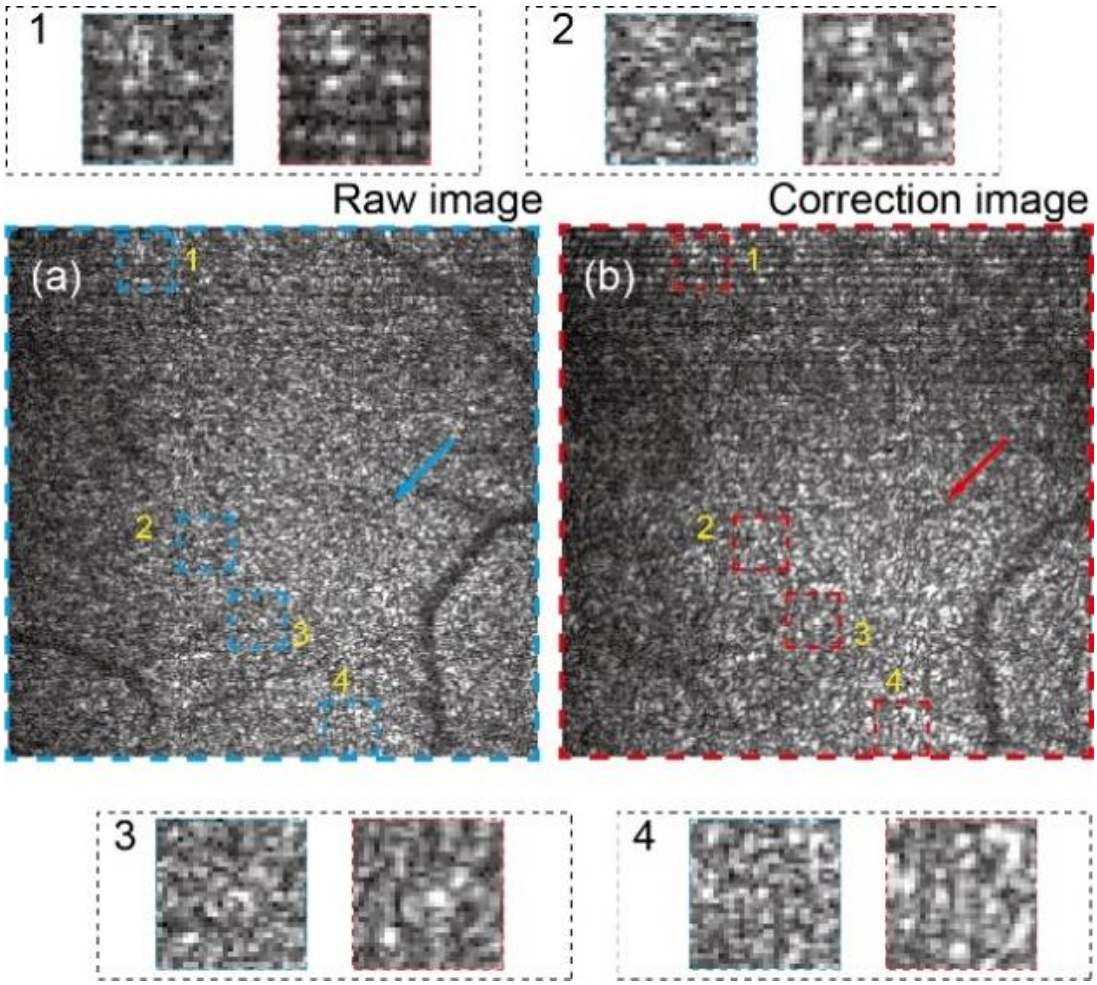


Figure 2.10 Digital aberration correction applied to CoORG data. (a) Raw e*n-face* projection with four ROIs (blue dashed boxes) at eccentricities spanning 1.1–2.5°; (b) projection after 36-term Zernike DAC, ROIs indicated in red; (c) side-by-side zooms (before, blue; after, red) for ROIs 1–4 illustrate the emergence of the cone mosaic post-correction (arrows highlight representative cones). Scale bar for insets: 0.20°.

2.8.5 Current limitations and future refinements

Although the two-stage DAC pipeline robustly restores cone contrast in AO-assisted OCT volumes, its effectiveness is somehow diminished in CoORG data. This reduction can be attributed primarily to two factors. First, the intrinsically lower spatial sampling of CoORG, approximately 3.6 μm lateral resolution, is three to four times coarser than the Nyquist spacing required to resolve

individual cones. Since wavefront-correction algorithms like EPSO–SD rely heavily on high-frequency spatial information to estimate Zernike coefficients, reduced spatial bandwidth results in weaker gradient cues and flatter optimization landscapes, consistent with earlier reports on undersampled coherent-imaging systems [96]. Second, metric non-specificity further limits DAC performance: the Shannon-entropy sharpness metric we employed excels at cellular scales but becomes less discriminative when larger-scale speckle structures dominate image texture instead of the regular periodicity of cones, a phenomenon similarly observed in entropy-based refocusing of vascular OCT datasets [95]. Collectively, these factors explain why DAC in CoORG often yields modest visual improvements and limited SNR gains, underscoring the need for more resolution-specific metrics or a hybrid coarse-to-fine optimization strategy tailored explicitly to wide-field, non-AO OCT datasets.

Chapter 3. Normative characterization of the ORG using CoORG system

3.1 Introduction

In this chapter, we present a comprehensive, population-based characterization of cone ORG in normal controls using our CoORG system. First, we demonstrate the cross-sectional B-scan quality achievable without AO, and establish trial-to-trial repeatability to ensure measurement reliability. Leveraging these validated data, we map normative ORG amplitudes and kinetics across the different retinal meridians and stimuli levels, then benchmark their performance against state-of-the-art AO-based ORG to quantify the variation between different modalities. The core analysis explores inter-individual variability, initially at a global level, then specifically as a function of inherent variation in pre-photoreceptor factors, (such as pupil diameter and axial length) and intrinsic photoreceptor metrics, such as outer segment length under various stimulus-dependent conditions. We synthesize these observations into key determinants that define normal ORG variability, and finally examine how ORG responses affected by healthy aging, including associated changes in cone density, and other potential factors. Collectively, these findings define the dynamic range, spatial distribution, and inter-subject variability expected when employing CoORG for clinical or research applications.

3.2 CoORG cross-sectional B-scan images

Figure 3.1(A) displays an OCT B-scan imaged by the CoORG system, ranging from the fovea to 4.5° temporal eccentricity. The intensity profile in Figure 3.1(B) reveals the peaks of A-lines at various eccentricities, representing the major outer retinal layers. Three dominant peaks, ISOS,

COST, and retinal pigment epithelium (RPE) are evident from the fovea to 1.5°. A fourth peak, indicative of rod outer segment tips (ROST), emerges from 2° eccentricity (shown in black arrow of Figure 3.1(B)), highlighting the instrument's capacity to accurately capture B-scans of major retinal layers.

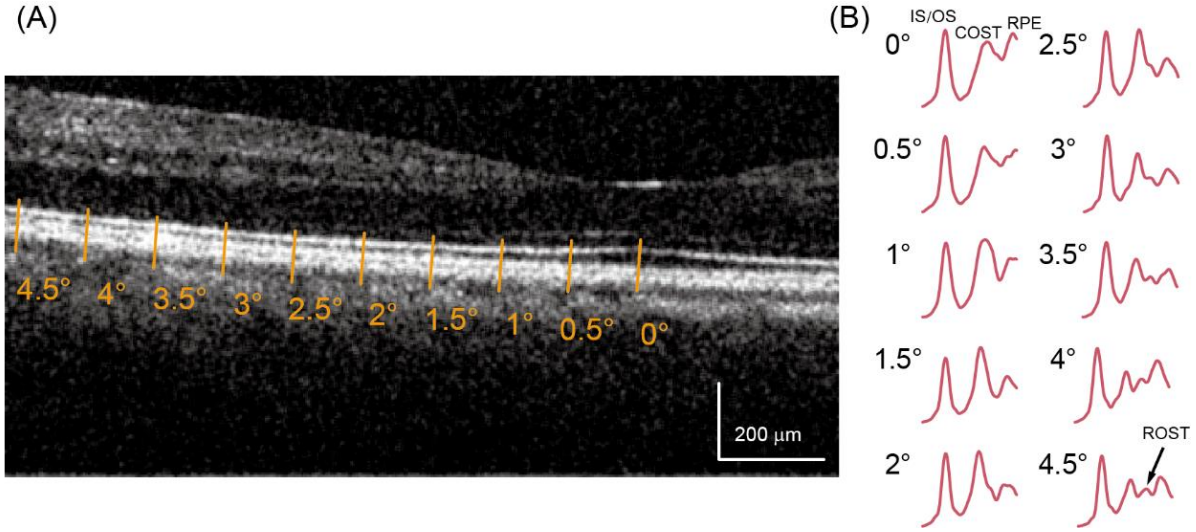


Figure 3.1 Example of a B-scan acquired from the CoORG instrument. Eccentricities are indicated on the B-scan shown in (A), and the corresponding intensity profiles along the A-scan are shown in (B). The peaks correspond to the major outer retinal layers shown in the black arrows.

3.3 ORG trial-to-trial repeatability

Repeatability was evaluated through 5 measurements and two bleach conditions for a subject, as shown in Figure 3.2. Each panel depicts the ΔOPL change in the outer segment (y-axis) against time post-stimulus onset (x-axis). The curves generally mirror published reports [55,62], displaying an initial ΔOPL dip post-light onset, followed by a rapid rise and plateau within approximately 300 ms. The ΔOPL's saturated amplitude and slope of rise are known to increase with stimulus bleach level [55], and they exhibit this trend across eccentricities as bleach is increased. For a given

stimulus bleach, the amplitude and slope both decrease in magnitude with increasing eccentricity. Figure 3.2(A) and (B) illustrate high and low bleach levels from 1° to 4° temporal eccentricity, with each trace in the panels representing a single measurement, demonstrating an overall consistent repeatability. The mean ΔOPL across all trials for both bleach levels are presented in Figure 3.2(C) and (D). Time-averaged standard deviations between trials, calculated for each 0.5° eccentricity step, ranged from 6.5 to 22.2 nm (high bleach) and 4.8 to 13.0 nm (low bleach), averaging ±13.34 nm and ±9.68 nm for high and low bleach levels, respectively. Across all subjects, the average inter-subject standard deviation was ±8.3 nm (range: 2.1 - 23.5 nm) for 20 ms flashes and ±4.5 nm (range: 1.0- 18.8 nm) for 10 ms flashes, indicating high ΔOPL vs. time repeatability in CoORG.

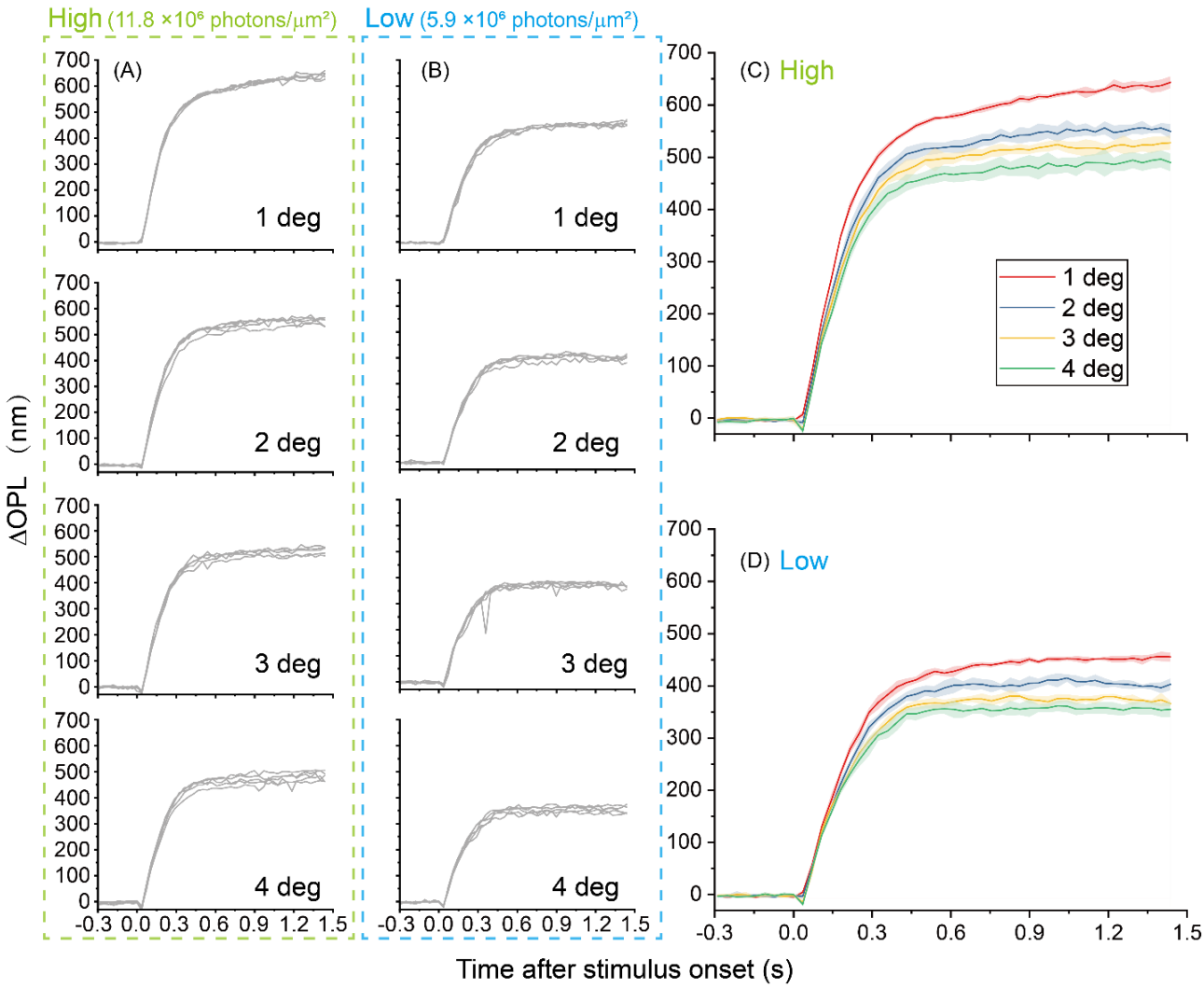


Figure 3.2 Light-evoked ΔOPL for a subject along the temporal meridian. Column A and column B show plots of 5 successive repeat trials at different eccentricities for high and low bleach levels, respectively where each curve represents a single trial. The high and low bleach correspond to 8.8×10^6 and 4.4×10^6 photons/μm^2 respectively for this subject. Plot C and D are the mean of the five repeat measurements for both bleach levels at each eccentricity. The shaded area surrounding the solid traces represent ±1 standard deviation.

3.4 ORG variability across retinal meridians

To evaluate dependence on retinal eccentricities at different meridians, a subject was imaged at the inferior and temporal eccentricity with the same high bleach level. The maximum saturated ΔOPL

was determined from the ORG trace by averaging the ΔOPL between 1.14 and 1.47 seconds and then plotted for each meridian versus eccentricity (Figure 3.3). The standard deviations were slightly higher for the temporal meridian compared to the inferior (±5.80 nm inferior vs. ±8.13 nm temporal). However, a two-tailed paired t-test showed no significant difference between the two groups ($p = 0.71$), suggesting a similarity in the saturated amplitude of ΔOPL between the two meridians.

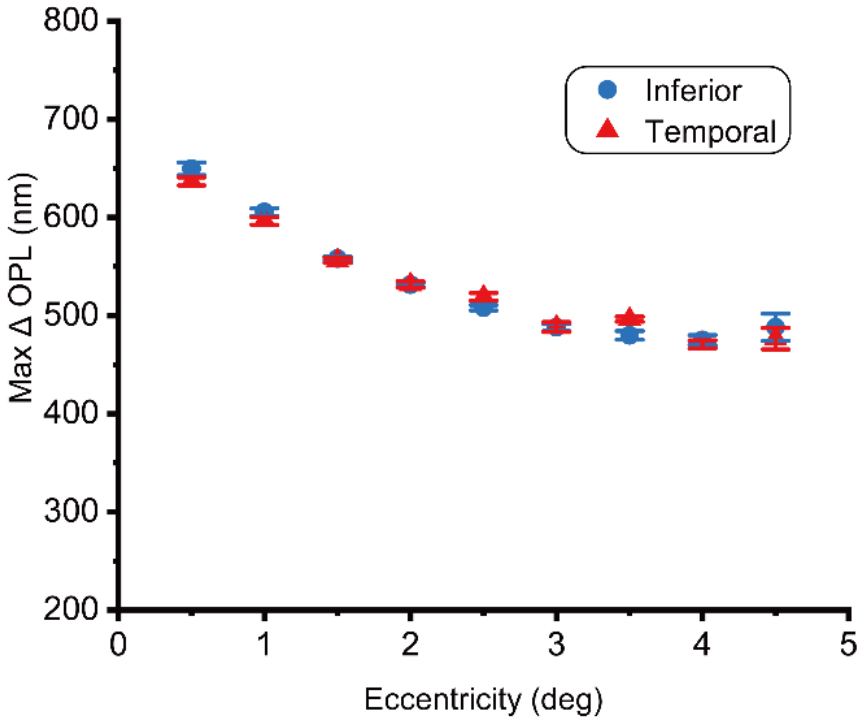


Figure 3.3 Comparison of ΔOPL changes versus eccentricity for inferior and temporal meridians.

3.5 The comparison between CoORG and AO-based ORG

ORG response amplitude from extended field CoORG without AO were compared to AO-based ORGs at cellular scale at 1.5°, 2.5°, and 3.5° inferior eccentricity using the same imaging protocol. The AO-OCT *en face* image at the ISOS was aligned with the CoORG's *en face* image of the same layer (Figure 3.4(B)), with a larger AOSLO montage facilitating precise alignment through to

vasculatures. ΔOPL was comparable between AO-ORG and CoORG for the same subjects (Figure 3.4(A)), with average standard deviations of ±15.2 nm (CoORG) and ±12.42 nm (AO-ORG) for S1, and ±7.6 mm and ±12.65 mm respectively for S2. Although there was significant agreement between coarse-scale ORGs and cellular resolution AO-ORGs, AO-based measurements for S2 were consistently lower, with the maximum ΔOPL difference observed at 3.5° eccentricity equal to 62 nm.

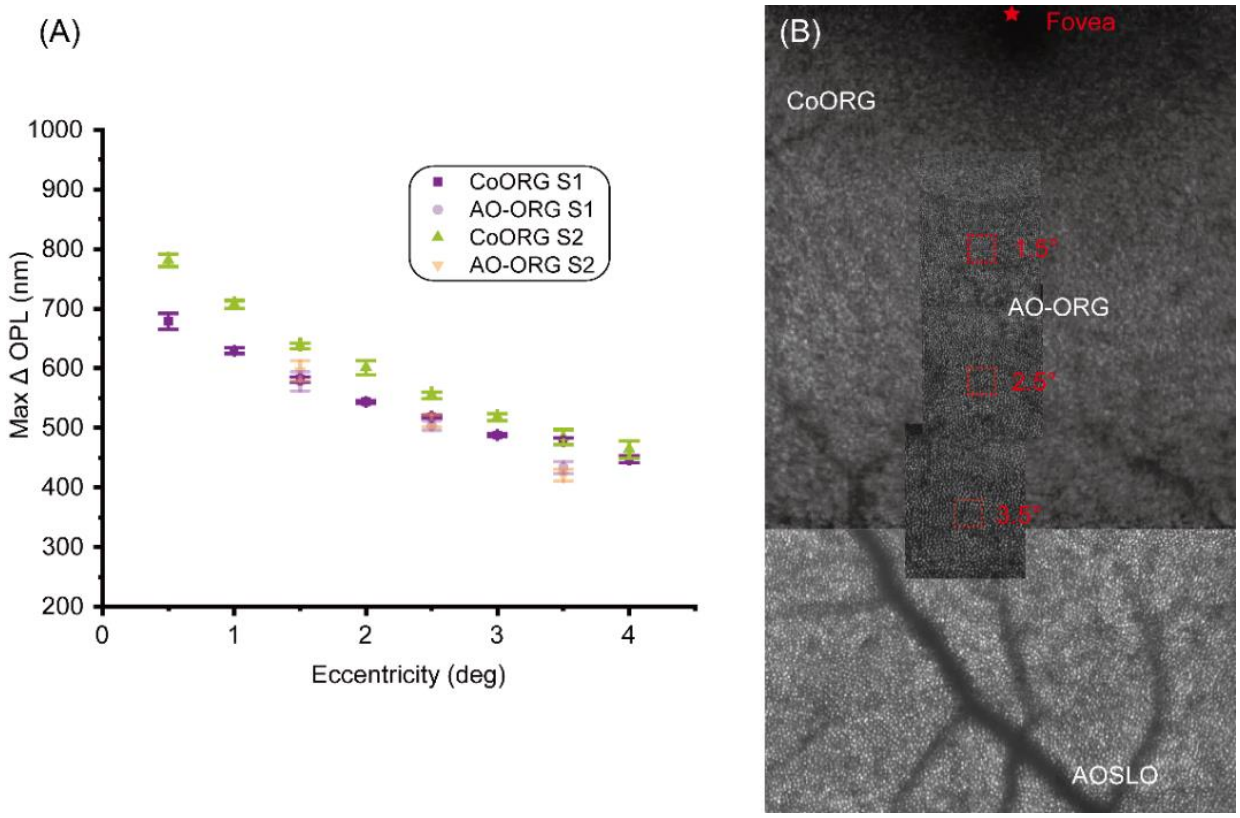


Figure 3.4 Comparison with AO and with CoORG in the same subjects S1 & S2 is shown in (A). (B) En face overlaying image of CoORG, AO-ORG, and AOSLO to facilitate alignment between them. The size of the red square is 0.3×0.3 deg^2.

3.6 Inter-individual variation in ORG

Figure 3.5 plots the mean saturated ΔOPL in the temporal meridian for 12 subjects, displaying a decrease with increasing eccentricity up to 5 deg. The highest variation among subjects occurred

at 0.5° eccentricity, with ±88 nm and ±66 nm (standard deviation) for high and low bleach levels respectively. While variability decreased with eccentricity for high bleach, it remained similar for low bleach, ranging from 88 to 31 nm (high bleach) and 66 to 17 nm (low bleach). One subject had a significantly lower ΔOPL magnitude (indicated by the pink left triangle) which is attributed to the subject's relatively smaller dilated pupil size (6.82 mm) and longer axial length (25.32 mm) and resultant lower effective stimulus bleach (22.6% lower than average photon density).

We aimed to identify contributing factors to the observed variations in ORG among healthy subjects. A five-factor ANOVA was conducted to analyze the impact of five variables on the ORG signal, with two factors (pupil size, axial length) and two fixed factors (bleach level and eccentricity). The analysis [97] found bleach level ($p < 0.05$), and eccentricity ($p < 0.001$) to be significant in determining saturated ΔOPL.

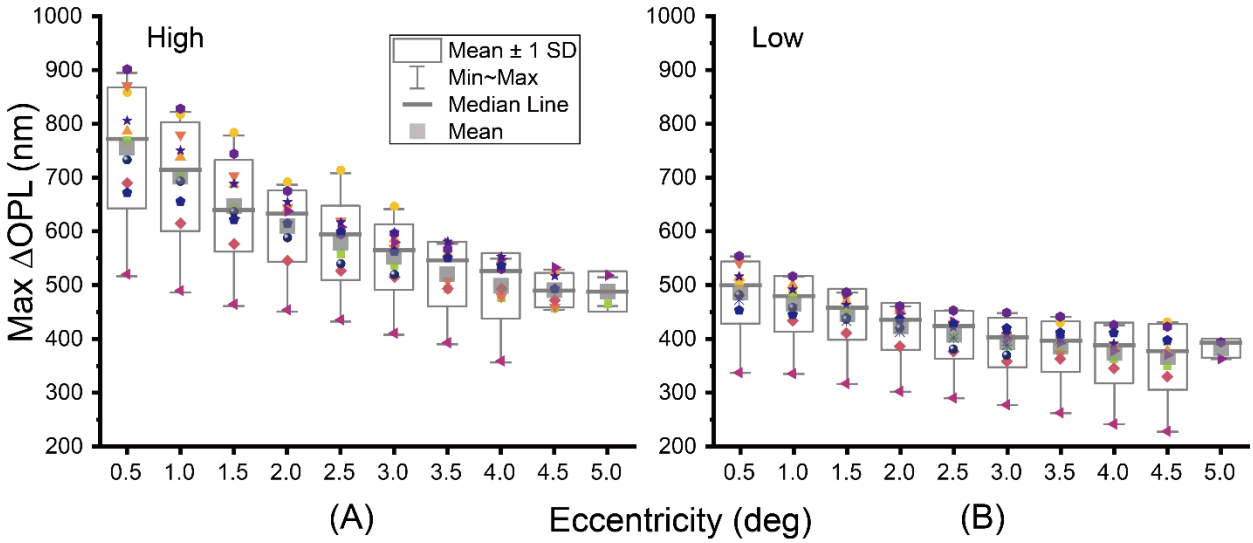


Figure 3.5 Box and whisker scatter plots with averaged maximum ΔOPL from 12 subjects for high (A) and low (B) bleach levels. One subject's OPL was significantly lower than others (pink left triangle), due to a smaller pupil size and longer axial length translating effectively to a lower photon density on the retina.

3.6.1 Variation of ORG with photon density

While pupil size and axial length individually had no significant effect on the ORG signal, their interaction did influence it significantly ($p < 0.001$, ANOVA). Effective photon density for each subject and bleach level was calculated, considering both factors. Saturated ΔOPL versus eccentricity, divided into four photon density bins for both bleach levels, is depicted in Figure 3.6 Paired t-tests conducted for the bins of both bleach levels revealed significant differences ($p = 0.001$ for high, $p = 0.0008$ for low), indicating an overall decrease in saturated ΔOPL with reduced photon density. Near the fovea, photon density had a more pronounced impact on ΔOPL, with a range of 467 to 794 nm (a 1.7x change from the lowest to highest photon density). This range contracted to 362 to 496 nm as eccentricity increased.

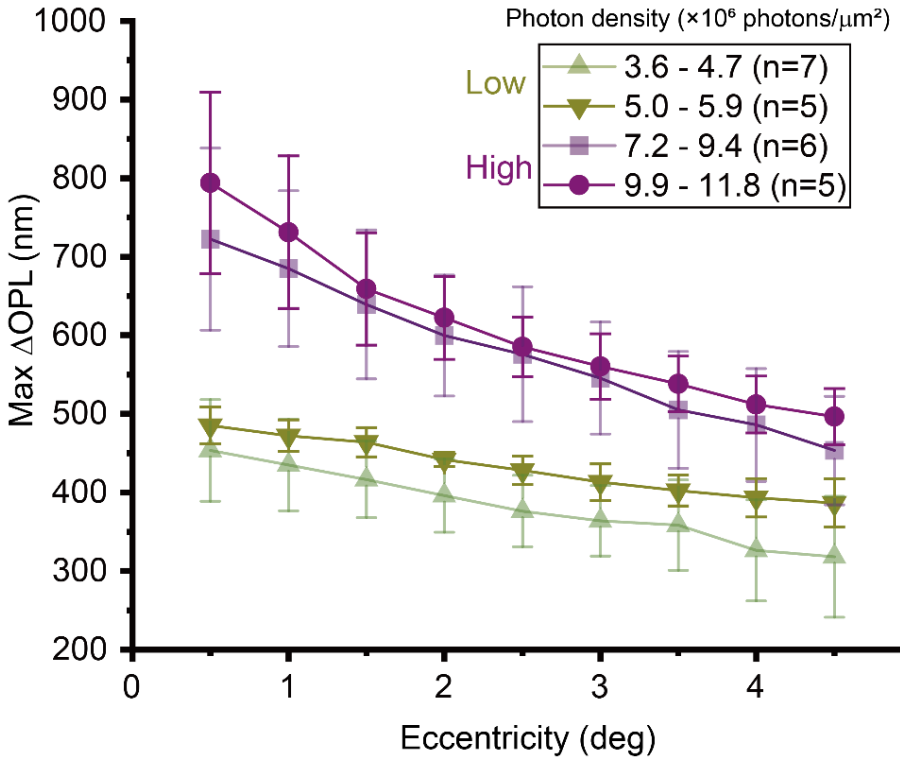


Figure 3.6 The variation in maximum saturated ΔOPL vs. eccentricity for different photon density bins calculated specific to each subject. Data points are the mean in each bin, and error bars represent ± 1 standard deviation.

3.6.2 Variation of ORG with outer segment (OS) length

The amplitude of saturated ΔOPL diminishes with increasing eccentricity independent of bleach level, as observed in Figure 3.3 – Figure 3.6 To explore whether variation in cone outer segment (OS) length is a contributing factor, we analyzed cone OS lengths from the CoORG B-scans of each participant. Figure 3.7 plots the maximum ΔOPL in 0.5° bins against outer segment lengths for all subjects. Linear regression, applied to both high and low bleach conditions, yielded R^2 values of 0.65 and 0.53, respectively. Upon excluding an outlier with significantly lower effective retinal photon density (refer to section 5.5), these R^2 values increased to 0.75 for both bleach levels, with all regression coefficients being statistically significant ($p < 0.0001$).

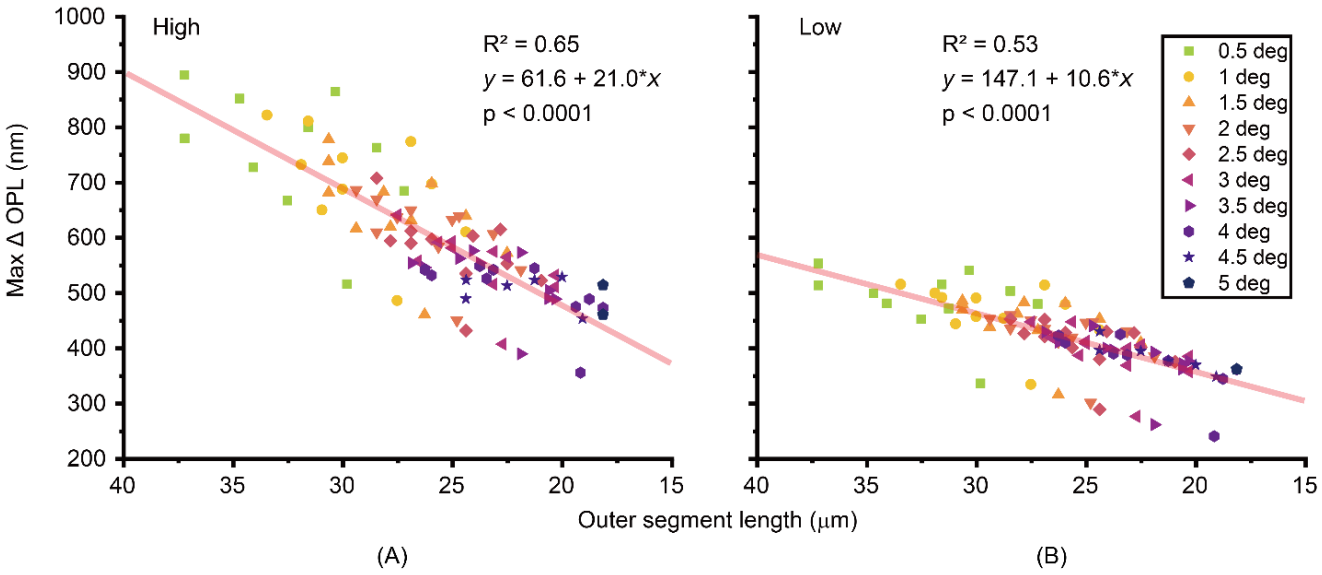


Figure 3.7 The variation in maximum saturated ΔOPL versus outer segment length for high (A) and low (B) bleach strengths. Each data point indicates measurement from a single subject & eccentricity, while markers and colors indicate different eccentricity bins. A linear regression fit to all data is shown in both plots, along with the coefficient of determination and the equation for the linear fit.

3.6.3 Variation of ORG across different nominal photon densities

Increasing the retinal photon density drives a corresponding rise in the saturated ORG amplitude, but the gain depends on retinal eccentricity. Figure 3.8 shows ORG amplitudes for each individual based on effective photon density (calculated from pupil diameter and axial length) at three different nominal photon densities (low: 4.4; middle: 8.8; high 14.2×10^6 photons/μm^2) from nine parafoveal locations (0.5°–5°). Across the full data set the max ΔOPL scales quasi-logarithmically with photon density over two orders of magnitude. ORG amplitude closer to the fovea exhibit higher saturation plateaus than their peripheral counterparts , which may be explained by shorter outer segments peripheral to the central fovea.

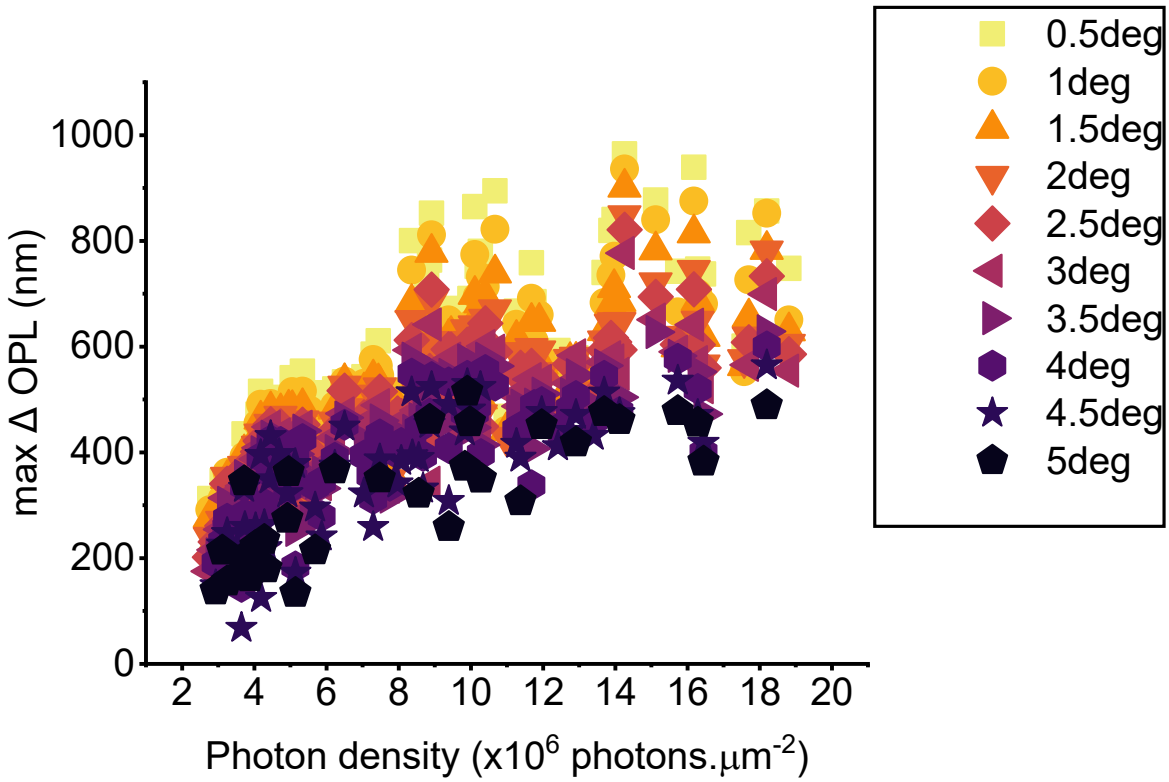


Figure 3.8 Relationship between retinal photon density and maximum cone ORG amplitude. Scatter plot of photon density at the x-axis versus max ΔOPL for 0.5° FOV interval recorded at eccentricities

from 0.5° (yellow squares) to 5° (black pentagons); marker colors transition from yellow to violet with increasing eccentricity, as indicated in the legend.

The structure-function slope (SF-slope) in different stimulus groups are shown in Figure 3.9. The data reveal a nearly linear dependence of the max ΔOPL on OS length, modulated by retinal photon density. Across the sampled eccentricities, the relationship can be expressed as:

$$Max\Delta OPL = k \times OSL \tag{3.1}$$

where the proportionality constant k increases with stimulus level. The slope is 12.6 nm · μm^{-1} at the lowest nominal retinal photon density (4.4 × 10^6 photons · μm^{-2}), whereas at intermediate and high bleaches (8.8 × 10^6 and 14.2 × 10^6 photons · μm^{-2}) k rises to 17.0 and 20.5 nm · μm^{-1}, respectively. Thus, longer outer segments generate larger absolute optical-path-length changes, and brighter flashes amplify this structural scaling. The finding supports a simple linear model in which stimulus-driven nanometer elongation accumulates along the axial stack of discs; for a given fractional increase in osmotic pressure, cones with longer outer segments and higher absorbed-photon counts exhibit proportionally greater ΔOPL magnitudes.

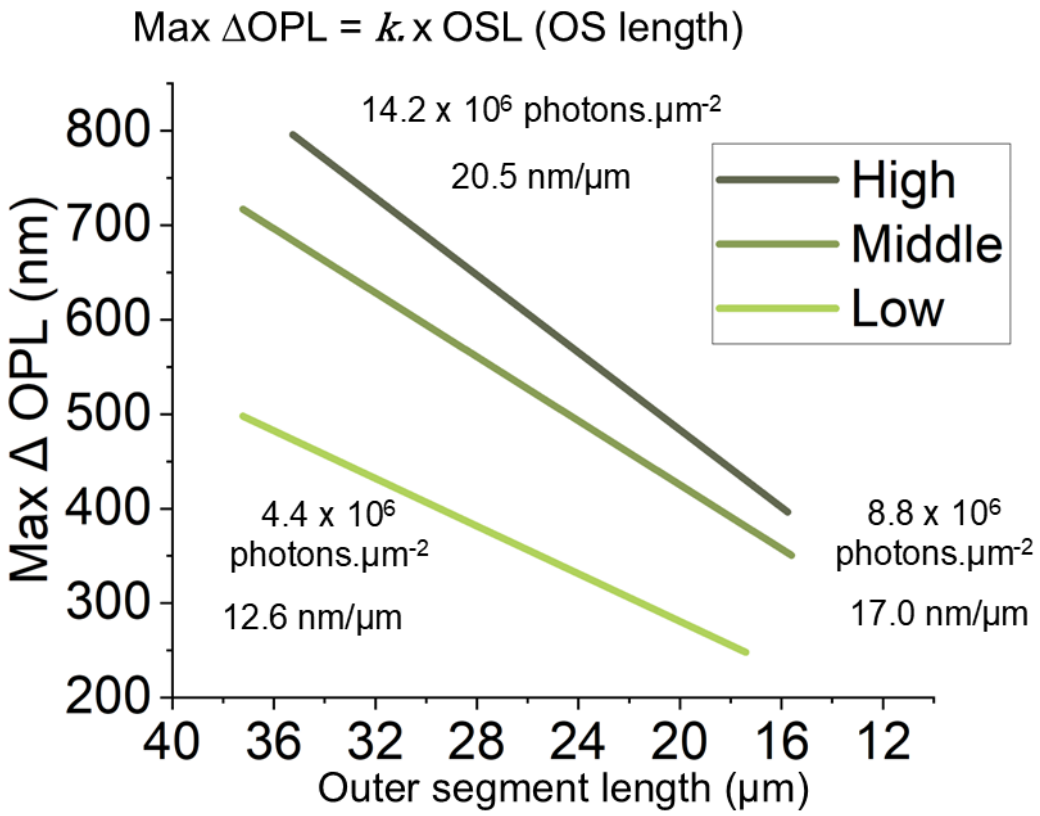


Figure 3.9 Linear scaling of saturated ORG amplitude with cone OS length. Maximum optical path length change (max ΔOPL) plotted against measured OSL for three photon-density conditions: low (light green), middle (olive), and high (dark green).

3.7 Summary of the key factors in the cone ORG

Based on the parameters discussed above, normal variability in cone ORG arises from two primary classes of influence: pre-photoreceptor factors and intrinsic photoreceptor properties, outlined in Figure 3.10. Pre-photoreceptor factors dictate the effective photon density of the stimulus that reaches the outer segments, encompassing: (i) stimulus characteristics, including flash radiant power, pulse duration, and spectral power density which collectively determine the incident photon flux; and (ii) ocular media and geometry, such as pupil aperture, axial length, and the spectral

transmittance of the cornea and lens, shown in Figure 3.10(A)-(B). Specifically, larger pupils and shorter axial lengths concentrate photons into a smaller retinal area, increasing photon density, while age-related lens yellowing or cataract reduces photon flux, resulting in substantially diminished ORG amplitudes even when external stimuli remain constant (Figure 3.10(C)). After photons reach the cones, ORG amplitude and dynamics are further shaped by intrinsic photoreceptor morphology and optical properties, displayed in Figure 3.10(D). Along the retinal eccentricity gradient from fovea to periphery, inner-segment (IS) diameters increase, and outer-segment (OS) lengths decrease, modifying the optical path length, scattering behavior, and Stiles–Crawford ("directionality") Effect (SCE). These structural and optical variations influence both the initial nanometer-scale mechanical response and the slower osmotic swelling component of the ORG, collectively defining the normal range of ORG responses as a function of retinal location and age-related factors (lens transmittance, etc.).

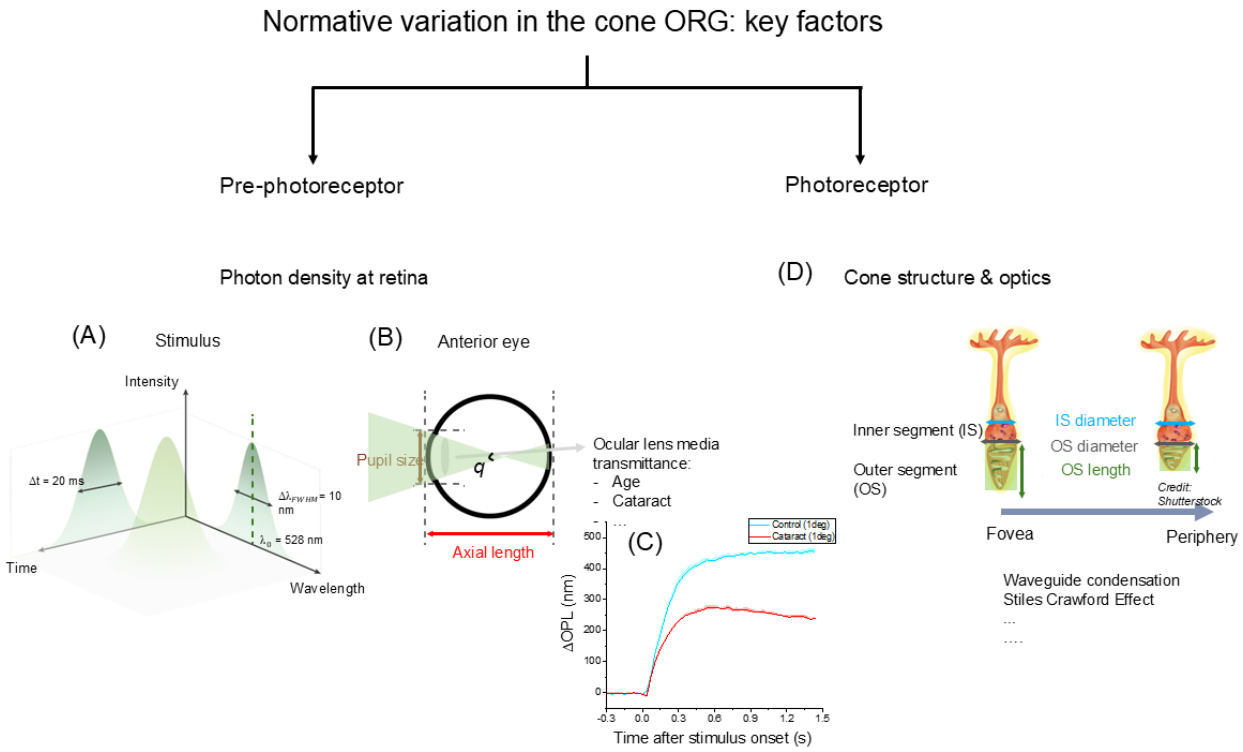


Figure 3.10 Schematic summary of factors that shape the normal variability of the cone ORG. Pre-photoreceptor influences (left) govern the photon density reaching the retina: panel A illustrates how flash intensity, pulse duration (Δt) and spectral bandwidth ($\Delta\lambda$) and central wavelength (e.g., λ_0 = 528 nm) jointly define the incident photon dose, while panel B shows anterior-eye optics in which pupil size, axial length (q) and age- or cataract-related lens transmittance modulate that dose. Panel C plots represent ΔOPL traces from a control eye (blue) and a cataractous eye (red), demonstrating the amplitude reduction caused by diminished lens transmission. Photoreceptor-intrinsic factors (right) further modulate the response: panel D depicts eccentricity-dependent changes in cone morphology, notably shorter outer-segment (OS) lengths, and optical phenomena such as waveguide condensation and the Stiles–Crawford effect; together these structural and optical gradients influence both the fast mechanical and slower osmotic components of the ORG.

3.8 ORG as a function of age

With the median age of global population on the rise, understanding how normal aging affects visual function becomes increasingly important. Even without overt retinal disease, the aging eye undergoes subtle but cumulative anatomical and physiological changes that alter photoreceptor responses to light. ORG, which measures nanometer-scale photoreceptor deformations in response to visual stimuli, is uniquely sensitive to these age-related changes. By around age 60, the retina receives approximately one-third of the light it did in youth [98], primarily due to age-related pupil constriction and lens yellowing. These factors directly reduce incident retinal photon density [99], while other physiological factors, such as impaired photopigment regeneration, Stiles-Crawford effect, and waveguide condensation, may alter the mechanical responsiveness of cone OS, collectively reshaping the ORG amplitude. Indeed, preliminary studies suggest chronological age significantly influences cone ORG amplitude and kinetics even in healthy individuals [85]. In this section, we first characterize the ORG changes observed with normal aging, and then

systematically explore candidate structural and optical factors, such as pupil size, axial length, cone density, and lens transmission, to clarify their contributions to the age-related ORG properties.

3.8.1 ORG response reduces with age

For three stimulus bleach levels, we measured ORG response and OS length for older participants and younger controls, as shown in Figure 3.11. Under all stimulus conditions, younger individuals exhibited higher SF-slopes (larger ΔOPL per unit OS length) and lower intercepts, indicating stronger OS length-dependent responsiveness. Consequently, age-related ORG reduction primarily reflects a uniform reduction in ORG amplitude rather than altered scaling dynamics. Across the three bleach levels, the average ORG amplitude reduction in the older group was approximately 25%. Notably, Figure 3.11(C) illustrates that regions closer to the fovea exhibit relatively greater ORG reductions, possibly due to a stronger OS length-dependent responsiveness in younger subjects or because ORG amplitudes have saturated in peripheral regions with shorter OS lengths. The physiological mechanisms underlying this localized loss warrant further investigation.

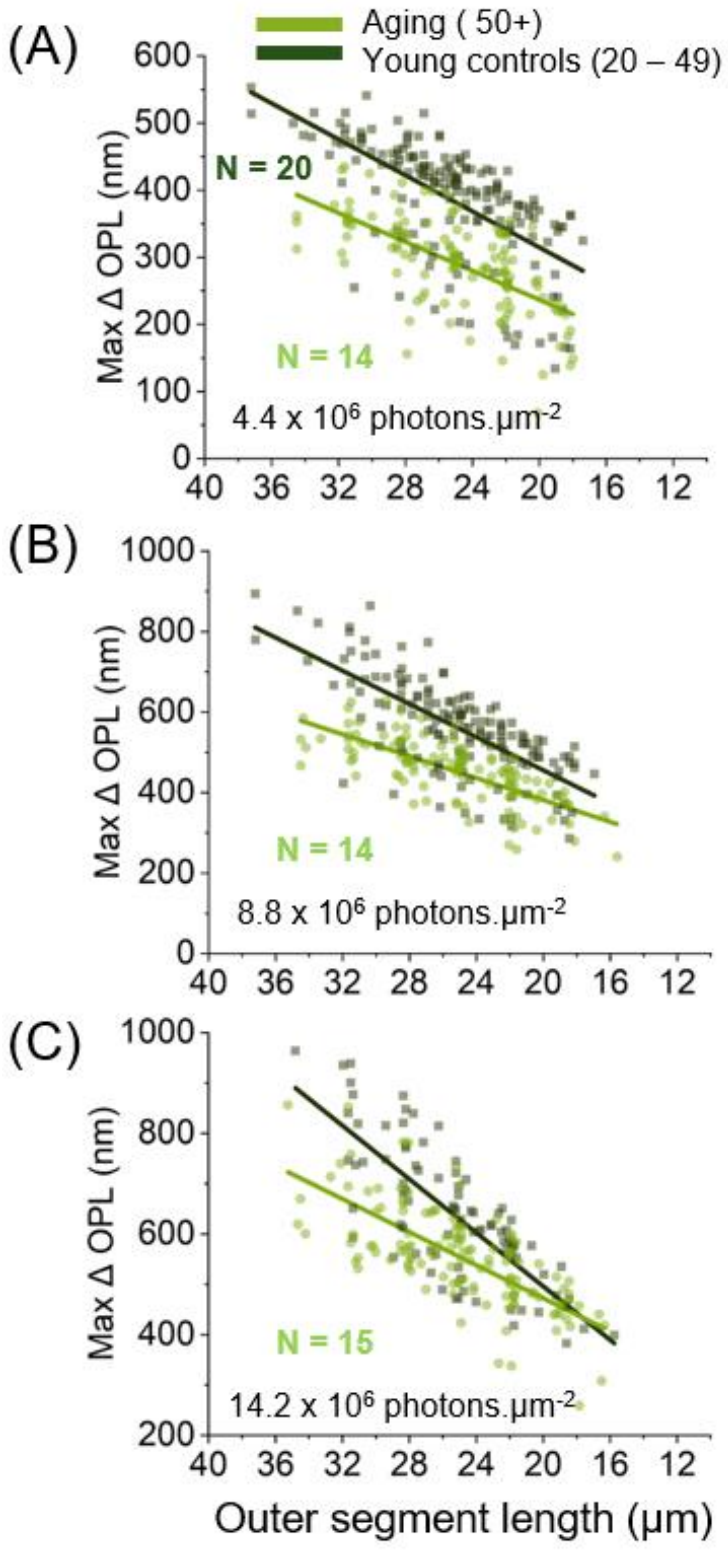


Figure 3.11 Effect of age on the relationship between ORG amplitude and OS length. Scatter plots comparing ORG amplitude (max ΔOPL) against photoreceptor OS length for two age groups—

participants 20- 49 years (dark green squares, sample sizes indicated) and older than 50 years (light green circles)—in three stimulus conditions : (A) 4.4×10^6 photons/μm², (B) 8.8×10^6 photons/μm², and (C) 14.2×10^6 photons/μm² nominal retinal photon density. Solid lines represent linear fits for each group.

Aging cones generate lower ΔOPL for a given OS length and display a shallower SF-slope, leading us to hypothesize that age-related functional attenuation may result from factors such as reduced anterior pupil diameter and lens transmission, decreased cone density, or impaired OS length-dependent photoreceptor recovery dynamics. However, Figure 3.11 illustrates that, for any given retinal photon density, the relationship between ORG amplitude and OS length (the SF-slope) remains consistently shallower in older participants compared to younger controls. Increasing photon density from 4.4×10^6 to 14.2×10^6 photons/μm² elevates both regression lines in parallel but does not narrow the gap between age groups. If reduced cone packing were the primary reason for weaker ORG responses in older eyes, we would expect SF slopes from both cohorts to converge at fixed photon density, as each cone would absorb a similar photon flux regardless of spacing between neighbors. However, Figure 3.12 reveals only a modest, uniform reduction in cone density (~10–15%) across 1–5° eccentricity in older eyes—far too small to explain the observed ~30–40% decrease in ORG amplitude at comparable OS lengths. These findings suggest that other age-related factors, such as reduced pupil diameter, decreased lens transmission, or alterations in phototransduction efficiency, rather than changes in cone sampling density, are primarily responsible for the diminished ORG amplitudes observed in healthy aging.

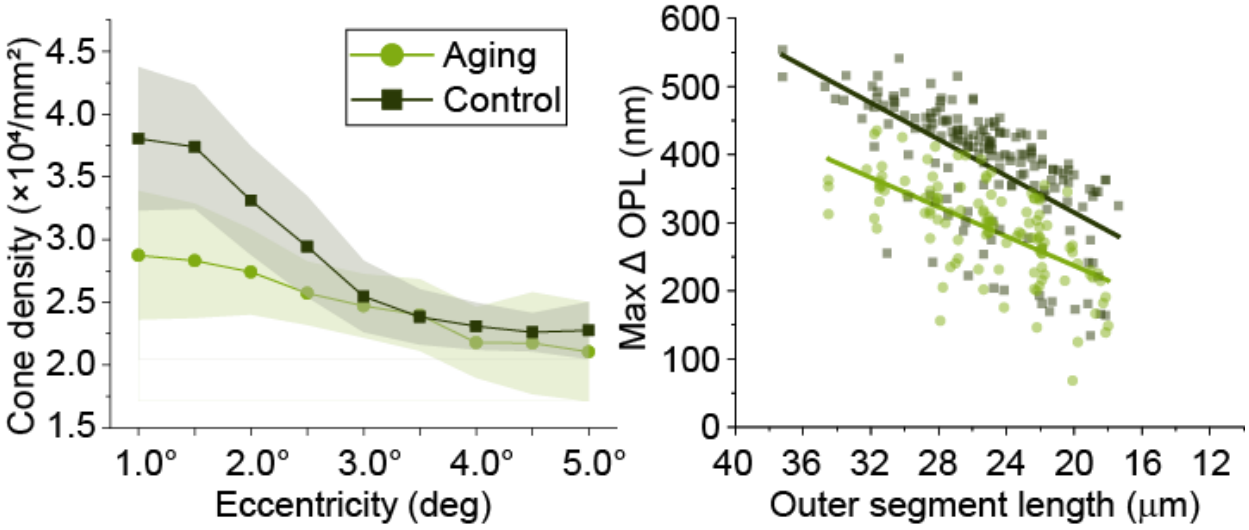


Figure 3.12 Impact of healthy aging on cone structure and ORG response. Left: Mean cone-density profiles versus eccentricity for the aging cohort (light-green circles, age range: > 50 years old) and the younger control group (dark-green squares, age range: 20 – 50 years old). Shaded regions represent ±1 SD. Both groups show the expected decline in density with distance from the fovea, while the aging eyes exhibit a consistent downward offset across the parafoveal band. Right: Scatter-plot of ORG amplitude (max ΔOPL) versus OS length (eccentricity range: 1° to 5°) at the lowest nominal photon density stimulus condition (4.4 × 10^6 photons/μm²); solid lines are linear fits for each cohort.

Table 3.1 demonstrates that pupil diameter is the primary parameter differing significantly between age cohorts, and this difference alone largely accounts for the observed reduction in retinal photon density and the resulting attenuation of ORG amplitude in older eyes. After mydriasis, older participants had a mean pupil diameter of 6.47 ± 1.04 mm, approximately 15% smaller than the 7.57 ± 0.55 mm recorded in younger controls. Because retinal photon flux scales with pupil area, even this modest diameter reduction lowers effective photon density by nearly one-third, as indicated by the calculated photon dose dropping from 15.0 ± 1.8 × 10^6 photons/μm² in controls to 12.5 ± 2.6 × 10^6 photons/μm² in the aging group. In contrast, axial length (24.1 mm vs. 24.2 mm) and cone OS length (23.5 μm vs. 23.1 μm) are nearly identical between groups, and are

therefore less likely to drive ORG response attenuation in the older age group. We therefore conclude that a decreased in dilated pupil diameter, and the resultant decrease in effective retinal photon density—is the primary driver of diminished ORG responses in healthy aging. The residual differences that persist after normalizing for photon density likely reflect secondary factors, including decline in lens transmission , alterations in photopigment regeneration kinetics, or age-related changes in OS biomechanics. These possibilities are further explored in the subsequent section.

Table 3.1 The potential factors between aging and young control

Potential factors	Ages 50+ (N=15)	Ages 20-49 (N=24)
Dilated pupil size (mm)	6.47 ± 1.04*	7.57 ± 0.55
Axial length (mm)	24.13 ± 1.01	24.15 ± 1.06
Photon density ($\times 10^6$ photons/ μm^2)	12.54 ± 2.58*	14.98 ± 1.80
OS length at 3° temporal (μm)	23.47 ± 1.89	23.10 ± 2.08

*: significant, $p < 0.01$

3.8.2 Summary of age-related decrease of ORG response

Based on the data summarized in Table 3.1, we next explore additional factors that might contribute to age-related reductions in ORG amplitude. A comprehensive overview of measured ocular parameters and relevant insights from the literature are provided in Table 3.2. From prior studies, it is known that aside from anterior ocular parameters such as pupil size, structural features like cone diameter and OS length remain largely stable with normal aging.

Several key physiological changes occur with aging. First, resting pupil diameter decreases gradually—a phenomenon known as senile miosis—which subsequently causes a quadratic

reduction in the density of photons reaching photoreceptors [100]. Although axial length measurements initially suggest slight shortening in older adults, such apparent changes are typically attributed to generational differences (e.g., reduced stature or lower myopia prevalence in older cohorts) rather than genuine anatomical shrinkage [101]. Controlling for these biases, true axial length remains largely stable throughout adulthood. Additionally, histological studies indicate that cone OS length and central cone packing remain relatively constant with age[102-105], though a modest peripheral cone-density reduction (~0.2% annually) has been documented[99], and an AOSLO-based cone density study shows declining density in <1.5° retinal eccentricity[106], a trend that mirrors our own observations in Figure 3.12.

Significant age-related alterations occur in ocular media. Crystalline lens yellowing substantially reduces retinal photon delivery, particularly affecting shorter wavelengths. For example, lens transmission at approximately 480 nm diminishes from around 80% in youth to 20–30% by the eighth decade [107]. Moreover, lens thickness continuously increases throughout life [108], and vitreous humor undergoes progressive liquefaction (synchysis senilis) [109]. Age-associated accumulation of lipofuscin within the retinal pigment epithelium (RPE) [110] and slowing of the visual cycle also occur [111], affecting photopigment regeneration and consequently prolonging dark adaptation times [112].

Integrating these insights with our measured ORG data, we estimate that percentage of reduced pupil diameter (and thus lower effective retinal photon density) in aging group is 16%, which accounts for approximately 64% of the total observed ORG amplitude reduction (of the ~25% overall ORG reduction with age). Lens yellowing and reduced optical transmission likely explain an additional ~4% [107]. The remaining 20% reduction remains unexplained by these age-related factors, suggesting that other physiological changes (e.g., vitreous liquefaction, RPE lipofuscin

accumulation, slowing of the visual cycle) might collectively contribute to the residual ORG attenuation. These unresolved factors merit further investigation to fully characterize the origins of age-related photoreceptor dysfunction.

Table 3.2 A comprehensive summary for age-related parameters

Parameter	Change with age
Pupil size (measurable)	Decreases[100]
Axial length (measurable)	Minimal change[101]
Outer segment length (measurable)	Insignificant difference[102-104]
Cone diameter	Minimal change[105]
Cone density (measurable)	Decreases[106]
Lens transmission	Decreases, especially for blue light[107]
Lens thickness	Increases[108]
Vitreous liquefaction	Increases[109]
RPE lipofuscin	Cell loss and lipofuscin accumulation and result in AMD[110]
Recovery of photo pigments	Disc renewal becomes slightly slower with age [111,112]

Chapter 4. Multi-layer ORGs in the human outer retina

4.1 Introduction

Light stimulation of the retina triggers not only the well-known electrical impulses that initiate vision but also a cascade of subtle optical and mechanical changes within retinal tissue[113]. Photoreceptors, the primary light-sensitive neurons, undergo nanometer-scale deformations and refractive index shifts as they transduce photons into neural signals[114]. These light-evoked changes propagate through the complex retinal architecture[115], spanning from the photoreceptor outer segments (OS) to the retinal pigment epithelium (RPE) and adjacent structures, reflecting key aspects of phototransduction[116] and neuroglial interactions[117]. Capturing these minute biomechanical and optical responses provides direct insight into retinal function at the cellular level. By complementing traditional measures of visual function, such imaging deepens our understanding of how light is converted into neural activity, underscoring the expanding role of functional imaging in vision science.

From the introduction of chapter 2, we already know that there are a bunch of advances in optical imaging that have enabled direct visualization of these light-evoked intrinsic responses through a technique using ORG [56,60,62,118-123]. Building upon OCT – which provides high-resolution, depth-resolved images of retinal structure [124] – ORG extends OCT into the functional domain by capturing transient changes in optical path length (ΔOPL) that occur immediately after photo-stimulation. In essence, ORG is a noninvasive functional extension of OCT that records the living response of retinal tissues rather than a static snapshot. By leveraging phase-resolved OCT, ORG

can detect displacements in the order of nanometers, distinguishing individual layer responses with exquisite spatial and temporal resolution [59]. This capability allows functional readouts at the level of single cells or specific retinal layers, far surpassing the spatial localization of conventional electroretinography (ERG)[125]. Unlike standard structural imaging such as OCT or fundus autofluorescence (FAF)[126], which highlights only anatomical abnormalities, ORG objectively measures light-induced neural activity in vivo. It thereby offers a powerful complement to electrophysiological tests (such as the ERG), but with non-contact, much finer resolution and without requiring subjective input from the patient. Such attributes position ORG as an emerging high-impact tool for probing retinal function with the precision of OCT.

Despite its promise, interpreting ORG signals remains challenging because the recorded responses represent a complex interplay of concurrent motions at multiple retinal layers, each potentially differing in amplitude, direction, and timing. The precise direction and magnitude of these layer-specific displacements, such as movements of the photoreceptor ISOS and COST, remain active areas of investigation. Similarly, deeper retinal structures like the ELM and RPE have generally shown minimal or subtle motion, but their exact responses are still being explored. Notably, in the near-foveal region (< 1.5°), preliminary evidence suggests possible relative displacements between the ELM and RPE layers, raising the question of whether this reflects elongation or other structural rearrangements. This multi-layered analysis framework promises to provide a detailed representation of retinal biomechanics, enabling a deeper understanding of phototransduction-related structural changes and potentially uncovering previously undocumented aspects of human retinal physiology.

In this chapter, we discuss the ORG signals arising from distinct pairs of retinal layers, their corresponding movements, and the overall characterization of these responses. While ORG has

significant potential as an objective and non-invasive biomarker of retinal function, interpreting its complex signals remains challenging because the measured responses represent a superposition of concurrent motions across multiple retinal interfaces. Each retinal layer may exhibit unique amplitude, directional, and temporal characteristics, all of which are actively under investigation. The precise displacements of key retinal boundaries between ELM to RPE remain critical to fully understanding retinal biomechanics. Preliminary observations suggest that responses at different retinal depths may reflect distinct physiological phenomena, including photoreceptor elongation, osmotic swelling, or structural rearrangements triggered by phototransduction. By exploring these multi-layer interactions systematically, this chapter aims to clarify the biomechanical basis of ORG signals, identify layer-specific characteristics, and provide insights into retinal physiology and photoreceptor dynamics not previously documented in the human retina.

4.2 Method

4.2.1 Study participants

Ten healthy subjects (ages 20–40), with no known history of retinal disease, and six patients clinically diagnosed with RP were recruited for this study. All participants underwent pharmacological dilation and cycloplegia (using 1% tropicamide ophthalmic solution, Akorn Inc.) prior to image acquisition to ensure optimal imaging quality. The research procedures adhered to the tenets of the Declaration of Helsinki, and informed consent was obtained from all participants. The study protocol was reviewed and approved by the Institutional Review Board of the University of Washington (IRB#STUDY00002923).

4.2.2 ORG imaging systems with AO/non-AO modes

In this study, two different ORG acquisitions systems were used:

1) Adaptive Optics OCT (AO-OCT): This system incorporates an adaptive optics (AO) module into a custom-built, line-scan spectral-domain OCT platform. This AO-OCT configuration enables single-cell-level imaging and facilitates investigations such as cone classification—differentiating long (L), medium (M), and short (S) wavelength cones—at a stimulus wavelength centered at 660 ± 10 nm. The field of view (FOV) in each region of interest (ROI) is limited to approximately 1.5° × 1.5°, allowing high-resolution focus on discrete retinal features. A more detailed description of the AO-OCT design, including optical setup and system calibration, has been published previously [63].
2) Coarse-scale ORG (CoORG): To overcome practical challenges observed in some patients (e.g., unstable fixation, small pupil size, or advanced retinal pathology) and to accommodate a wider field of view (FOV), the second OCT system operates without the AO module. This CoORG system offers a 3° × 5.5° FOV and uses a 532 nm ± 5 nm stimulus, making it more suitable for a broader range of normal subjects and many clinical populations such as those with RP. The nominal photon density is 14.4×10^6 photons/μm^2 based on a model eye of 24 mm axial length while 7 mm pupil diameter. The technical details of this system, including scanning protocols and reconstruction algorithms, have been described previously in chapter 2.6 and in ref[85].

4.2.3 Protocol and analysis

For all participants, a one-minute dark adaptation was conducted prior to data acquisition. In the CoORG system, 50 OCT volumes were recorded sequentially at a volume rate of 32 Hz, with each volume reconstructed using fast Fourier transform (FFT). This extended FOV accommodates eyes where AO-based imaging might be challenging. In the AO-OCT system, which operates at a volume rate of 20 Hz, participants also underwent a one-minute dark adaptation before recording

50 OCT volumes. These AO-OCT data were processed similar to CoORG data. After initial assessment to discard volumes with blinking artifacts or poor fixation, the retained datasets from both systems were aligned and averaged to enhance signal-to-noise ratio (SNR). Subsequent analyses included identifying and classifying cone types in the AO-OCT volumes and examining broader-scale retinal structure using CoORG, with additional image-processing steps (e.g., layer segmentation, strip-based segmentation) applied as appropriate for each investigation.

4.3 Results

4.3.1 The categories of ORGs among different outer retinal layers

The ORG response was then calculated from the phase change between two distinct retinal layers, converted to an optical path length change (ΔOPL) using the formula (1.3). Figure 4.1(A) shows a typical B-scan from the CoORG system, highlighting the four outer retinal layers with greater reflectance, the external limiting membrane (ELM), inner/outer segment junction (ISOS), cone outer segment tips (COST), and retinal pigment epithelium (RPE).

Based on these distinct layers, we define a series of ORG responses derived from selected pairs of them: α ORG (ISOS–COST), β ORG (COST–RPE, subretinal space), γ ORG (ISOS–RPE), ε ORG (ELM–ISOS), and δ ORG (ELM–RPE), as depicted in Figure 4.1(B). Representative time traces of these signals (Figure 4.1(C)) demonstrate that α ORG and β ORG typically exhibit larger amplitudes, while γ ORG shows a relative small amount changes, and ε ORG as well as δ ORG are also relatively small. Among these five signals, we can find that the amplitude of α, γ, and δ ORGs are positive (elongation), whereas β and ε ORGs' amplitudes are negative (contraction). In the single-flash stimulus paradigm shown in Figure 4.1(C), the ΔOPL undergoes an immediate, low-amplitude reduction after stimulus onset, followed by a sharp rise to a plateau. The saturated

ORG response is calculated as the average ΔOPL over approximately 300 ms during this plateau, and it can be further analyzed across different eccentricities to quantify spatial variations in the outer retina.

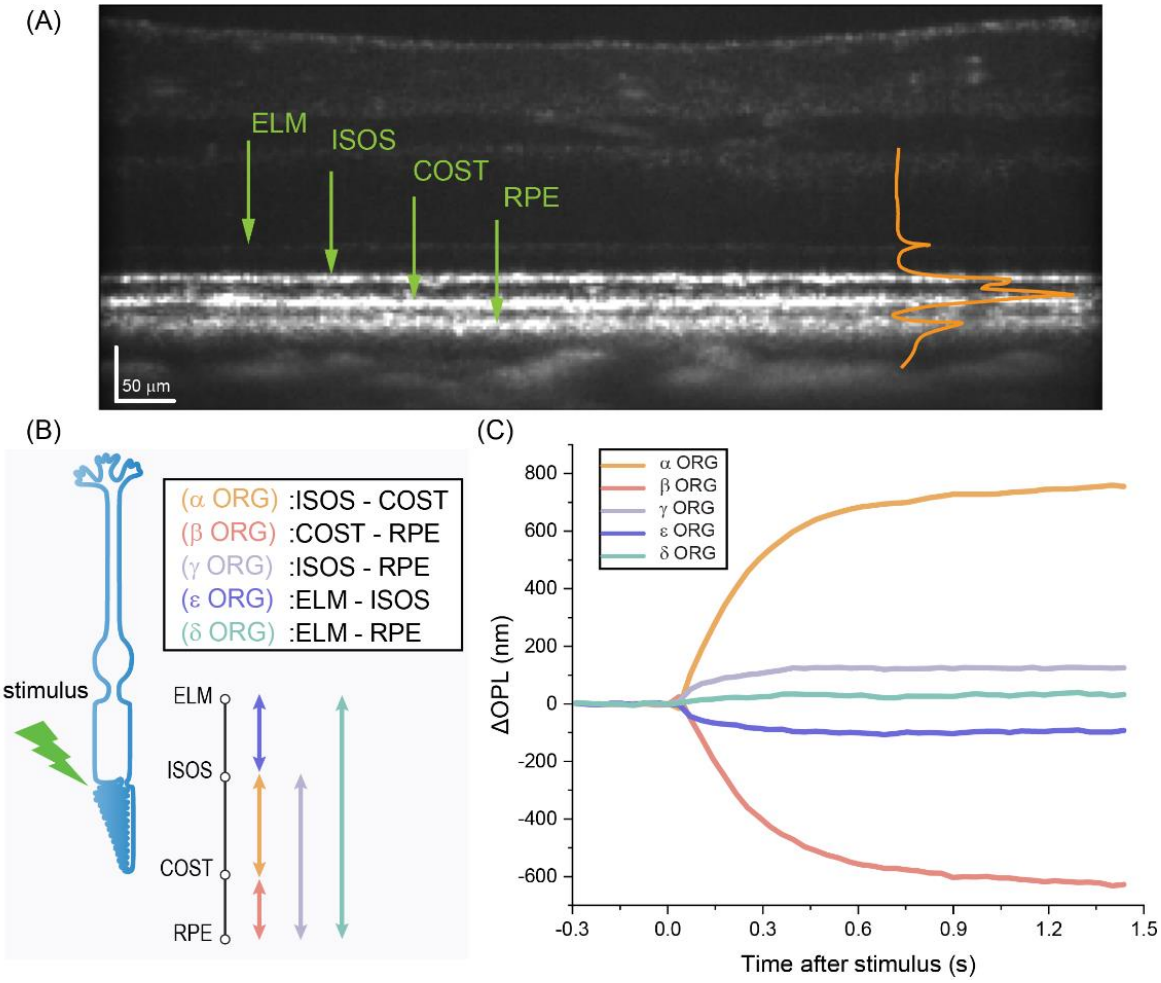


Figure 4.1 Schematic representation of different ORG responses. (A) shows an example B-scan from the CoORG system with the outer retinal layers: external limiting membrane (ELM), inner segment/outer segment junction (ISOS), cone outer segment tips (COST), and retinal pigment epithelium (RPE) marked by green arrows, alongside the average A-line profile on the right. (B) illustrates the various ORG responses derived from differences between specific retinal layers: α ORG (ISOS–COST), β ORG (COST–RPE), γ ORG (ISOS–RPE), ε ORG (ELM–ISOS), and δ ORG

(ELM–RPE). (C) presents representative ORG traces over time, highlighting how these signals evolve within each corresponding layer boundary.

4.3.2 ORGs across eccentricities

From the ISOS *en face* image in Figure 4.2(A), we extracted the saturated ORG responses at eccentricities ranging from 0.25° to 5°, using 0.5° × 0.5° regions of interest (ROIs). The resulting plot in Figure 4.2(B) shows that most absolute ORG amplitudes decrease with increasing eccentricity. Focusing first on α, β, and γ ORG responses, we find that α + β ORG closely matches γ ORG, indicating that the net elongation between the ISOS and RPE layers (γ ORG) arises from the combined elongations of ISOS–COST (α ORG) and COST–RPE (β ORG). The characteristic rates of change for these individual responses are detailed in Supplementary Information S1, supported that the γ ORG is a combination of α + β ORGs. Additionally, γ ORG increases with decreasing eccentricity, indicating an elongation between the ISOS and RPE is more pronounced near the central fovea. Assuming the RPE remains rigid and static by virtue of its attachment to Bruch's membrane (BrM), this elongation implies a slight upward shift of the ISOS after light stimulation.

Next, exploring the relationship among γ, ε, and δ ORG, we find that γ + ε ORG also closely aligns with δ ORG. This suggests that the elongation between ELM and RPE (δ ORG) effectively reflects the sum of ISOS–RPE (γ ORG) and ELM–ISOS (ε ORG). Interestingly, near the fovea (< 1°), there remains a measurable amplitude for δ ORG (e.g., 80 nm in 0.25°), implying a small elongation between ELM and RPE in this region. For deeper, cellular-scale insights into these signals, higher-resolution imaging via AO-OCT is necessary.

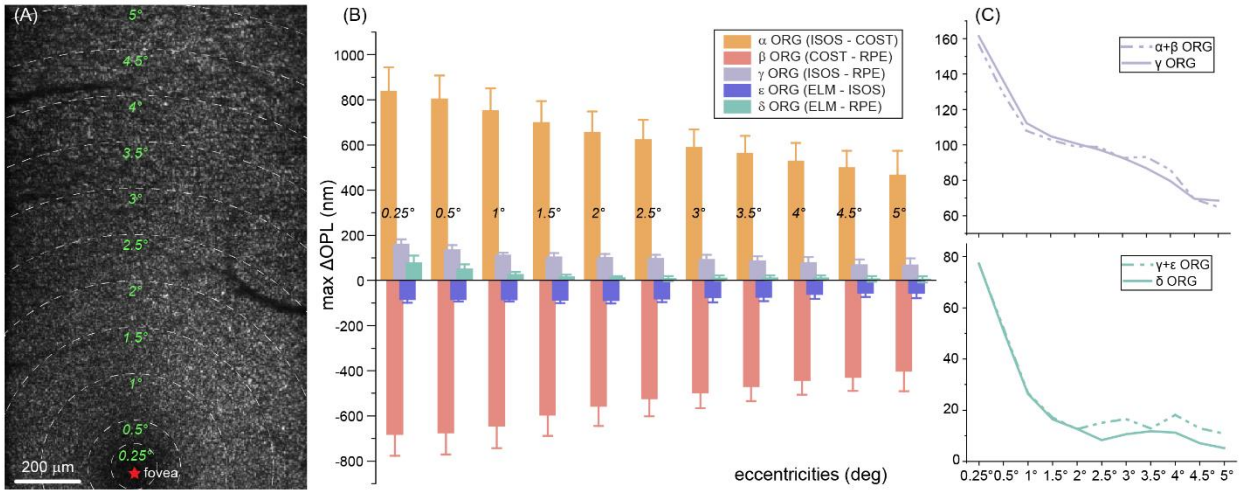


Figure 4.2 (A) ISOS *en face* image extending from the central fovea out to 5° eccentricity. The dashed white circles indicate eccentricities binned at 0.5° intervals. (B) Saturated ORG amplitudes plotted as a function of eccentricity (0.25° to 5°) for α ORG (orange), β ORG (pink), γ ORG (light purple), ε ORG (dark purple), and δ ORG (cyan). (C) Comparison of the sum α ORG + β ORG (purple dash-dot line) with γ ORG (solid purple line), and the sum γ ORG + ε ORG (green dash-dot line) with δ ORG (solid green line), illustrating how these individual layer responses relate to one another.

4.3.3 Kinetics among α, β, and γ ORGs

We measured the rate of change in ΔOPL over time by taking the derivative of each subject's ORG trace and then averaging the results. As shown in the bar plots in Figure 4.3(A), the maximum slope decreases with increasing eccentricity. Meanwhile, Figure 4.3(B) confirms that the γ ORG rate of change effectively equals the sum of α ORG and β ORG.

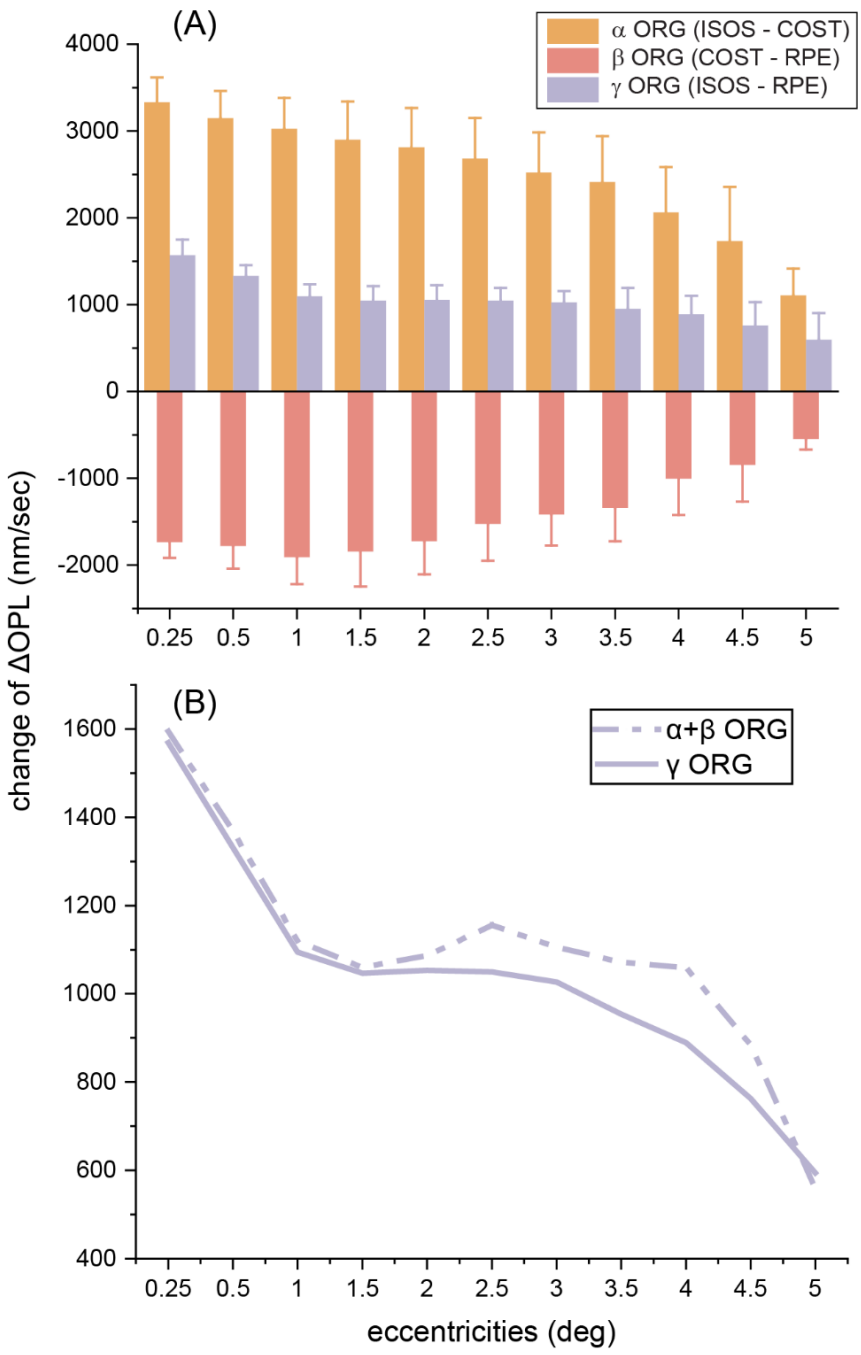


Figure 4.3 The kinetics analysis among α, β, and γ ORGs. (A) The rate of change of the ΔOPL as a function of eccentricity for α ORG (ISOS–COST), β ORG (COST–RPE), and γ ORG (ISOS–RPE). Error bars represent ±1 standard deviation. (B) The purple dash-dot line indicates the sum (α ORG + β ORG), while the solid purple line shows γ ORG, allowing direct comparison of their maximum rates of change.

4.3.4 ELM – RPE response analysis at the cellular scale using AO-ORG

AO-based ORG (AO-ORG) enables single-cell resolution measurements of δ ORG near the fovea. Two ROIs were selected using AO-OCT: one centered at 0.5° temporal (Figure 4.4(B)) and another at 4° nasal (Figure 4.4(C)). The spatial maps reveal not only higher cone density but also greater δ ORG amplitudes at 0.5° compared to 4°. As shown in Figure 4.4(D), the mean saturated δ ORG amplitude in the 0.5° ROI is 77.5 ± 26.7 nm, nearly three times higher than the 26.9 ± 16.1 nm observed at 4°. Interestingly, despite clear distinctions among L, M, and S cones, the δ ORG signals overlap across these cone types (Figure 4.5). This result suggests that the ELM–RPE elongation is a membrane-wide phenomenon relatively independent of individual cone subtype characteristics.

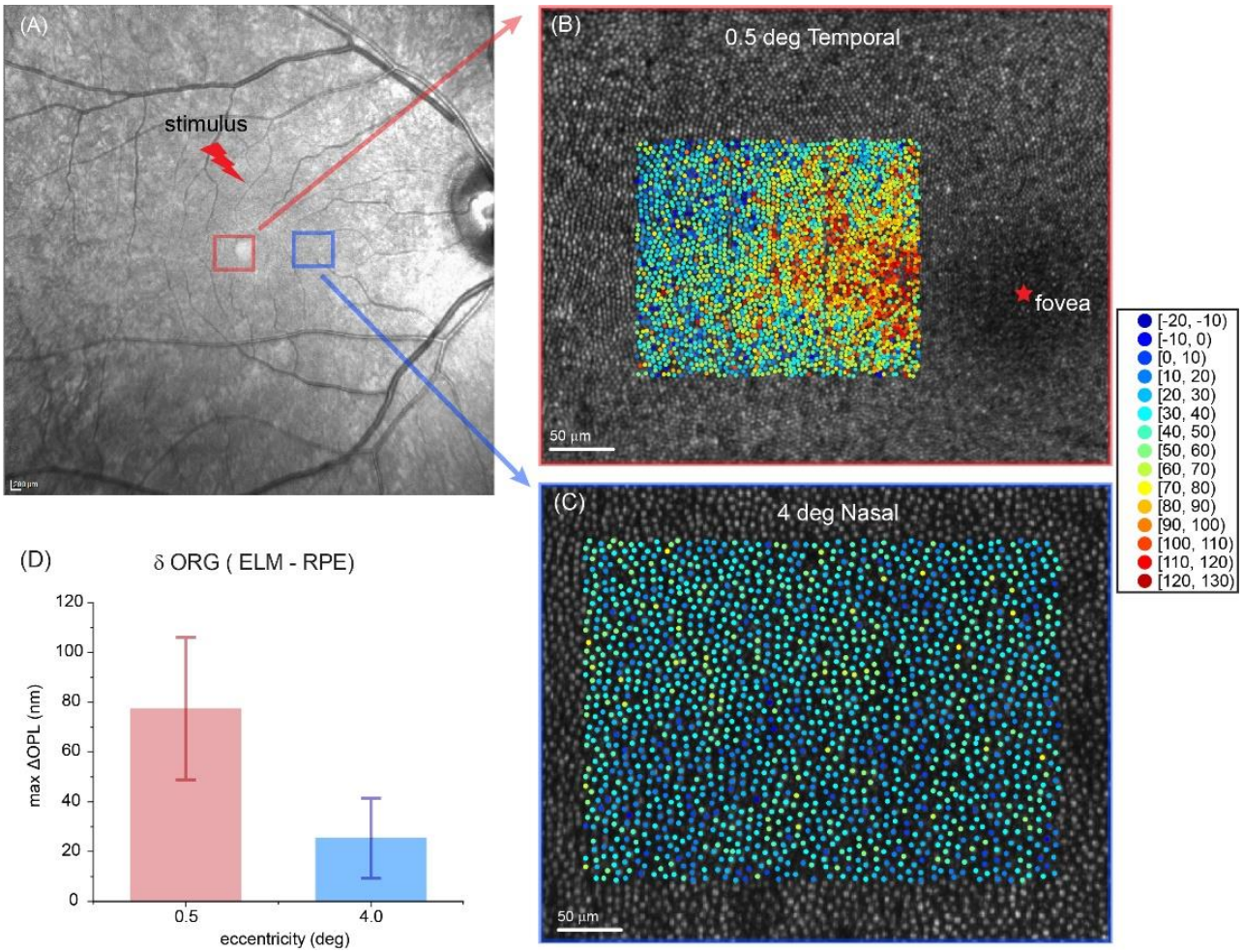


Figure 4.4 Adaptive Optics-based ORG (AO-ORG) near the fovea to assess the residual δ ORG amplitude. (A) En face SLO image from a commercial OCT, where the red and blue rectangles indicate the 0.5° temporal and 4° nasal eccentricities, respectively. (B) and (C) illustrate the spatial distribution of the saturated δ ORG amplitude at single-cone resolution, overlaid on the ISOS/COST MIP en face image for each location. The color scale indicates the saturated ΔOPL at individual cones, with 10 nm increments per bin. (D) A bar plot of the mean δ ORG amplitude compares the two regions, indicating a significant difference between them.

Furthermore, to capture the cellular-scale retinal images, we employed AO-OCT to do a further analysis, shown in Figure 4.5(A). Because the 660 ± 10 nm stimulus differentially affects the three cone types (L, M, and S), we classified each cone to visualize the mosaic (Figure 4.5(B)). The averaged α ORG traces for these cone clusters (Figure 4.5(C1)) show clear distinctions among the three types, which is further supported by the bar plots in Figure 4.5(C2). In contrast, when measuring the ORG response between the ELM and RPE (δ ORG), all three cone types exhibit similar responses with no significant differences (Figure 4.5(D1–D2)). From preivous studies, the ELM is a continuous adherent layer between the inner segments and the overlying Müller glia cells[69]. Rather than allowing each photoreceptor to move independently, the ELM acts as a unified, elastic membrane that maintains the alignment of local photoreceptor clusters. This means any axial movement (here it is elongation) of photoreceptor outer segments tends to occur in concert for a local group of cells, constrained by the ELM's continuous junctional net[127], effectively shifting the ELM–RPE distance as a single structural unit. Moreover, previous studies indicate that in primates, the ELM–Müller glia region near the fovea is roughly five times denser than in surrounding areas[128], providing additional capacity for ELM layer's upward displacement and explaining the residual elongation observed between the ELM and RPE in the near-foveal region.

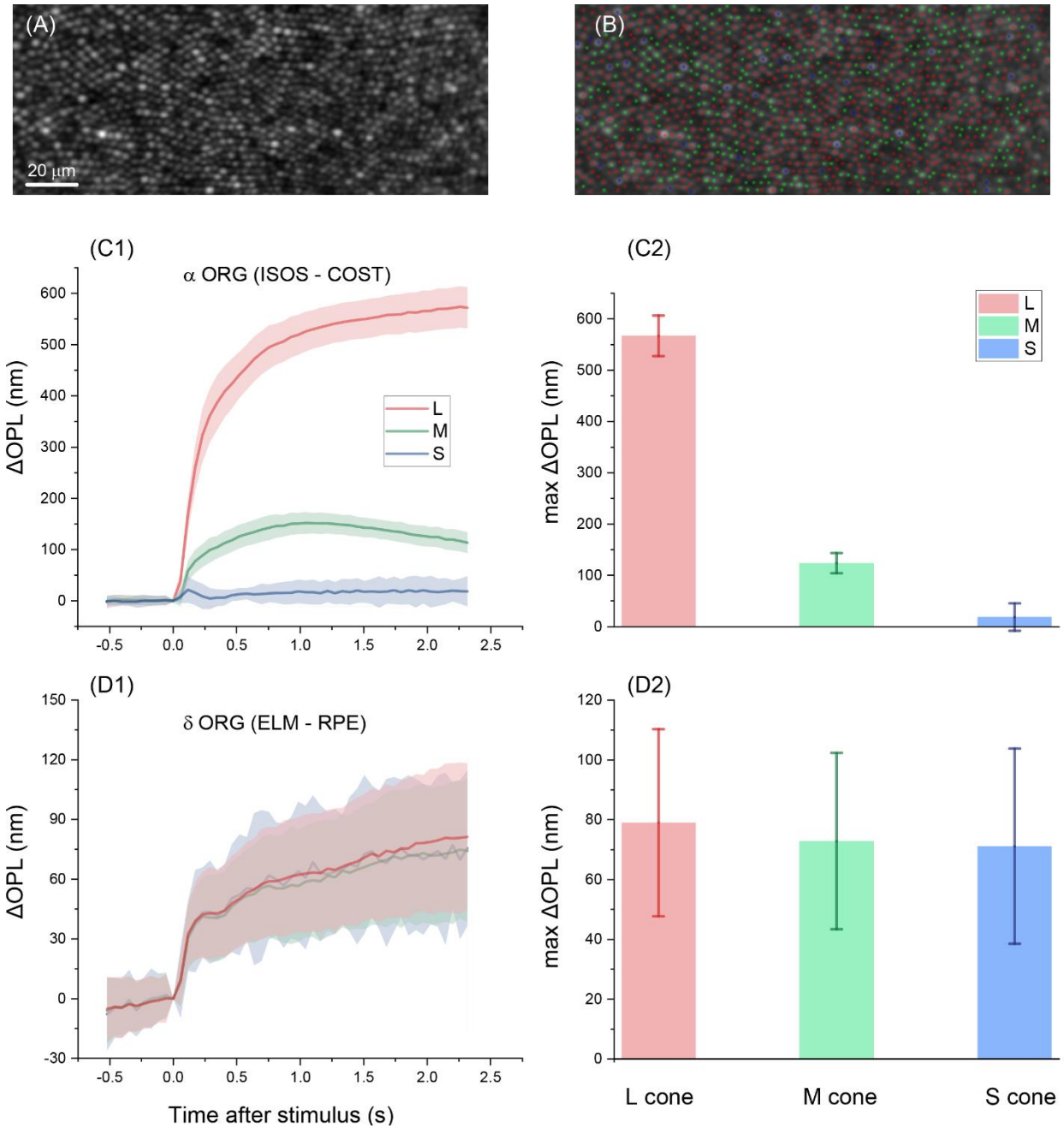


Figure 4.5 AO-based ORG with cone classification, featuring (A) a maximum intensity projection (MIP) of the ISOS/COST interface in a selected region of interest (ROI) and (B) the corresponding cone mosaic and distribution. In (C1), time-resolved α ORG traces are shown for L-, M-, and S-

cones, with shaded regions indicating ±1 standard deviation, while (C2) presents the corresponding saturated α ORG amplitudes by cone type. Panels (D1) and (D2) illustrate the time-resolved δ ORG traces and their associated amplitude bar plots, respectively.

The outer retina exhibits distinct mechanical movements in response to light, which vary between the near fovea and the periphery. As shown in Figure 4.2(B), absolute ORG amplitudes generally decrease with increasing eccentricity across all measured layers; however, a residual δ ORG remains detectable near the fovea (i.e., within ~1°) according to Figure 4.2(C) (bottom) and Figure 4.4(B–D). A representative B-scan of these amplitude changes (elongation or contraction) is depicted in Figure 4.7(A). The retinal pigment epithelium (RPE) is considered relatively rigid and tightly coupled to Bruch's membrane, whereas the external limiting membrane (ELM) is more flexible, lying adjacent to the neural retina (Müller cells). Figure 4.6 indicates that the RPE–BrM complex remains stable, showing only blood vessel–induced pulsations unrelated to light stimulation or eccentricity, thus the RPE can be treated as effectively immobile.

4.3.5 Evidence for absolute movement direction between ELM/RPE layers

To elucidate the residual positive δ ORG near the fovea, which indicates net elongation between the ELM and RPE, we focused on the apical RPE visible in our data. Although the boundary with BrM is indistinguishable, a previous report indicates the combined RPE–BrM thickness is approximately 26.3 ± 4.8 μm[129]. Given our axial pixel resolution of 3.15 μm/pixel in CoORG system, we selected BrM 5 pixels below the apical RPE (Figure 4.6(A)) and measured their relative displacements. As shown in Figure 4.6(B), δ ORG traces differ across eccentricities, with near-foveal regions displaying a stronger response to light stimulus. When examining the ELM–BrM response (Figure 4.6(C)), the overall trend persists but includes a periodic fluctuation. In contrast, RPE–BrM measurements (Figure 4.6(D)) exhibit a clearly periodic pulsation not triggered by the

stimulus. To confirm this, we conducted a non-stimulus control (Figure 4.6(E))—where the timeline is labeled ‘time after ref-vol’, revealing a similar periodicity that does not vary with eccentricity or stimulus onset. This pulsation is most likely driven by blood-vessel dynamics[130]. Consequently, the near-identical motion of RPE and BrM suggests that light-evoked deformation of the RPE–BrM complex is not differentiable, and their relative position keeps stationary.

Building on our earlier discussion that the ELM behaves as a more flexible structure, and given the demonstrated stability of the RPE–BrM complex, we suggest that the net elongation between the ELM and RPE arises from the ELM shifting upward, driven by photoreceptor swelling and the ELM’s intrinsic properties.

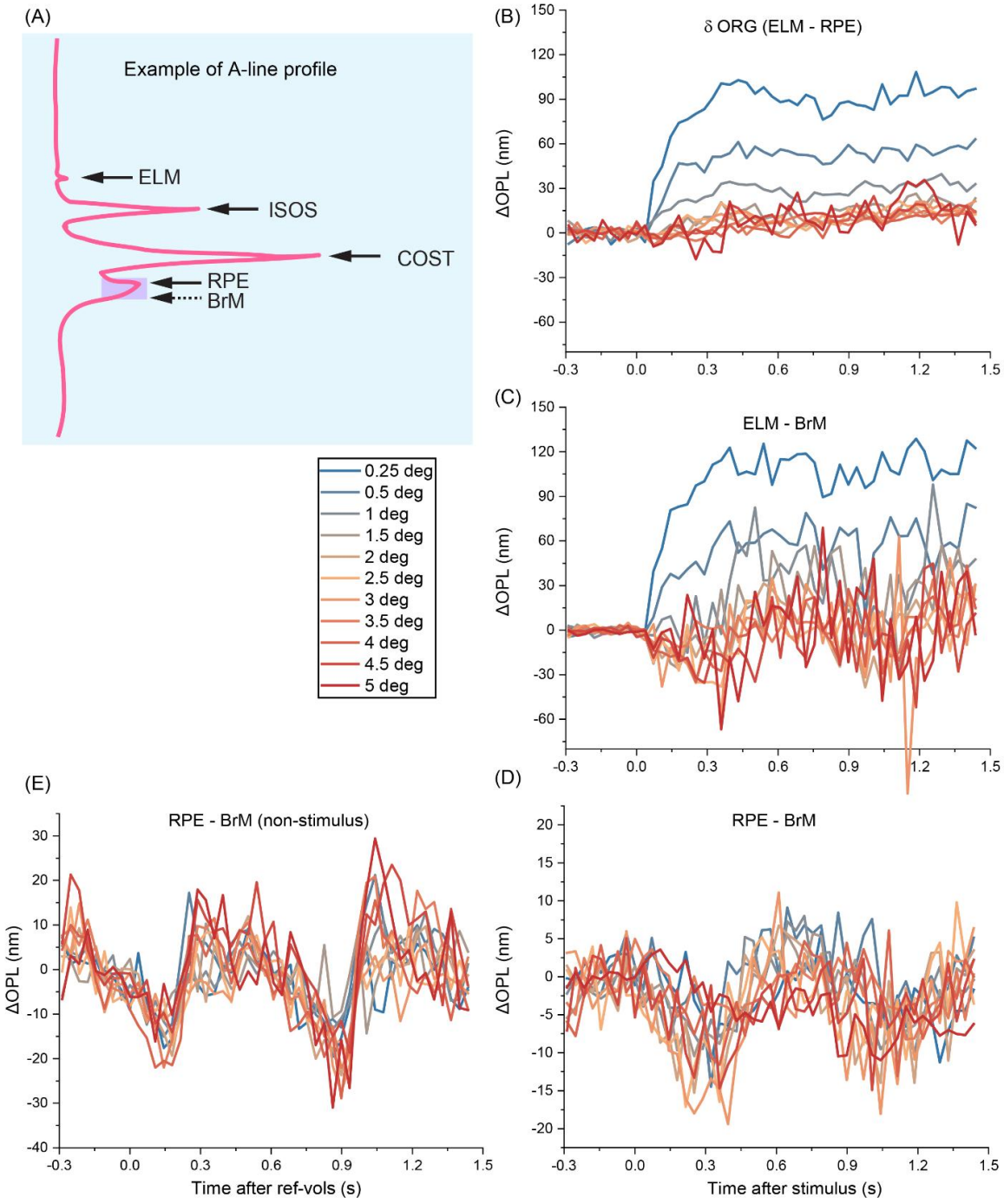


Figure 4.6 An auxiliary demonstration of RPE movement. (A) An exemplary A-line profile, where the dashed arrow indicates the BrM layer within the indistinguishable RPE–BrM complex. (B) Time-resolved δ ORG traces across eccentricities ranging from 0.25° to 5° for a typical single subject. (C) and (D) show the ORG responses for ELM–BrM and RPE–BrM, respectively, as a

function of eccentricity. For comparison, (E) presents a non-stimulus RPE–BrM response, with a consistent legend applied to all four panels.

Based on these observations, the outer retina can be divided into two behavioral regions:

Peripheral to the foveal slope (> 1.5°), both ELM and RPE remain relatively stable (Figure 4.7(B)), the COST layer undergoes substantial downward elongation, and the ISOS exhibits a smaller upward displacement (with the COST movement amplitude ~5–7 times greater than that of the ISOS).

Near the fovea (≤ 1.5°), ISOS and COST maintain their respective upward and downward motion, RPE remains stable, yet the ELM shifts noticeably toward the inner retina (Figure 4.7(C)). Consequently, when considering ELM–RPE as a reference complex, the ELM appears to move upward in the foveal region.

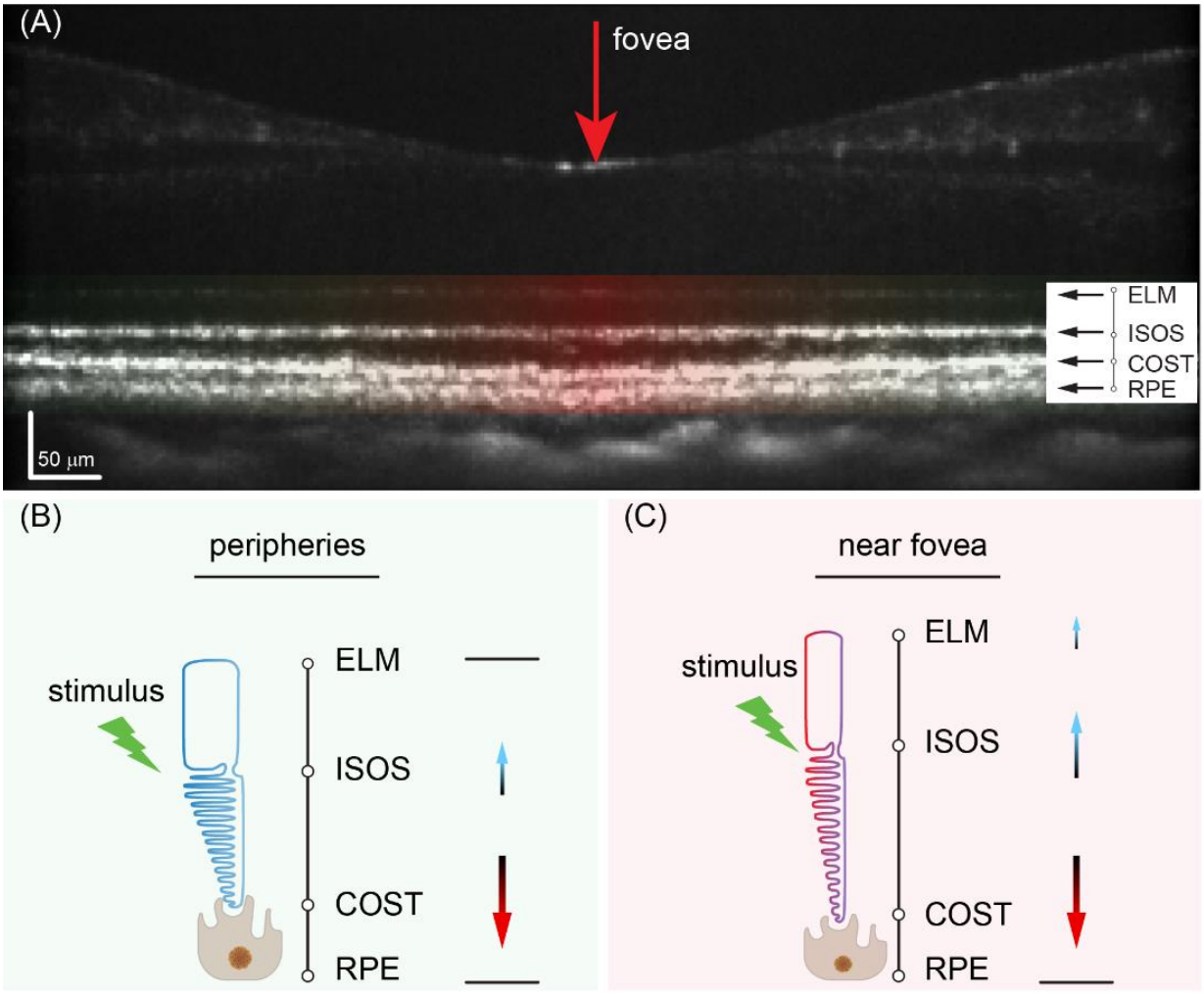


Figure 4.7 Mechanical movement of distinct retinal layers after light-evoked activity. (A) A color-coded amplitude map overlaid on a representative OCT B-scan, illustrating how the movement amplitude transitions from central fovea (red- larger movement) to peripheries (green- smaller movement). In peripheral regions, the ELM and RPE remain relatively stable with minimal displacement. However, within approximately 1.5° of the fovea, there is a pronounced elongation between the ELM and RPE, while the COST displaces downward substantially, and the ISOS shifts upward more mildly. (B) & (C) Plots depicting these displacements in more detail, confirming that the near-foveal region exhibits significantly greater mechanical movement than the retinal periphery, particularly in ELM layer.

4.3.6 Modeling the ELM displacement near the fovea

In the previous section, we observed that the ELM moves up in foveal regions. Here, we propose a viscoelastic model to explain the mechanism underlying this movement. A net upward displacement of the ELM suggests that there is an elongation in cone photoreceptor (outer segment [OS] + inner segment [IS]). Below, I derive a quantitative framework demonstrating how three factors—(i) the axial force generated within the OS, (ii) the IS geometry (diameter and length), and (iii) the material stiffness of the IS (primarily determined by mitochondrial packing)—collectively determine this displacement.

Based on Figure 3.9 and Eq 3.1, we know that the saturated ΔOPL is proportional to a bleaching constant for a given OS length. Similarly, for a fixed bleaching level, the saturated ΔOPL is proportional to the change in OS length. Since the saturated ΔOPL arises from the force generated by phototransduction, we can represent the force from the OS with a proportionality constant $\boldsymbol{c}$ as follows:

$$F \propto \Delta OPL = \boldsymbol{c} \cdot OSL \tag{4.1}$$

Meanwhile, the axial stiffness (k) of the IS in the fovea can be approximated by considering it as an elastic rod, represented by the standard stiffness equation:

$$k = E \cdot \frac{A_{IS}}{ISL} \tag{4.2}$$

Where $\boldsymbol{E}$ is Young's modulus of the IS material (primarily influenced by mitochondrial density), $\boldsymbol{A}$ is the cross-sectional area, and $\boldsymbol{ISL}$ is the IS length. This simplified expression allows us to quantify how IS geometry and material properties affect its resistance to axial deformation. However, it should be noted that the cone IS is geometrically a tapered frustum, with its diameter

gradually decreasing from the apical region (near the myoid) toward the narrower distal tip (ellipsoid zone) in the periphery. By contrast, near the fovea, the apical and distal diameters of the IS are nearly identical [131]. To effectively represent these structural characteristics, we use the mean value of the apical and distal IS diameters as the representative diameter parameter. The specific structural parameters used for both foveal and peripheral regions are summarized in Table 4.1.

Table 4.1 The parameters of cone structures between fovea and periphery

Eccentricity	ISD* (μm)	ISL (μm)	OSL (μm)	Measured ΔOPL (nm)
Fovea (0.25 °)	2.7	30	28	128
Periphery (4 °)	6.5	25	19	12

*The inner segment diameter (ISD) values used in this analysis were obtained from previously published data[132].

Thus, the equilibrium displacement (x_∞) of the ELM can be estimated by combining anatomical parameters with experimentally measured modulus values:

$$x_\infty = \frac{F}{k} = \frac{OSL}{E} \cdot \frac{ISD}{A_{IS}} \tag{4.3}$$

Considering mitochondrial distribution, mitochondria in the fovea are generally denser compared to the periphery and are present in the myoid zone as well as in the outer fiber proximal to the ELM[133]. Based on previously reported atomic force microscopy measurement[134], we calculated

that the Young's modulus in the fovea (E_{fovea}) is slightly higher than in the periphery (E_{periph}), given the difference between mitochondrial and cytoplasmic stiffness. By combining mitochondrial distributions and stiffness values, we estimated the relative modulus ratio as $E_{fovea}/E_{periph} = 1.01$.

Combining these factors, the equilibrium displacement ratio between fovea and periphery can be expressed approximately as:

$$\frac{x_{\infty,fovea}}{x_{\infty,periph}} \approx \frac{OSL_{fovea}}{OSL_{periph}} \cdot \frac{ISL_{fovea} \cdot A_{IS,periph}}{A_{IS,fovea} \cdot ISL_{periph}} \cdot \frac{E_{periph}}{E_{fovea}} = 10.14 \approx 10 \quad (4.4)$$

This indicates that the interplay of OS-generated force, IS structural geometry, and IS material stiffness collectively results in a net elongation of the ELM near the fovea, which closely matches our measured results (Table 4.1). Thus, the residual upward displacement of the ELM after stimulation can be fully explained by the force-compliance balance described in equations (4.1–4.4):

1. Force originates in the OS, with the longer OS in the fovea generating a larger axial force $\boldsymbol{F}$.
2. Compliance is determined primarily by IS geometry, with foveal cones approximately five times more compliant than peripheral cones.
3. Young's modulus, while being influenced by mitochondrial density, varies only minimally between fovea and periphery (1% difference).

4.3.7 Comprehensive characterization of γORG (ISOS - RPE)

Given the different ORG representations from Figure 4.1(C) & Figure 4.2(B), the COST layer-related ORG types - α & β ORG - show a relatively high amplitude compared to other layers because the cone outer segment's uniquely flexible, continuously stacked disc structure—coupled

with its soft attachment to the RPE, facilitates pronounced osmotic and biochemical-driven elongation during the slow phase of phototransduction. When isolating the contribution of the COST layer, γ ORG exhibits a relatively high amplitude compared to ε and δ ORG, suggesting its potential utility in assessing inherited retinal dystrophies (IRDs) where COST reflectivity may be compromised. However, before γ ORG can be adopted in clinical practice, establishing normative data from healthy controls is essential. Therefore, to characterize γ ORG more comprehensively, we examined its eccentricity dependence, stimulus-intensity related changes, and structure–function relationships within our control population. As shown in Figure 4.8(A), the γ ORG response diminishes with increasing eccentricity, consistent with previous findings [85]. A box-and-whisker plot of the saturated γ ORG amplitudes across 10 control subjects in Figure 4.8(B) further supports this eccentricity-dependent decline; corresponding α ORG data can be found in Figure 4.9(A, B).

We next investigated the impact of stimulus intensity by fixing the eccentricity at 5° temporal and varying the photon density from 1.73×10^6 to 15.6×10^6 photons/μm^2. The resulting ORG traces show a clear positive correlation with light level, and the saturated γ ORG amplitudes display a linear increase with photon density (Figure 4.8D), mirroring the α ORG findings in Figure 4.9(C, D). Lastly, we observed a significant structure–function correlation between outer retinal thickness (ORT, defined here as the thickness from ISOS to RPE) and the saturated γ ORG amplitude (Figure 4.8E). The linear fit ($p < 0.001$) indicates that changes in ORT account for approximately 66% of the variation in γ ORG amplitude. A similar trend appears in Figure 4.9(E), although the structure–function slope for outer segment length versus saturated ΔOPL is approximately four times higher than that for γ ORG.

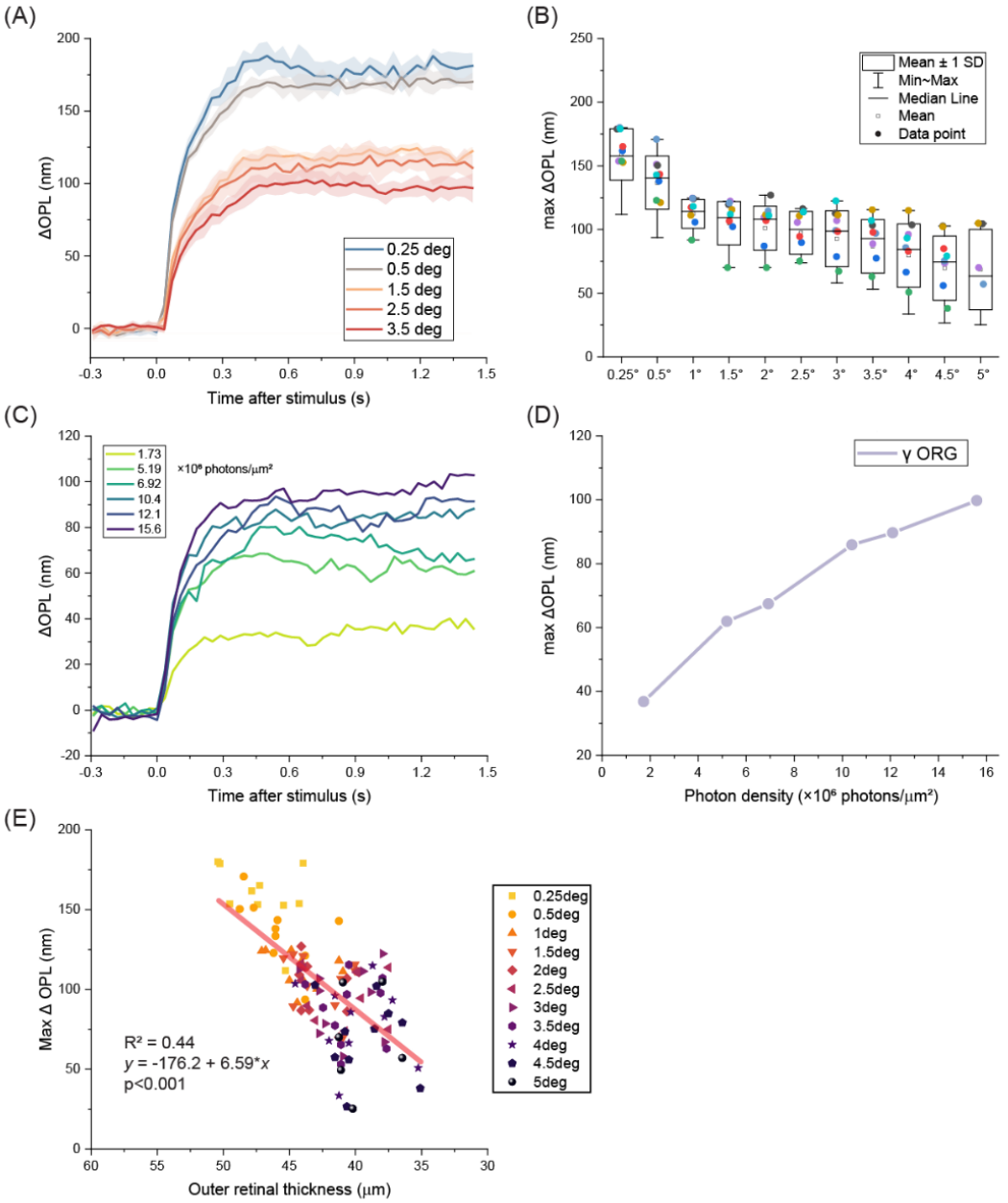


Figure 4.8 Comprehensive characterization of the γ ORG, showing repeatability, stimulus sensitivity, eccentricity dependence, and structure–function relationships. (A) presents representative γ ORG traces recorded at eccentricities ranging from 0.25° to 3.5°, while (B) shows box-and-whisker plots of γ ORG amplitudes from 10 subjects across 0.25° to 5°. In (C), γ ORG traces acquired at varying photon densities, measured at 5° temporal eccentricity, illustrate stimulus-dependent responses, and the corresponding relationship between saturated γ ORG amplitude and photon density is plotted in

(D). Finally, (E) displays the structure–function correlation between saturated γ ORG amplitude and outer retinal thickness (ORT), with a linear fit shown in red.

4.3.8 Comprehensive characterization of αORG (ISOS – COST)

The overall characteristics of α ORG in this study are consistent with our earlier findings[85], as illustrated by the eccentricity-dependent traces and box-and-whisker plots in Figure 4.9(A–B). The light-sensitivity pattern in Figure 4.9(C–D) likewise aligns with previous results[56]. Moreover, at a nominal photon density of 14.4×10^6 photons/μm², the structure-function (S–F) slope shown in Figure 4.9(E) closely matches our earlier observations, indicating that higher photon densities yield steeper S–F slopes[85].

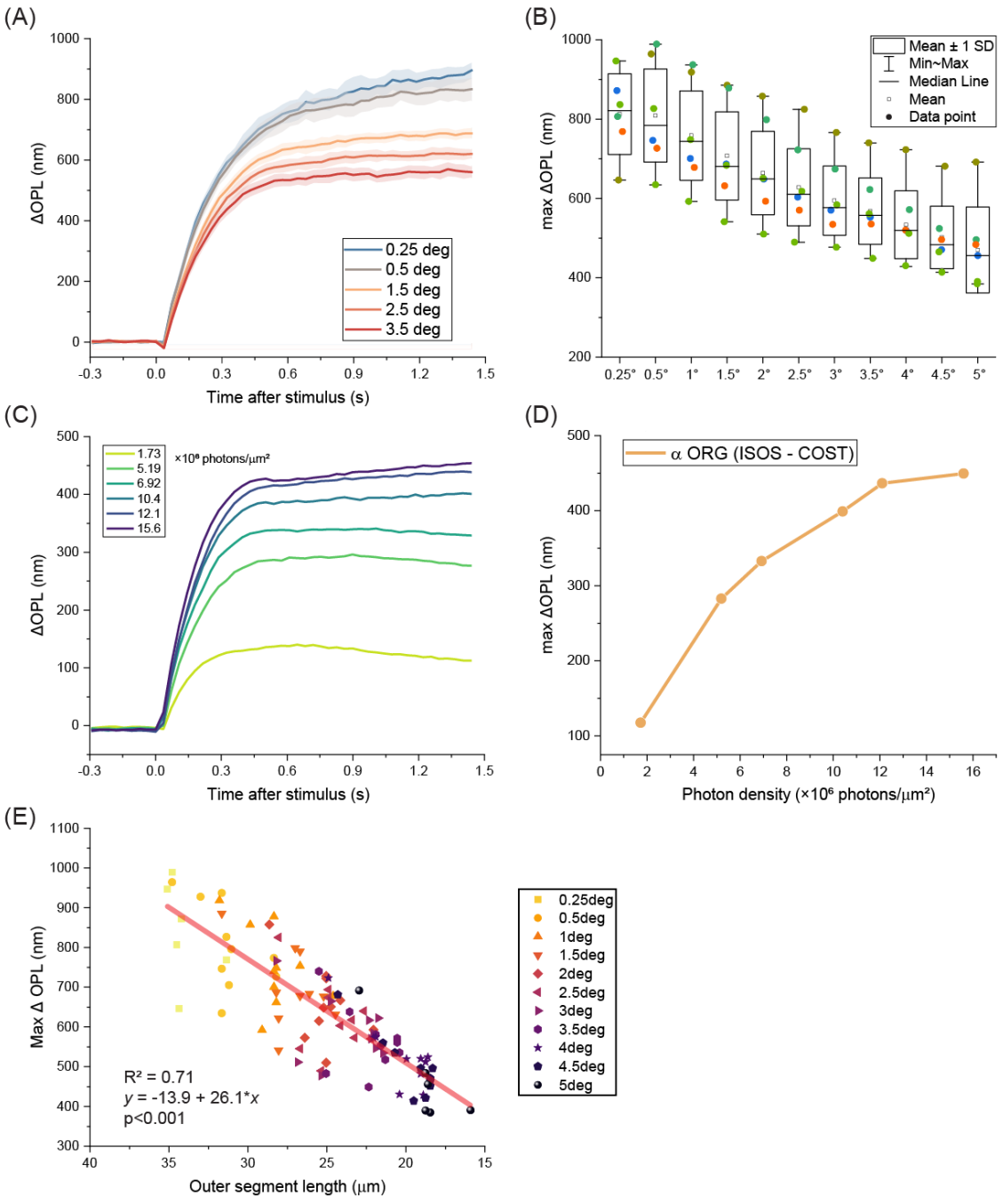


Figure 4.9 Corresponding cone (α, ISOS - COST) ORG characterizations. Comprehensive characterization of the α ORG, showing repeatability, stimulus sensitivity, eccentricity dependence, and structure–function relationships. (A) presents representative α ORG traces recorded at eccentricities ranging from 0.25° to 3.5°, while (B) shows box-and-whisker plots of α ORG amplitudes from 10 subjects across 0.25° to 5°. In (C), α ORG traces acquired at varying photon

densities, measured at 5° temporal eccentricity, illustrate stimulus-dependent responses, and the corresponding relationship between saturated α ORG amplitude and photon density is plotted in (D). Finally, (E) displays the structure–function correlation between saturated γ ORG amplitude and outer segment length, with a linear fit shown in red.

4.4 Discussion

ORG represents a promising, noninvasive, and label-free functional imaging modality for assessing the light-evoked activity in the retina. By targeting various inter- and intra-layer interfaces—ranging from the ISOS and COST to the ELM and RPE —ORG provides a comprehensive evaluation of outer retinal function. Different ORG metrics, including α, β, γ, and δ ORG, capture distinct structural changes during phototransduction, enabling refined assessments of retinal function and health. In detail, α-ORG (ISOS-COST) shows a rapid elongation, β-ORG (COST-RPE), by contrast, exhibits a strong negative shift, suggesting that the interface between cone outer segments and the RPE experiences a contraction. γ-ORG (ISOS-RPE), which is often a more moderate but observed response, reflects broader osmotic changes occurring between the inner/outer segment junction and the RPE, likely linked to swelling or elongation of the outer segments. The ε-ORG (ELM-ISOS) and δ-ORG (ELM-RPE) components display smaller magnitude responses but are crucial for capturing deformations in deeper retinal structures, particularly in how the ELM interacts with photoreceptor dynamics.

In this study, we observed that light stimulation elicits a net elongation spanning from ISOS to RPE, even when accounting for the cone outer segment and subretinal space as a single unit. Specifically, the COST interface shows a pronounced downward shift following light stimulus, whereas the ISOS undergoes a slight but measurable upward displacement. These observations

suggest that, despite the dominant COST movement, additional subtle alterations in photoreceptor substructures contribute to the net expansion of the OS.

Our measurements also revealed that the ELM and RPE remain largely stable over a few seconds, as indicated by minimal or negligible changes in ORG amplitude. However, near the central fovea (<1.5° eccentricity) in Fig. 4.7(C), an unexpected elongation was detected between ELM and RPE. Individual cone classification using AO-OCT indicated that despite cones being classified as L-, M-, or S-cones, there is no clear decoupling at the ELM-RPE complex. This finding supports the notion that the ELM acts as a unified boundary, tightly linked to Müller glia and photoreceptor inner segments [135]; consequently, when multiple adjacent cones elongate, the entire ELM may shift slightly as a single structural entity.

Additional evidence from RPE–BrM analyses (Figure 4.6) indicates that the RPE–BrM complex remains relative stable. Previous studies have established BrM as a rigid "wall" anchored to the choroid, making significant movement unlikely and further supporting the stability of the RPE layer. Thus, the net elongation in the foveal region is most likely attributed to the ELM's small upward displacement (~100 nm), driven by photoreceptor and subretinal expansions. Prominently, these transient changes occur on a timescale of seconds, distinct from previous reports of micron-scale shifts over tens of minutes suggesting an alternative underlying mechanism, possibly involving transient water movement or rapid photoreceptor deformation.

From a clinical standpoint, the broader suite of ORG measurements demonstrates significant potential. For example, γ-ORG can be particularly beneficial when conventional COST-based metrics (e.g., CoORG imaging) fail, such as in regions of diseased retina where the COST layer reflectivity is compromised. However, an invisible COST reflection does not necessarily indicate a loss of light perception, as it may arise from factors such as abnormal waveguiding [59]. Employing

γ-ORG can provide more insight into disease status under such cases. Indeed, our exploration in RP indicates that retinal functional signals can still be captured even when the COST layer deteriorates. By selecting different layer pairs, ISOS/RPE or ELM/RPE, clinicians can select the functional imaging approach suited to specific disease conditions. In RP, the typical progression is COST–ISOS–RPE loss from the periphery inward, whereas in dry age-related macular degeneration (AMD), the RPE/BrM complex is often the first to show atrophy or drusen formation, followed by photoreceptor disruption [136,137]. Diseases such as BEST disease or choroideremia likewise feature early RPE impairment [138]. By pairing different retinal bands, ORG has the potential to target the layer most affected in a given disease, thus providing a versatile framework for early detection.

In future, translating ORG into broader clinical contexts will require extended testing across a range of retinal diseases, coupled with optimized hardware to accommodate larger fields of view (especially if adaptive optics are not used). As these technical hurdles are overcome, ORG's capacity for capturing rapid, localized changes in outer retinal structure holds great promise for advancing both basic vision research and clinical diagnostics.

Chapter 5. ORG characterization in retinitis pigmentosa (RP): functional assessment and longitudinal monitoring

5.1 Introduction

In this chapter, we explore the translational potential of CoORG in clinical settings by evaluating its efficacy as a biomarker for retinitis pigmentosa (RP), the most common form of inherited retinal dystrophy (IRD). We begin with a clinical overview, then use cross-sectional data from a genetically diverse RP cohort to illustrate how ORG amplitude progressively declines relative to established structural markers. We further analyze the structure–function relationship (SF-slope), identify the structural hallmarks of photoreceptor degradation, and quantify longitudinal ORG changes over two years, highlighting ORG's greater sensitivity compared to conventional biomarkers. Additionally, we demonstrate the utility of multi-layer ORG analyses in detecting residual retinal activity in regions where both photoreceptor layers are not visible Together, these findings position ORG as a sensitive, robust, and quantitative biomarker for assessing cone viability and therapeutic response in IRDs and other vision-threatening diseases.

5.2 ORG in RP

Sensitive biomarkers of retinal health are critical for monitoring disease progression and evaluating therapeutic response [139,140]. Current clinical imaging tools are limited in their sensitivity and resolution to detect subtle degradation in retinal structure and function. This precludes early diagnosis and treatment, limiting visual recovery as there is a critical window for therapeutic

intervention [141]. Optical coherence tomography (OCT) and fundus autofluorescence (FAF) are hallmark structural measures of the outer retinal complex. Primary biomarkers include the ellipsoid band width on OCT [142-146] and hyper-autofluorescent (hyper-AF) rings on FAF [147-150]. It remains unclear to what extent the remnant structure of photoreceptors still supports normal function. Furthermore, studies have shown that in advanced stages of disease, OCT and FAF reveal only minor changes over time, making it difficult to detect incremental progression or an accurate response to treatment [151,152]. Clinical functional assessments, including BCVA [153,154], perimetry [155] and electroretinogram (ERG) [156,157], offer complementary information about retinal integrity. BCVA and perimetry represent the cumulative output of the entire visual system and are thus limited in their cellular specificity. Moreover, mechanisms in the retina and cortex that compensate for photoreceptor loss can allow patients to largely overcome compromised visual symptoms until late in the disease process [59,153,158]. The gold standard measure of objective retinal functional activity is ERG, but it lacks the spatial resolution to detect localized changes, particularly in advanced stages of disease [159]. The urgent need for a non-invasive and sensitive biomarker of retinal disease progression has taken on renewed importance in the light of recent gene therapy clinical trials that have shown promise to restore outer retinal function [140,160-166].

Optoretinography (ORG) marks a significant advance in the non-invasive and sensitive monitoring of retinal structure and function in vivo. When implemented in an OCT, it provides a direct optical measure of light-evoked photoreceptor activity [56,60,62,118-123] in conjunction with the underlying three-dimensional structure. The activity is linked to the initial steps in vision that originate in the outer retina - light absorption, photoisomerization, phototransduction and the visual cycle [56,167]. A few recent studies have demonstrated the ability of ORG to detect sub-clinical changes in RP [58,59,65],

particularly in the transition zone at the border of structurally intact and progressively degenerating central island, highlighting its potential for accurate disease assessment.

We have conducted experiments on 7 RP patients using the CoORG system . Patient age, gender, genotype, and effective stimulus photon density measurements are available in Table 5.1. For the effective photon density calculation, we employed the same protocol used with CoORG's normal subjects, i.e. derived from each patient's dilated pupil size and axial length. This approach facilitates a more direct comparison between normal subjects and RP patients within similar photon density groups. One of the primary goals in documenting the various genotypes was to enable a detailed comparison with the ORG signal phenotype and its comparison with observed OCT structural phenotypes. Due to the limited number of participants, however, we have not drawn definitive conclusions yet, and work is ongoing to recruit more subjects with the same genetic mutations in order to obtain sufficient statistical power to draw inferences. Based on our current protocol and measured variability in normal controls, to achieve a statistical significance of $p<0.05$, we require a sample size of at least 6 subjects within each identical genotype group of RP patients. While genotype is our primary comparative parameter, we should ensure other influencing factors like age and photon density are grouped similarly to account for their impact.

As mentioned above, RP is the most common inherited retinal degeneration (IRD) and is the target of various therapeutic approaches [160,168,169]. Whereas no approved treatments are available to halt or reverse the progression of RP, a multi-center clinical trial is underway (NAC Attack: NCT05537220). For the first time, ORG will be included as an experimental outcome measure for the clinical trial, and there are 11 "NAC" trial participants have successfully imaged for the baseline and 9-month trial visits. Clinical and high-resolution adaptive optics (AO) imaging have revealed the prevalent outer retinal phenotypes in RP - reduction in ellipsoid zone (EZ) width [144-

[146,149,170,171], OS length [172-174] and cone density [175]. Visual acuity [176] and perimetry [155] reveal progressive visual field constriction that eventually affects the central fovea. ERG typically shows reduced or absent a- and b-waves, reflecting photoreceptor degeneration and inner retinal remodeling[157,177-179]. Overall, these metrics show between 4-13 % annual rates of RP progression [144,157,180].

Table 5.1 The information of all RP patients

Subject ID	**Age**	**Gender**	**Genotype**	**ORG stimulus effective photon density (photons/μm²)**
RP01	26	F	indeterminate	19.7×10^6
RP02	28	M	IMPDH1	18.2×10^6
RP03	60	F	RHO	15.8×10^6
RP04	23	F	PRPF31	13.4×10^6
RP05	30	F	RHO	15.5×10^6
RP06	30	F	SNRNP200	17.4×10^6
RP07	37	F	USH2A	16.3×10^6

5.2.1 The structure and function in RP

Before delving into the ORG details of RP patients, let us first examine a representative structural image from an RP patient. The *en face* image, segmented at the IS/OS layer, for an example RP patient and control subject can be seen in Figure 5.1Figure 5.1. The dark annular region in the RP *en face* image in Figure 5.1(A) distinguishes between the so-called “central island” of preserved

outer retinal structure (inside the dark annular area), the transition zone (TZ) (the dark annular area itself), and the retinal areas beyond the peripheral edge to the TZ are where the photoreceptors layers are no longer visible in OCT, indicative of severe degradation, and that the hyperreflectivity is hypothesized to come from the RPE (outside the dark annular area). For direct comparison across the same eccentricities, we have identified two regions of interest, labeled as ROI1 and ROI2 at 0.5 and 1.5 deg. respectively, each measuring 0.5x0.5 degrees.

From the results in Figure 5.1(C), it is evident that there is a notable reduction in ORG within both the HZ & HZ-TZ for the RP subject when compared to a normal control. In essence, even within the healthy region with apparently normal OCT structure, functional changes determined by the ORG demonstrate a deficit. This observation suggests that dysfunction as measured in ORG can precede structural degeneration in the transition zone and retinal regions with apparently unaffected structure. To further substantiate this observation, data from additional subjects is incorporated below.

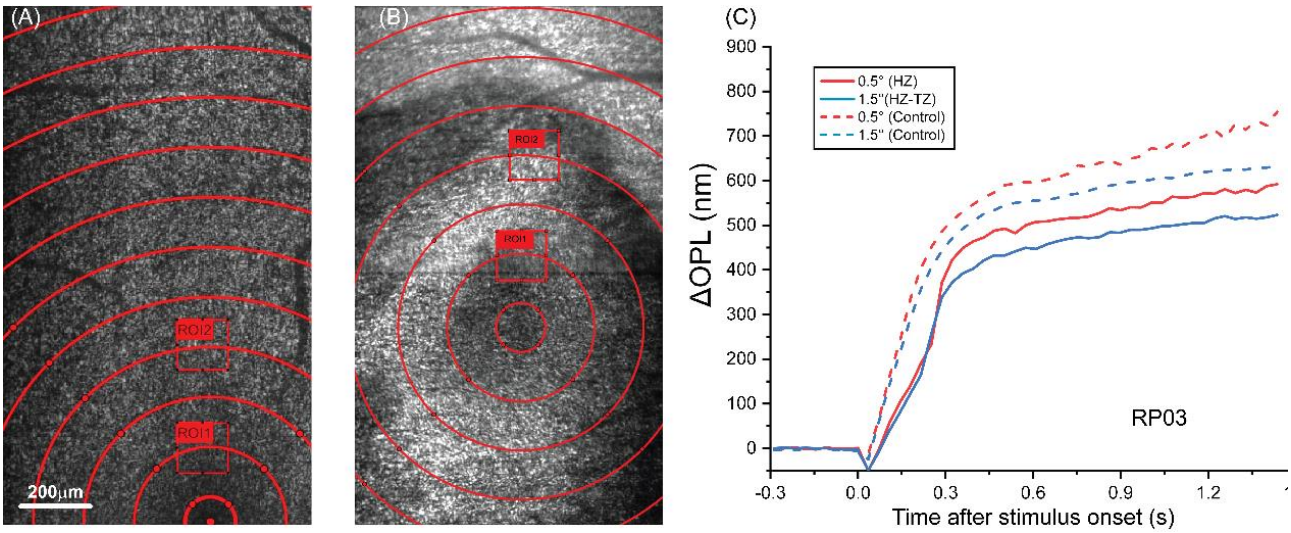


Figure 5.1 A typical RP patients' structural and control's image and corresponding ORG traces. (A) & (B) The IS/OS structural en *face* image of a normal subject and an RP patient. (C) The ORG traces

between RP & control in same eccentricities (0.5° & 1.5°, respectively). The annuli expand in increments of 0.5 degrees centered at the fovea.

5.2.2 The ORG amplitudes in whole RP patients across eccentricities

Figure 5.2 presents scatter plots for all seven RP patients, charting saturated ΔOPL against eccentricity at 0.5° intervals. A TZ onset bar is included beneath the scatter plot to distinguish between the HZ and TZ, marking the start of the transition zone. The data in Figure 5.2 reveal that for most RP patients, maximum ΔOPL generally decreases with increasing eccentricity, irrespective of the zones. Moreover, the deficit in ORG amplitude in the RP patients is observed to be as high as 32.8%, 31.4%, and 28.9% compared to normal controls at 0.5°, 1.0°, and 1.5° eccentricities, respectively. An exception is noted in the case of patient RP05, an outlier whose ORG amplitude is greater than normal controls. RP05 is an early-stage disease patient, whose genotype is suggested to be slower progressing than other forms of RP [181]. Further, in the retinal locations assayed with ORG, RP05 presents a relatively normal-appearing structural phenotype when compared to the other RP patients in this cohort. In our efforts to bolster early detection capabilities, we intend to conduct biannual monitoring of this patient, closely tracking the progression of their condition over time.

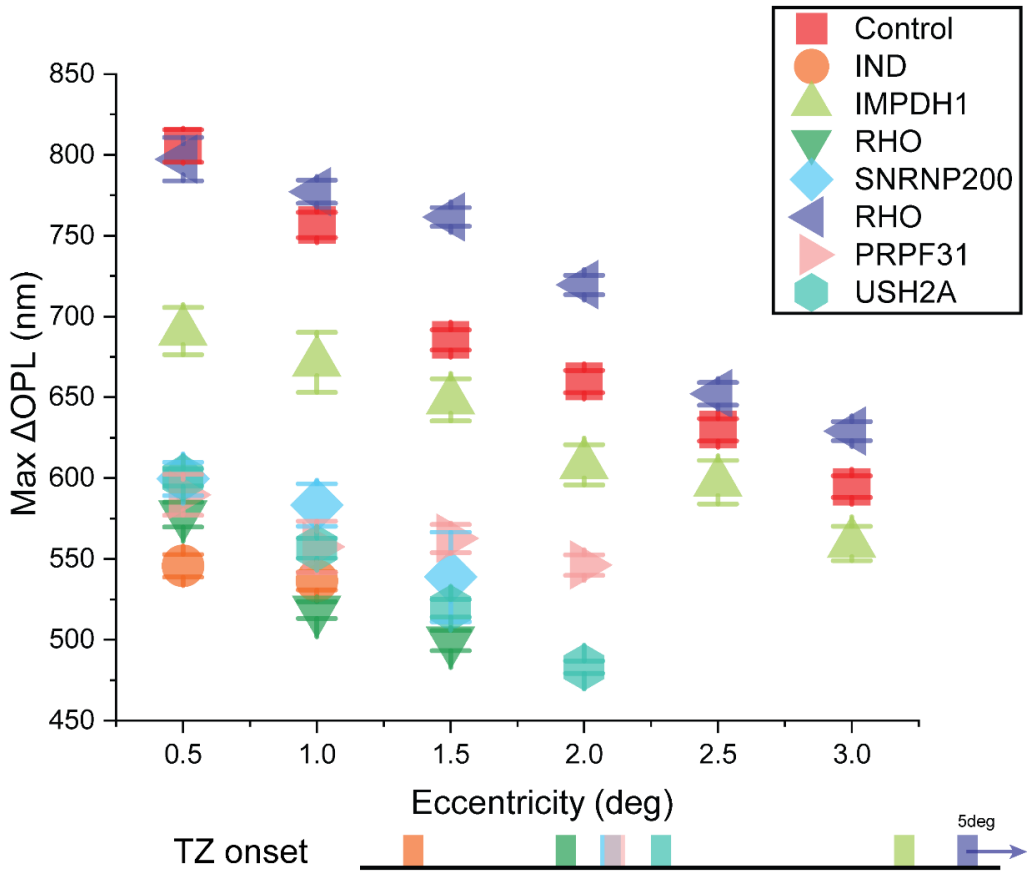


Figure 5.2 Plot of saturated ΔOPL vs. eccentricities ranging from 0.5° to 3° across seven RP patients and controls (n=8). The panel below shows the TZ onset, indicating the start of the transition zone in each patient. An arrow signifies that the range extends beyond 5° eccentricity. The purple left triangle RHO is RP05-RHO patient.

The ORG scatter plot above provides a convenient functional marker for grouping the RP by disease status. Here, we define that patients whose TZ begins beyond 3 degree retain near-normal ORG amplitudes across the imaging field and are classified here as Stage I (early stage), consistent with relatively preserved cone structure. In contrast, eyes with a TZ < 3 degree exhibit a marked depression in max ΔOPL at all locations and are defined as Stage II (more advanced stage), indicating advanced central disease progression. Although individual genetic subtypes cluster differently, under the disease stage criteria the patients do not cluster by genotype and there may

be other factors in addition to genotype that determine the rate of progression. The disease stage criteria is applied to deeper analysis in the next section.

5.2.3 Overlaying function on structure at different stages

The linear relationship between peak ORG amplitude (max ΔOPL) and OS length progressively weakens in eyes with RP (Figure 5.3). In healthy controls, max ΔOPL rises steeply with increasing OSL at a slope of 29.2 nm·μm^{-1} (n = 8), reflecting nearly proportional stimulus-induced expansion in longer outer segments. In Stage I RP eyes (with transition zones beyond 3°), the relationship remains monotonic but exhibits a reduced slope of 17.6 nm·μm^{-1} (n = 2), indicating diminished responses for a given OSL. This attenuation is more pronounced in Stage-II eyes (transition zones <3°), where the slope declines further to just 7.7 nm·μm^{-1} (n = 5), approximately one-fourth the responsiveness seen in healthy controls. Thus, RP progression not only causes shortening of OS segments but also significantly reduces their OS length-dependent biomechanical responsiveness. SF slope analysis offers a sensitive functional metric that complements structural markers of retinal degeneration. In other word, for a given structure (OS length), the cone responds less to the light stimulus as disease progresses, which might be due to the reduced waveguide efficiency or potential deficits in phototransduction.

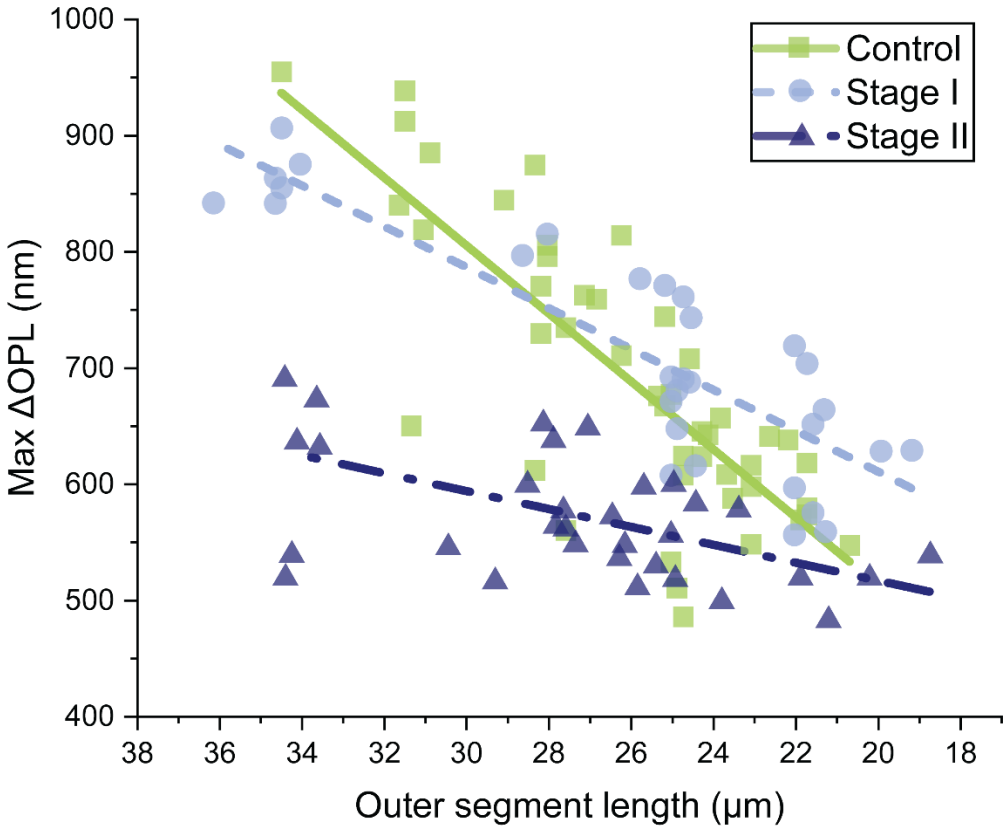


Figure 5.3 Scatter plot of maximum ΔOPL for control cones (green squares), Stage I (light-blue circles) and Stage II (dark-blue triangles) RP patients. Solid and dashed regression lines give group SF-slopes of 29.2, 17.6*, and 7.7* nm/μm, respectively (*$p < 0.05$ versus control; ANCOVA). The progressive flattening of the SF-slope illustrates the loss of length-dependent ORG gain with advancing disease.

5.3 An ORG longitudinal study of RP

Here, based on the cross-sectional study of RP, we further explore the longitudinal changes in RP. As a first application of ORG to a longitudinal study, we test the hypothesis that cone dysfunction measured with ORG precedes the deterioration exhibited by standard clinical biomarkers in RP patients. We hypothesize that the ORG can detect photoreceptors in their earliest stages of outer segment compromise, at the border of the transition zone, where structural imaging suggests

normal status. The retrospective longitudinal study spanned 12 to 21 months in 5 RP patients and compared ORG findings with EZ width and OS length in quantifying progression.

5.3.1 Study participants

Five patients (ages 23–60 years-old (yo), mean: 33.4 yo) diagnosed with RP based on clinical presentation and relevant family history at the Karalis Johnson Retina Center, Department of Ophthalmology at University of Washington were enrolled in the longitudinal study. All participants underwent genetic testing through CLIA-approved labs and four (RP02 – RP05) had a confirmed molecular genetic diagnosis (Table 5.2). Although genetic testing for RP01 was inconclusive, their clinical exam, imaging, Goldmann Visual Fields, and electrophysiology testing were consistent with RP. Research procedures followed the tenets of the Declaration of Helsinki. Eight age-matched normal controls were also enrolled in the study. Informed consent was obtained from all patients, and research protocols were approved by the institutional review board of the University of Washington (IRB#STUDY00002923). Patient characteristics are listed in Table 5.2.

Table 5.2 Characteristics of longitudinal study participants

Patient ID	**Age**	**Sex**	**Genotype**	**Clinical presentation description**	**Follow-up duration (months)**	**Change of BCVA study eye (logMAR)**	**Reduction of EZ width (μm, %)**
RP01	26	F	Indeterminate	nyctalopia, myopia,	16, 20	0	310 (15%)

				"macular cysts"			
RP02	28	M	*IMPDH1* c.942_944del, p.(Lys314del)	reduced peripheral vision, impaired dark adaptation	14, 21	0.08	72 (5.3%)
RP03	60	F	*RHO* c.165C>A, p.(Asn55Lys)	nyctalopia, increased glare while driving	9, 15	0.10	130 (13.5%)
RP04	23	F	*PRPF31* c.323-1G>T	nyctalopia, high myopia, blurring of central vision with flashes	6, 12	-0.10	23 (0.9%)
RP05	30	F	*RHO* c.68C>A, p.(Pro23His)	nyctalopia, reduced peripheral vision	8, 16	0	34 (1.5%)

Research imaging procedures were performed over three visits: baseline, first follow-up (f/u #1), and second follow-up (f/u #2), with a minimum of six months between each follow-up visit. The maximum length of follow-up ranged from 12 to 21 months. Cycloplegia was induced by 1% tropicamide ophthalmic solution for imaging.

The study involved standard clinical testing including OCT (Spectralis HRA+OCT system; Heidelberg Engineering, Heidelberg, Germany), color fundus photography and fundus autofluorescence (FAF) (Optos PLC, Dunfermline, UK). These conventional measures were compared to ORG (Figure 5.4). ORG was successfully acquired at each time point for all five RP patients.

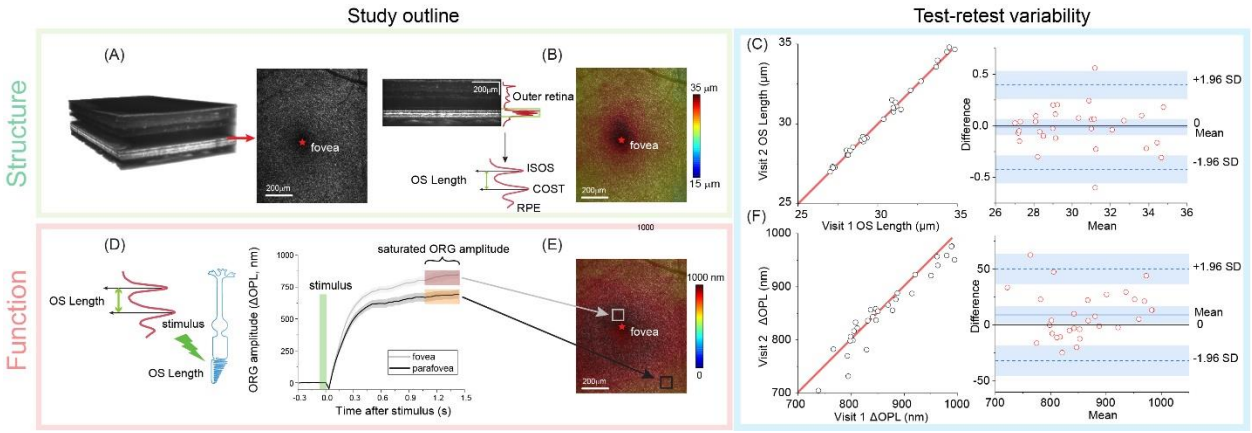


Figure 5.4 Overview of study design, illustrating the advanced structure-function assessment. OCT volumes along with the segmented en face image at the inner/outer segment-ellipsoid zone (ISOS-EZ) and outer segment tips (COST) help visualize the retinal structure (A). A zoomed-in view of OCT B-scans provides the outer retinal profile (red line) from which the OS length is obtained and plotted as a function of eccentricity in a color map (B). Warmer and cooler colors represent longer and shorter OS lengths respectively. Retinal function is assessed by measuring the change in outer segment optical path length (ΔOPL) evoked by a light stimulus (shaded green) – denoted as the ORG amplitude (D). The saturated ORG amplitude is obtained from the time evolution of the functional response, shown in (D) for a near-foveal (gray) and parafoveal (black) retinal location.

The shaded areas around the solid lines indicate the standard-deviation of repeat measurements. The variation of the saturated ORG is plotted as a function of eccentricity in a color map (E). Test-retest (left) and Bland-Altman analysis (right) shows high repeatability for both OS length (C) and ORG (F). Red line is the y=x identity line. Data points in (C) and (F) represent measurements (ORG or OS length) from same retinal locations of size 0.25° × 0.25° in the same subject taken 6 months apart.

5.3.2 ORG in RP: protocol and analysis

ORG measurements were obtained using a custom-built, line-scan spectral domain OCT system with 3° × 5.5° field-of-view, whose details are described previously [85]. First, after a 1-minute dark adaptation, fifty OCT volumes were recorded at 32 Hz (comprising 10 pre-stimulus and 40 post-stimulus volumes). Single OCT volumes were reconstructed and registered with each other to compensate for small eye movements, rendering an averaged, high signal-to-noise ratio OCT volume (Figure 5.4A) for further analysis. Next, segmentation of the outer retinal layers – the inner-outer segment (ISOS)-ellipsoid band and the outer segment tips, yielded en face 2D images of these layers (Figure 5.4A) as well as the length of the cone outer segment (Figure 5.4B). The length of cone outer segment was calculated by measuring the distance between these two retinal layers at a sampling resolution of 3.15 μm/pixel. Although EZ width is a well-recognized clinical biomarker of RP, it reflects the preserved portion of the photoreceptor inner segment and therefore does not provide information on outer segment integrity. Sub-clinical changes, such as shortening of the outer segment, can still occur within the EZ area in RP. Therefore, in addition to EZ width (Table 5.2) derived from clinical OCT based on the presence of the ISOS-ellipsoid band (as determined by three independent graders), this study also used the OS length as a structural measure of disease status. Figure 5.4B shows the characteristic decline in OS length radiating outward from the foveal center. Note that the measures of cone structure and function, OS length,

EZ width and ORG, were all obtained from the same retinal location for each follow-up visit, facilitating spatially localized comparison between them.

The cone ORG, i.e. light-evoked activity in cone OS, was measured following a green stimulus (532 ± 5 nm) of nominal photon density 1.41×10^7 photons/μm^2, chosen to provide a similar and high activation of L and M-cones. The cone ORG response is defined as the change in the cone OS length evoked by a light stimulus as a function of time, as illustrated in Figure 5.4D. It is computed as the change in optical phase (converted to optical path length (ΔOPL)) between the ISOS-EZ and cone outer segment tips (COST). In the typical single-flash stimulus paradigm shown here, the ΔOPL exhibits a rapid, low amplitude reduction immediately after stimulus onset, followed by a sharp increase and a saturated plateau (Figure 5.4D). Saturated ORG response is calculated as the average ΔOPL over ~300 ms during the plateau and converted to a color map for visualization as shown in Figure 5.4E. In a typical healthy control, the saturated ORG scales linearly with OS length (and eccentricity), whereby longer foveal OS exhibits larger ORG responses and shorter peripheral cones have proportionally reduced ORG[85], as shown in Figure 5.4B&E. Each ORG recording took 1–3 minutes, with measurements repeated 8–10 times in patients and 5 times in normal controls. The entire ORG procedure was completed in 25 ± 10 mins.

5.3.3 Test-retest variability and statistical analysis

Figure 5.4C&F illustrate scatter plots of test-retest variability (left) for OS length and ORG in a normal control, showing minimal changes over two visits, spaced 6-months apart. Each scatter plot includes the identity line (y = x), indicating strong agreement between measurements from the two visits conducted 6 months apart. Data points represent ORG and OS length measurements from the same retinal locations, ranging from the fovea to 3° eccentricity, for regions-of-interest (ROIs) of size 0.25°x0.25° in the same control subject (Fig.5.4B & E). Figure 5.4C&F display

Bland-Altman plots (right) for OS length and ORG. In these plots, the mean difference (bias) between visits is close to zero for both parameters, indicating no significant systematic bias, suggesting minor measurement variability for both OS length and ORG. The protocol shown here in Figure 5.4 for a normal control was followed in all RP patients.

To further assess the reliability and repeatability, test-retest variability was analyzed by calculating the coefficient of variation (CV) (CV = (SD/Mean) ×100%) for EZ width, OS length, and ORG across repeat measurements. Additionally, Wilcoxon signed-rank tests were used to examine intra-subject variability in reductions of these metrics, providing a means to analyze paired differences for non-normally distributed data. The CVs of 1.5% for EZ width, 3.1% for OS length, and 4.1% for ORG, confirm comparable measurement reliability across these metrics.

5.3.4 Follow-up results in ORG

Table 5.2 lists age, sex assigned at birth, genetic diagnosis, clinical presentations, follow-up duration, and changes in BCVA and EZ width of the RP participants included in the study. Over the course of follow up, there was minimal change in BCVA (Table 5.2). The EZ width captured on a commercial OCT macular B-scan revealed variable progression across the cohort. Study participants experienced a reduction in EZ width ranging from 0.9% to 15% (mean: 4.5% ± 5.9%) over varying follow-up periods of 12 to 21 months.

The most significant EZ width progression of 15% over 20 months of follow-up was seen in Subject RP01. We detail the complete procedure, including both the clinical and advanced imaging with this subject as an example (Figure 5.5). Clinical OCT B-scans and FAF images in Figure 5.5(A-B) illustrate visible changes between baseline and follow-up visits. Within the EZ area, where subtle and early changes might not be distinguishable using clinical biomarkers alone, ORG

imaging was applied to an area aligned with the FAF (blue rectangle, white ellipse, Figure 5.5B & 5.5C). At baseline, near the border of the transition zone (red ellipse), a complete loss of OS tip reflection precludes reliable OS length and ORG measurements. The OS length map shows a radial decrease from the fovea to the periphery both at baseline and follow-up. However, at follow-up, a reduction in OS length is noted at the outer edge of the measurable region, which is greater in magnitude for the temporal retina. The ORG map follow-up reflects the patient's general trend of overall reduction in OS length, with the temporal meridian showing greater progression. In both OS length and ORG, the progression is expectedly most evident at the frontier of structural degeneration at the border of the central island and transition zone. To highlight changes between baseline and follow-up, a difference map was generated with values ranging from 0 – 1, calculated as (Vbase – Vf/u)/Vbase. The same formula is applied to both OS length and ORG to quantify the reductions over time. In Figure 5.5D-E, the difference map reveals a sharper transition at the border of the central island in ORG compared to OS length. Together, Figure 5.5D-E demonstrate that, even in regions appearing intact on FAF and OCT, ORG not only reveals progressive changes in retinal structure but also reduced function over time.

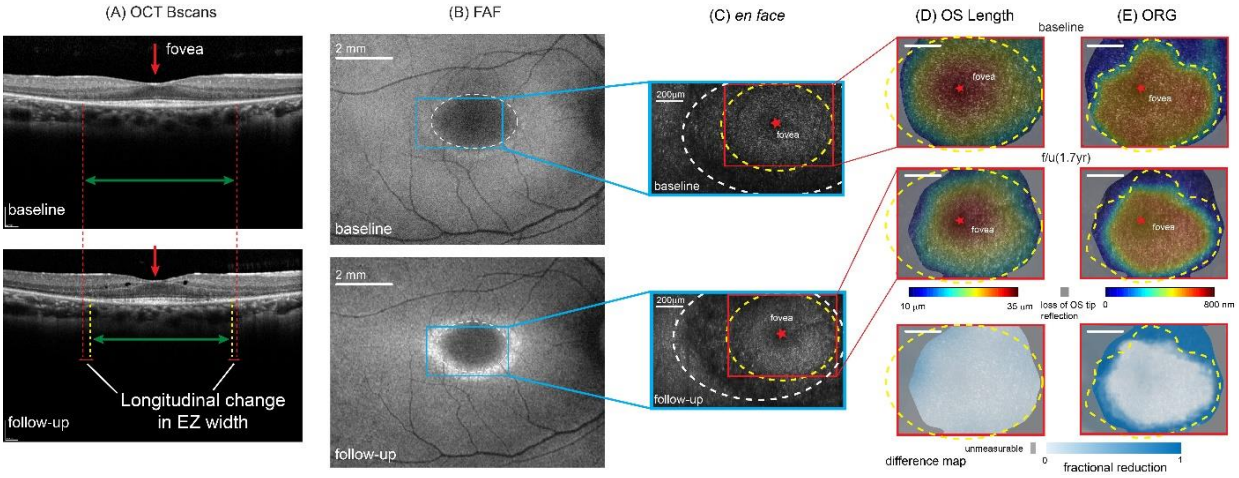


Figure 5.5 Example longitudinal study analysis pipeline for RP01. (A) Clinical OCT B-scans from baseline (top) and follow-up (bottom) visit. Red arrows indicate the fovea. Red & yellow dashed lines mark the EZ width boundaries at baseline and follow-up respectively. (B) Fundus autofluorescence (FAF) from baseline (top) and follow-up (bottom) visit. The white dashed ellipse outlines the EZ area, while the blue rectangle marks the region selected for further OCT-ORG analysis. (C) En face images for baseline (top) and follow-up (bottom), with the corresponding EZ area from (B) marked as a white dashed ellipse. The yellow ellipse highlights the area chosen for OSL and ORG analysis, based on the preservation of all outer retinal layers. Maps of (D) OS length and (E) ORG amplitude are shown for baseline (top) and follow-up (bottom). The difference maps between the follow-up visits are displayed for OS length and ORG. An outline (yellow) is drawn in all OS length and ORG maps, as reference for comparison between baseline and follow-up visits. The scale bar in (D-E) is 200 μm.

Figure 5.6A-5.6C display *en face* OCT images segmented at the ISOS-EZ, OS length maps, and ORG amplitude maps for RP03, RP04 and RP05. The difference maps are also shown for OS length and ORG amplitude to denote disease progression. The red boxes indicate ROIs selected for ORG. The gradual reduction in OS length and ORG versus eccentricity is evident both at baseline and follow-up for all cases, similar to normal controls (Figure 5.4). In RP03, both OS length and ORG show a significant reduction along the edge of the central island and border of the transition zone (Figure 5.5B, yellow dashed line). The difference in structural and functional readouts are apparent, where the OS length shows a gradual reduction at the edge of the measurable region at baseline, while the ORG shows a more drastic decline.

In RP04, OS length changes are minor and nearly indistinguishable upon visual inspection of the color maps. Yet ORG reductions are observed, where only minor changes are observed in cone structure as assessed by OS length (yellow arrows, Figure 5.5). In the early-stage patient RP05, as defined by minimal symptoms and greater preservation of clinical metrics, both OS length and

ORG remained stable over time and no changes were apparent upon visual inspection. Of note, RP03 (age: 60 yo) and RP05 (age: 30 yo) are both affected by variants in the RHO gene (RP03: c.165C>A, p.Asn55Lys; RP05: c.68C>A, p.Pro23His in RP05), but exhibit distinct rates of progression presumably due to differences in their age and stage of disease.

The ORG maps reveal a drop in amplitude at the peripheral borders of the measurable regions over time, whereas OS length shows comparably lower reductions in the same areas. On the other hand, OS length and ORG remain more stable near the fovea, indicating structural and functional preservation in locations away from the active area of degeneration, i.e. the transition zone. Although the disease progression is minimal near the fovea, the absolute ORG magnitude is indeed decreased in RP compared to normal controls (see Table 5.3). Previously, the reduction of ORG in the parafovea was shown to correspond with normal microperimetry in RP [59]. These qualitative observations highlight nuanced structural and functional changes detectable by ORG, even in regions previously considered stable via standard clinical assessment. Next, we performed a quantitative comparison between ORG, OS length and EZ-width as an objective basis for evaluating progression in RP.

Table 5.3 Comparison of ORG and OS length between RP patients and normal controls in the central island

Patient ID	ORG in central island (nm)	OSL in the central island (μm)	Reduction of ORG (%)	Reduction of OSL (%)
RP01	545.8 ± 7.0	29.3 ± 0.6	32.1	5.2
RP02	690.9 ± 14.6	24.6 ± 0.2	14.1	20.4
RP03	577.4 ± 7.6	27.4 ± 0.3	28.2	11.3
RP04	645.1 ± 7.5	31.6 ± 0.3	19.8	-2.2
RP05	797.4 ± 13.5	28.1 ± 0.3	0.8	9.1
Control (n=8)	803.9 ± 9.6	30.9 ± 0.3	-	-

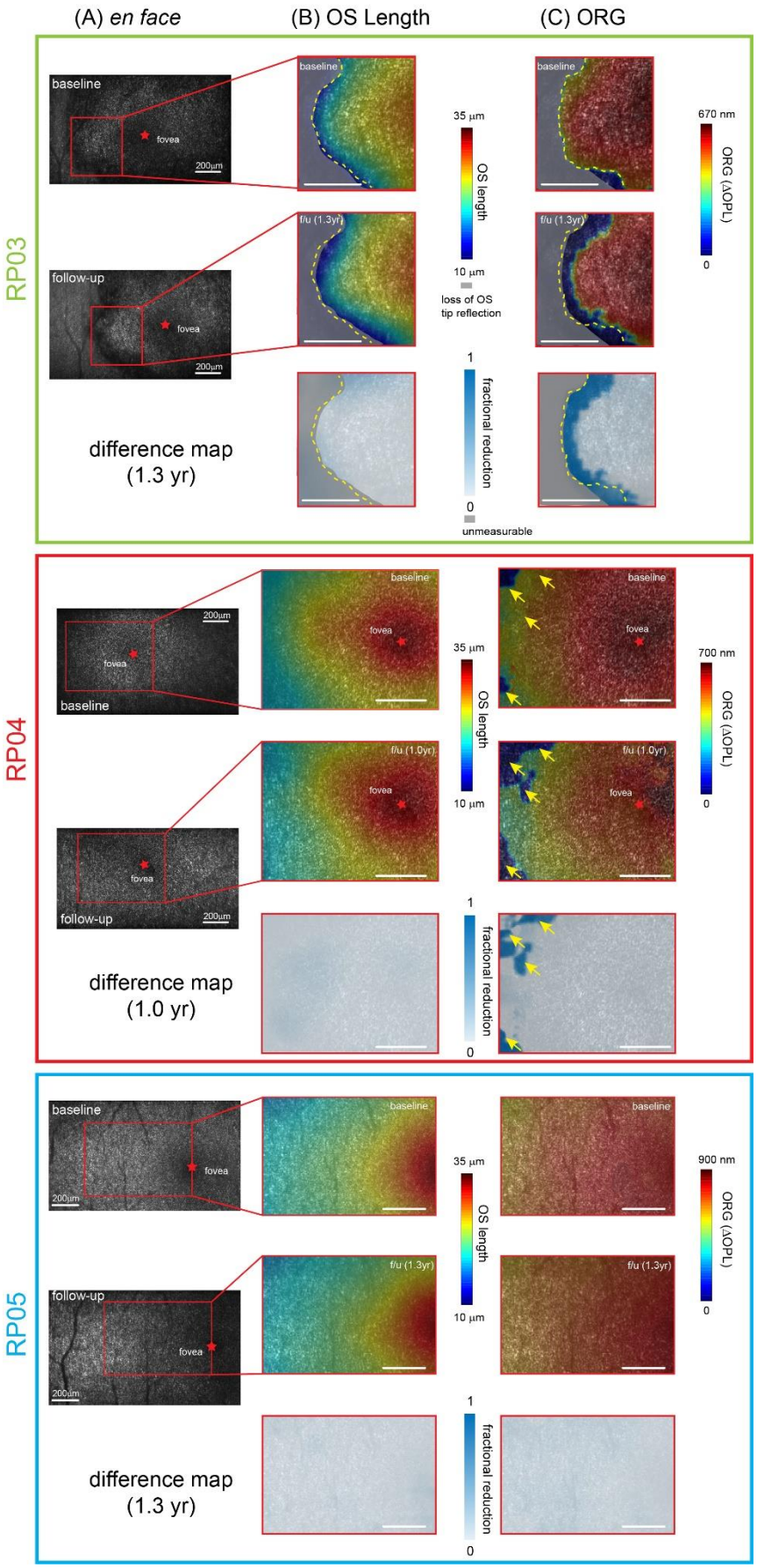

(A) en face
(B) OS Length
(C) ORG
RP03
baseline
fovea
200μm
follow-up
f/u (1.3yr)
difference map
(1.3 yr)
35 μm
OS length
10 μm
loss of OS
tip reflection
1
fractional reduction
0
unmeasurable
670 nm
ORG (ΔOPL)
0
RP04
f/u (1.0yr)
difference map
(1.0 yr)
700 nm
RP05
900 nm

Figure 5.6 Longitudinal follow-up in RP03, RP04, and RP05, displaying the progression from the initial baseline visit to the most recent follow-up. (A) Baseline and follow-up *en face* images at the ISOS-EZ band and the corresponding ROIs (red) selected for OS length and ORG analysis. Maps of OS length and ORG are shown in (B) and (C) respectively. Their corresponding color bars denote the variation in OS length and ORG response amplitude. The difference maps between the follow-up visits for OS length and ORG are shown for each patient. Yellow dashed lines and arrows indicate the same location for reference across follow-up visits. The scale bar is 200 μm.

To derive relevant metrics for disease and potential clinical trials, we divided the ORG into three spatial sections for further assessment: ORGtot denoting the overall ORG amplitude across the measurable region, where the measurable region is defined by the presence of both the ISOS-ellipsoid and COST bands; ORGedge denoting the ORG response in the border region surrounding the structurally intact central island; and ORGcent denoting the ORG response in the central region. The definition and retinal eccentricities corresponding to ORGedge, the start & end of the transition zone for all patients are detailed in Figure 5.9 and Table 5.5. This is analogous to the "hill of vision" metric [182,183] for documenting the rate of progression in established natural history studies such as the USH2A-related retinal degeneration RUSH2A study. ORGedge and ORGcent were calculated based on the mean ORG of 10 regions of interest, each of size 0.25° × 0.25°, near the edge of the central island and in the central region respectively (marked by white dots in Figure 5.7A). The ORGtot was calculated based on the mean ORG of 17 ROIs from the central region to the border of the whole measurable area (white dashed line in Figure 5.7A). The comparison between these spatially distinct metrics is shown in Figure 5.7B. ORGedge is the most sensitive for assessing progression and demonstrates the largest reduction in its magnitude over time, highlighting the active degradation due to the disease process at the boundary of the transition zone. By comparison, ORGcent shows only a minimal reduction ($p > 0.05$) over time, but remains

overall lower in magnitude compared to controls (Table 5.3). The corresponding values of OS length for the same spatial sub-divisions - indicated as OSLtot, OSLedge, and OSLcent - are illustrated in Figure 5.7C. The greater reduction in OSLedge compared to OSLtot and OSLcent is evident in RP01, RP03 ($p<0.01$) and RP04 ($p<0.05$), while this difference is not apparent for the other two patients.

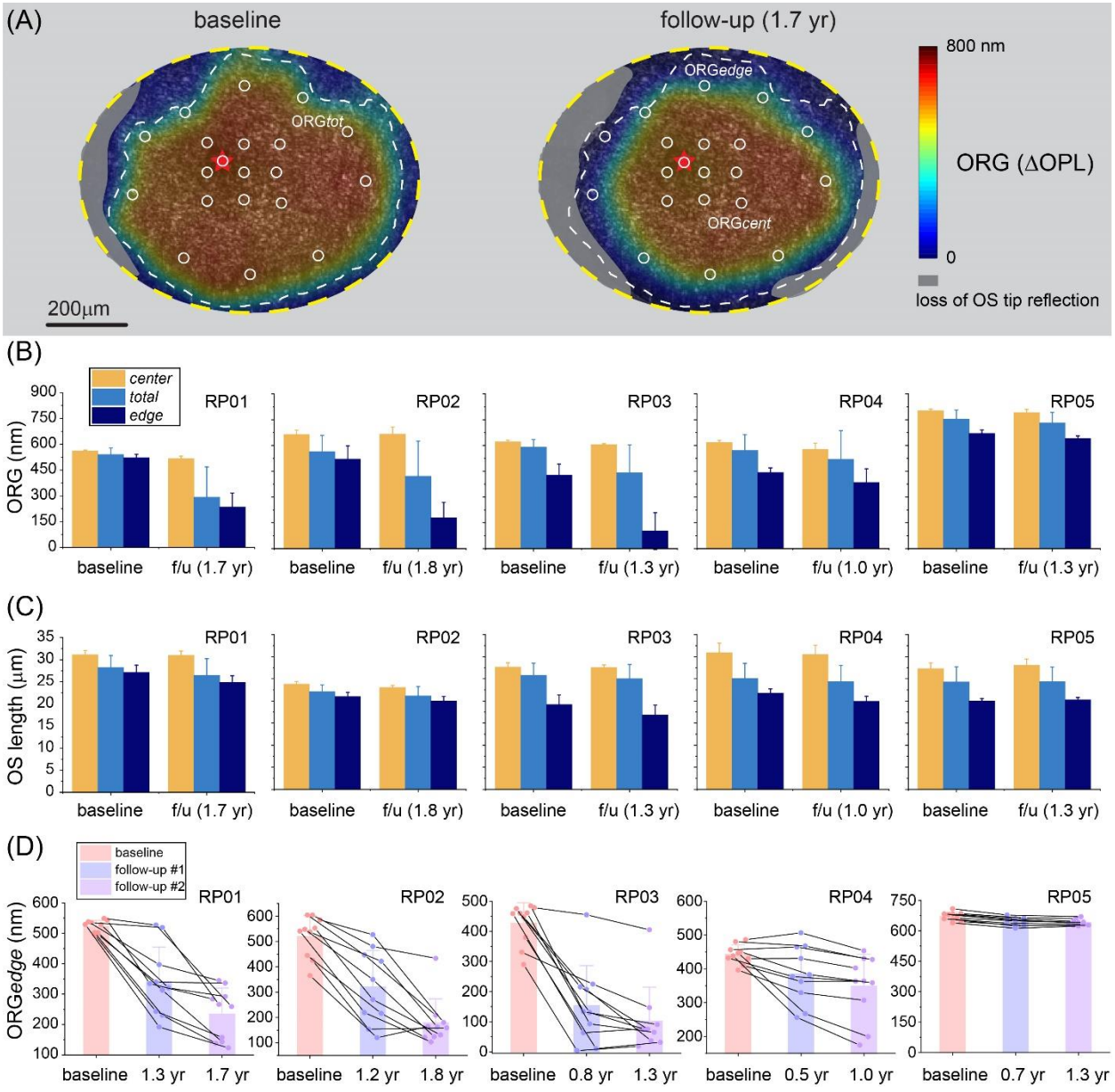


Figure 5.7 Quantification of RP disease progression. (A) The ORG maps are divided into regions-of-interest (ROIs) (white circles) to allow regional comparison of photoreceptor dysfunction. ORGedge and ORGcent are derived as the mean of 10 ROIs in the border region surrounding the structurally intact central island and the central region, respectively, while ORGtot is obtained as the mean of 17 ROIs across the entire ORG map. The fovea is indicated by a red star. (B) Comparison of regional metrics derived from ORG, including ORGtot, ORGedge, and ORGcent (C) The corresponding metrics for OS length, including OSLtot, OSLedge, and OSLcent are shown. The colors of legend in (B) & (C) are identical, representing the center, total, edge regions respectively in each subject. Error bars in (B) & (C) represent the standard deviation of values obtained from the different ROIs (10 ROIs each for center and edge, 17 ROIs for total). (D) Scatter and bar plots show the progression of ORGedge amplitude over time. The different colors represent baseline, first and second follow-up visits, respectively. Connecting lines illustrate ORGedge changes for the same location across the different follow-ups.

With the knowledge that ORGedge was the most sensitive in detecting longitudinal changes, we plotted the change of ORGedge amplitude for the three visits (baseline and the two follow-ups (Figure 5.7D)). The fractional reduction in the difference map was converted to a percentage reduction as : 100 x (Vbase – Vf/u)/Vbase. It is evident that by 9 months after their baseline visit, there was detectable disease progression in RP03 and RP04, as indicated by the reduction in ORGedge at the first follow-up, equal to 65.1% and 13.5% respectively. For RP01 and RP02, the first follow up of 16 and 14 months respectively showed an ORGedge reduction of 34.9% and 40.7% respectively. There was a notable decrease in ORGedge amplitude for all patients at both follow-ups, apart from RP05: f/u #1: mean = 31.5% ± 6.7% (range: 3.6% - 65.1%) and f/u #2: mean = 44.7% ± 5.3% (range: 4.3% - 76.7%). For RP01 – 03, the progression was statistically significant for both follow-ups compared to baseline ($p < 0.005$). For RP04, the progression from baseline to 1st follow-up was not statistically significant ($p = 0.084$), while the progression from

baseline to the 2nd follow-up was significant ($p = 0.02$). In these four cases, cone function deteriorated significantly in the time-interval between the two follow-up visits, demonstrated by the larger ORG reduction at the second follow-up. The most advanced stage patient within the cohort (RP03) also demonstrated the largest reduction in ORGedge (65.1% and 76.7% respectively at 9 and 15-month follow up).

We then compared ORGedge to standard clinical metrics of outer retinal structure (Figure 5.8). Comparison of the reduction in ORGedge against EZ width and OS length for the most recent follow-up visits is shown. Note that OS length in Figure 5.8 is obtained from the same retinal locations as ORGedge, facilitating a direct comparison between cone structure and function for each ROI. While the reduction in ORGcent is minimal across all five RP patients (mean: 1.3%; range: 0.3% - 3.0%), a significantly greater reduction in ORGedge amplitude was observed compared to OSL and EZ width for RP01, 02, 03 and 04 ($p < 0.02$, Wilcoxon signed-rank test). For RP05, the small but significant reduction in ORGedge was not accompanied by changes in EZ width. Deterioration in cone structure, measured by a reduction in OSL and EZ, was less pronounced; the change in OS length and EZ-width was 5.7% ± 1.2% and 4.5% ± 5.9% respectively. The reductions in EZ width versus OS length were not statistically different except for in RP04. Overall, these findings demonstrate that ORG detection of cone dysfunction precedes the loss of cone structure and provides an early and otherwise sub-clinical biomarker of disease progression.

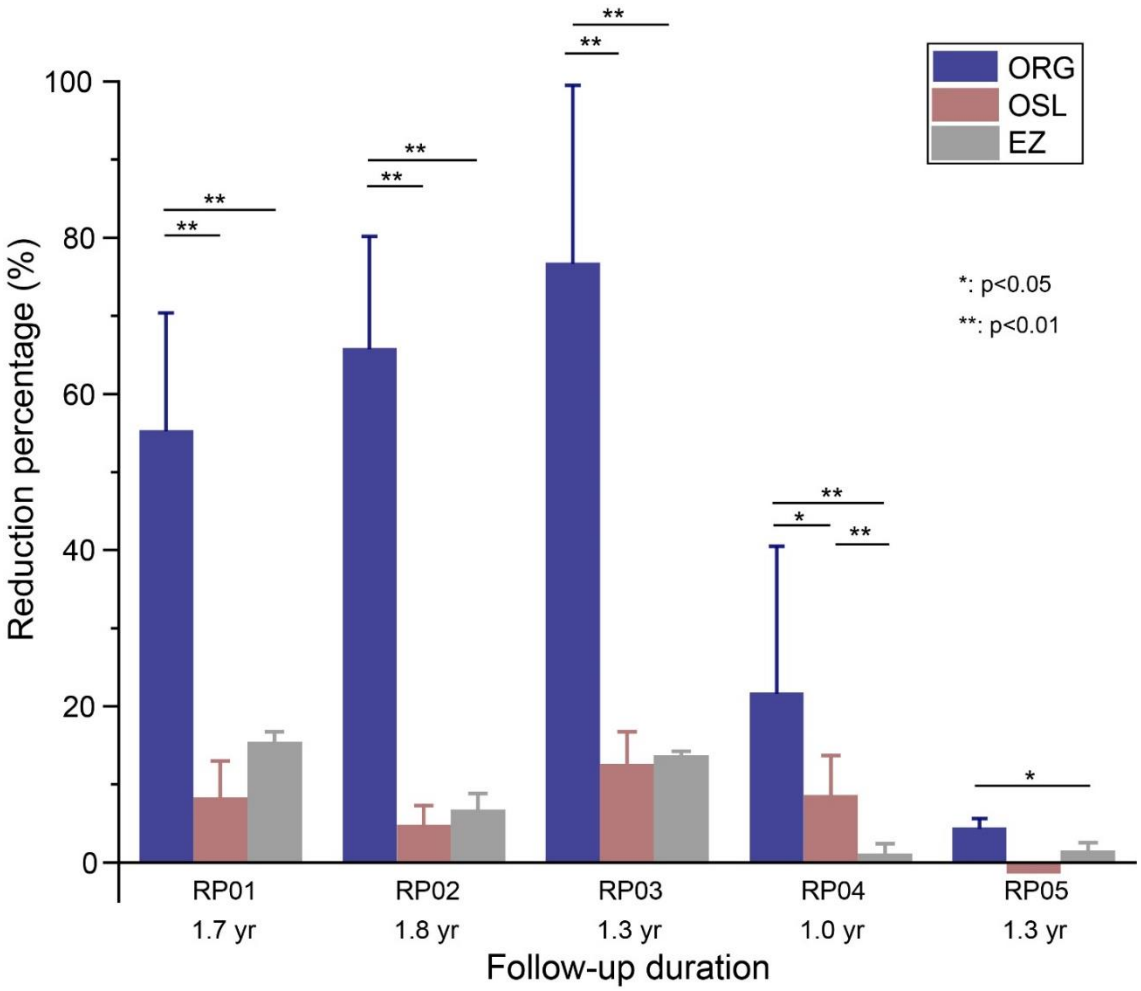


Figure 5.8 Comparison of different biomarkers for measuring RP disease progression. Percent reduction in ORG, OS length, and EZ-width between baseline and the latest follow-up visit for the five RP patients is shown. The ORG and OSL values are those obtained from the edge of the central island, ORGedge and OSL*edge* respectively. Statistical significance values obtained from the Wilcoxon signed-rank test are noted. Error bars for ORG & OS length represent the standard deviation of values obtained from different ROIs (10 ROIs each for ORG*edge* and OSL*edge)*. For EZ-width, the error bar represents the standard deviation of repeat measurements from three independent graders.

The follow-up duration varied among the five patients. Therefore, the progression was quantified as an annual rate of change, summarized in Table 3. In all RP patients, except RP05, the annual

rate of ORG reduction was significantly greater compared to the other two structural biomarkers – OSL and EZ. However, the observation period was only 2 years in this study, constituting a limitation, though still a sufficiently long timeline in which to observe a significant decline in ORG.

Table 5.4 Annual rate of progression, as defined by the reduction in different biomarkers

Patient ID	ORG† (%/yr)	OS length† (%/yr)	EZ width (%/yr)
RP01	33.1	4.9	9.2
RP02	37.6	2.7	3.8
RP03	61.3	10.0	10.8
RP04	21.6	8.5	0.9
RP05	3.3	-0.9	1.0

†: Values denote the annual percent reduction at the border of the central island, i.e. ORGedge & OSLedge

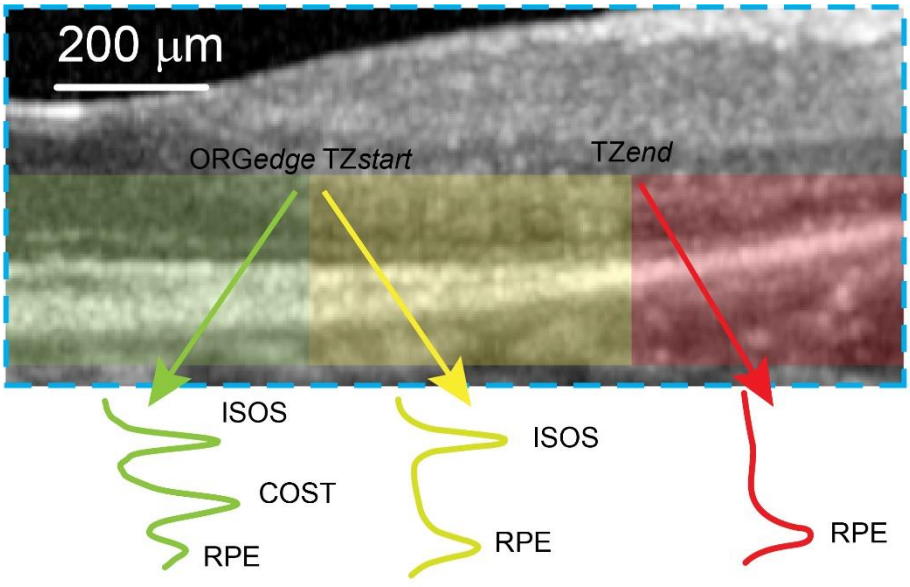


Figure 5.9 Defining ORG*edge*, TZ*start* and TZ*end* in the OCT A-scans and B-scans. The ORGedge is defined as the most peripheral retinal location where all three outer retinal bands are intact in the CoORG system. The TZstart is defined as the location in Heidelberg OCT B-scan where the COST reflection is absent while ISOS-EZ and RPE bands are visible. The TZend is defined as the location in Heidelberg OCT B-scan where only the RPE band is visible.

Table 5.5 Disease progression of patients diagnosed with RP

Patient ID	**TZ_{start} at baseline (deg)**	**TZ_{end} at baseline (deg)**	**TZ_{start} at f/u (deg)**	**TZ_{end} at f/u (deg)**	**ORG_{edge} at baseline/follow-up (deg)**
RP01	1.3	3.5	1.2	2.9	1.1
RP02	3.3	5.0	3.2	4.4	3.1
RP03	1.9	3.4	1.8	3.0	1.6
RP04	2.1	4.4	2.1	4.4	2.0
RP05	5.2	8.1	5.2	7.9	4.0[#]

[#]The ORG_{edge} region for RP05 was limited to 4 deg, given the current imaging protocol. While this eccentricity is sufficient to cover the transition zone of the other patients, RP05 was the most early-stage patient in this cohort with the TZ extending to 7.9 deg.

5.3.5 Discussion

This is the first study to assess longitudinal disease progression using ORG and highlights its potential as a sensitive biomarker to precisely monitor progression of outer retinal disease. While RP was chosen as an example of outer retinal degeneration to assess the sensitivity of ORG to detect progression, the findings could be applicable across a broad range of primary and secondary photoreceptor diseases, including geographic atrophy in age-related macular degeneration (AMD)

and other inherited retinal diseases, where the structure and function of the outer retinal complex is compromised [151,184,185]. The evolution of ORG used in this study, dubbed CoORG or Coarse-scale ORG, does not require an adaptive optics module and sacrifices cellular resolution for increased field-of-view and high-throughput, patient-friendly imaging [85]. Furthermore, patients with characteristics such as cataracts and excessive eye movements that would preclude adaptive optics imaging are accessible within the CoORG paradigm. Longitudinal study of the same patients and retinal locations over time as demonstrated here offers inherent control over inter- and intra-subject dependent factors that cause variability in the ORG, facilitating effective comparisons. In the future, documenting the normative characteristics of the ORG versus eccentricity [85] and age are important considerations for its wide-spread application.

Disease progression measured in ORG was compared to standard clinical assays. EZ width in OCT is one of the key biomarkers that reflects the remnant inner-segment-EZ structure of the photoreceptors. Here, we observed a 5% annual decline in EZ width in our cohort, a finding that closely aligns with the 5-7% reduction rate reported in previous studies [144,149]. While EZ width is a highly repeatable marker of advanced-stage outer retinal degeneration [145,180], it does not convey functional information of the outer retina, nor the viability of the photoreceptor outer segment. The constriction of hyper-AF rings observed in FAF provides a biomarker for progression and is shown to have low test-retest variability [180]. In RP, the annual horizontal and vertical rates of decline in hyper-AF ring size were reported to be 4.1% and 4.0%, respectively [180]. In our study, we observed similar rates of annual decline over a 5-year period for RP01, with horizontal and vertical reductions of 4.1% and 3.4%, respectively.

As an add-on to OCT imaging, the ORG seamlessly integrates the assessment of structure and function in the same platform with high sensitivity and spatial localization, enabling the detection

of functional changes that are anchored to clinically relevant structural disease phenotypes such as EZ width and OS length. This is of critical importance not only to compare against standard clinical measures of retinal structure but also to obtain granular insight into the spatially heterogeneous pattern of disease progression, such as in sectoral RP or geographic atrophy. As expected from the typical pattern of progression in RP, from the periphery to the fovea, the highly variable border region denoted by ORG*edge* showed the largest reduction over time. In contrast, cone function in the central island, denoted by ORG*cent*, showed minimal change over time. (Figure 5.7B-C). However, cone function in the central retina appeared to be compromised compared to controls even at the first time point, as shown in Table 2, consistent with cross-sectional reports of ORG in RP [58,59]. The ORG*tot* shows intermediate reduction in cone function compared to ORG*edge* and ORG*cent* (Figure 5.7B). Overall, targeted regional analysis as introduced here for ORG, based on previous suggestions for visual sensitivity [182,183] , enables capturing the spatially localized and heterogenous pattern of disease progression as well as its comparison against more global clinical metrics.

As shown in Fig 5.8, the reduction in cone function with ORG over time exceeds that observed in EZ width and OS length. EZ width and OSL decreased by 4.5% ± 5.9% and 6.5% ± 1.4%, respectively (Figure 5.8), approximately 9.9 and 6.9 times less than the reduction noted in ORG*edge*. The ORG*edge* revealed an average reduction of 44.7% ± 5.3% including the very early-stage subject (RP05). If RP05 were excluded, the mean ORG reduction in the remaining patients would increase to 54.8% ± 3.1%. The comparison against ORG*tot* was more modest, where reduction in overall cone function with ORG exceeds reductions in EZ width and OS length by 2.7x and 1.9x respectively (12.3% for ORG vs. 4.5% for EZ width and 6.5% for OS length). Whereas the EZ width can be treated as global metric of outer retinal health encompassing both

the central island and the transition zone, the breakdown of OS length into *edge*, *center* and *total* allows a more regional comparison between structure and function. Comparing Figure 5.7B versus Figure 5.7C, it is evident that reduction in cone function over time generally exceeds the reduction in OS length, whether assessed at the edge of the central island, or as a whole.

The growing landscape of clinical trials, including the advancements in novel gene-augmentation and gene-agnostic therapies for outer retinal diseases, underscores the need for outcome measures that are safe, sensitive, and efficient. These measures are particularly critical at early time points, when interventions may be most effective, or when the therapeutic effects can be assessed earlier during a clinical trial. The approval of voretigene neparvovec (Luxturna) for patients with *RPE65* mutations causing Leber Congenital Amaurosis (LCA) represented a major advance in human vision restoration using gene therapy. In addition, gene-editing for *CEP290*-associated retinal degeneration has shown promising early results in clinical trials. In the context of geographic atrophy in AMD, pegcetacoplan and avacincaptad pegol drugs have recently received FDA approval for slowing disease progression by targeting the complement pathway [186-188]. EZ-width and FAF are commonly used as clinical trial outcome measures. Efforts aimed at slowing or reversing disease progression would benefit from a faster and more sensitive biomarker that could ultimately lead to a shorter pathway for therapeutic testing and approval. This study marks a significant step in this direction. The low test-retest variability (~4%) coupled with the high sensitivity in detecting annual rates of reduction in cone function highlights the potential of ORG to augment longitudinal studies of retinal disease and response to therapeutic interventions. Accordingly, for a treatment to show measurable effect with ORG, it would need to exhibit a minimum of 4% preservation or restoration of cone function, while a treatment effect would be measurable in a significantly shorter timespan compared to the current outcome measures.

The study sample size is small, which may constrain statistical power and generalizability, specifically with respect to drawing genotype-phenotype correlations. In addition, the longitudinal study duration is limited to 21 months. Nevertheless, the ORG measurements showed a high test-retest reliability over repeat measurements, and significant disease progression was observed with ORG, even within the relatively short timeframe and in those with limited progression with standard clinical imaging. Another limitation of our study is the lack of longitudinal microperimetry in the same subjects. The addition of this important biomarker would enable relating the change in visual field to the degradation noted here in ORG and retinal structure. ORG methods that measure the light-evoked changes in backscattered intensity suggest a correlation between perimetry and ORG[65,66,123].. On the other hand, previous work using phase-based ORG has shown that retinal areas with sub-normal cone function measured with ORG [58,59] may exhibit normal visual sensitivity in RP. In addition, IRD patients with loss of up to ~62% of cones still exhibit normal visual acuity and sensitivity [153]. This suggests that subjective tests of visual function may be less sensitive compared to objective tests of cone function such as ORG in tracking progression. Finally, the ORGs here were undertaken without AO, precluding the cellular-scale assessment of longitudinal progression. Future ORG measurements with AO are expected to further enhance the sensitivity of mapping disease progression.

Overall, this study highlights the ability of ORG to capture early changes in photoreceptor function over time that are otherwise undetectable in standard clinical imaging and often precede structural deterioration. By enabling the detection of functional impairments before structural changes become apparent, ORG is poised to play a pivotal role in clinical practice and therapeutic trials. As treatments continue to evolve, the incorporation of ORG into clinical trials will accelerate the

timeline and improve sensitivity for monitoring treatment efficacy, ultimately shortening the assessment period and enhancing patient outcomes.

5.4 Multi-layer applications in RP

Beyond offering fundamental insights into normal outer retinal function and mechanics shown in chapter 4, this broader ORG framework holds significant promise for clinical applications. Each ORG component offers a quantifiable, layer-specific readout of retinal function, so deviations in these signals can serve as sensitive indicators of disease even when routine structural exams appear normal [189]. In RP, an inherited degenerative retinopathy primarily affecting photoreceptors[190], ORG has already demonstrated the ability to detect diminished photoreceptor responses in vivo that precede overt cell loss [58,59]. Here, by studying different retinal bands, we ask what layer is most affected in a diseased state. Here, ORG offers disease-specific flexibility based on specific retinal layer pairs: γ-ORG (ISOS–RPE), representing the incorporated response of photoreceptor OS & subretinal space, facilitates expanded field-of-view (FOV) dysfunctional detection in the TZ—a key site in RP where COST reflections often diminish. By capturing such functional deficits on a localized, precise scale, ORG can map regions of subclinical dysfunction in retinopathies, offering a more sensitive metric for disease progression and a potential outcome measure for therapies (e.g. gene or stem-cell therapies aimed at restoring photoreceptor activity).

Using the normative findings from Figure 4.8 as a baseline, we next examined the potential of γ ORG (ISOS - RPE) for assessing retinitis pigmentosa (RP), a prototypical IRD characterized by progressive cone photoreceptor deterioration. As the disease advances, the reflectivity of COST layer degrades first, followed by the ISOS layer. Based on this progression, we categorized the retina into three zones: a healthy zone (HZ) with intact ISOS, COST, and RPE; a transition zone

(TZ) retaining only ISOS and RPE; and a disease zone (DZ) where evidence of cones is largely absent, shown in Figure 5.10A. Traditional ORG relies ISOS and COST presence to measure ORG, which in this study is defined as α ORG. The α ORG alone would therefore limit assessment to the HZ (shown in the ISOS *en face* image yellow dashed irregular circle), whereas using γ ORG expands the measurable region from ~1.3° to 2°, representing a 136% increase in coverage and offering a more comprehensive diagnostic window.

Figure 5.10 (B) illustrates a typical example of the eccentricity-dependent variation in γ ORG responses across time from 0.25° to 2°. Based on Figure 5.10(A), TZ boundary was demarcated at 1.4°. The plot shows that γ ORG in the TZ is substantially lower than in the HZ. Pooling data from all six RP subjects, we then compared HZ amplitudes with corresponding eccentricities in normal controls; as shown in Figure 5.10(C), RP exhibits a notable reduction in γ ORG from the near fovea to the parafovea. Further analysis of the TZ in RP, relative to normal controls (Figure 5.10D), reveals an 18.1% amplitude decrease in the HZ and an 80.4% decrease in the TZ. Closer to the TZ–DZ boundary (TZ end), γ ORG can even become negative, suggesting why the TZ amplitude is roughly 70% below normal levels. These results indicate that γ ORG can detect retinal deterioration earlier and across larger retinal areas compared to the traditional ISOS-COST response (α ORG), providing novel insights and expanding its potential as a clinical tool for the assessment and monitoring of various retinal diseases.

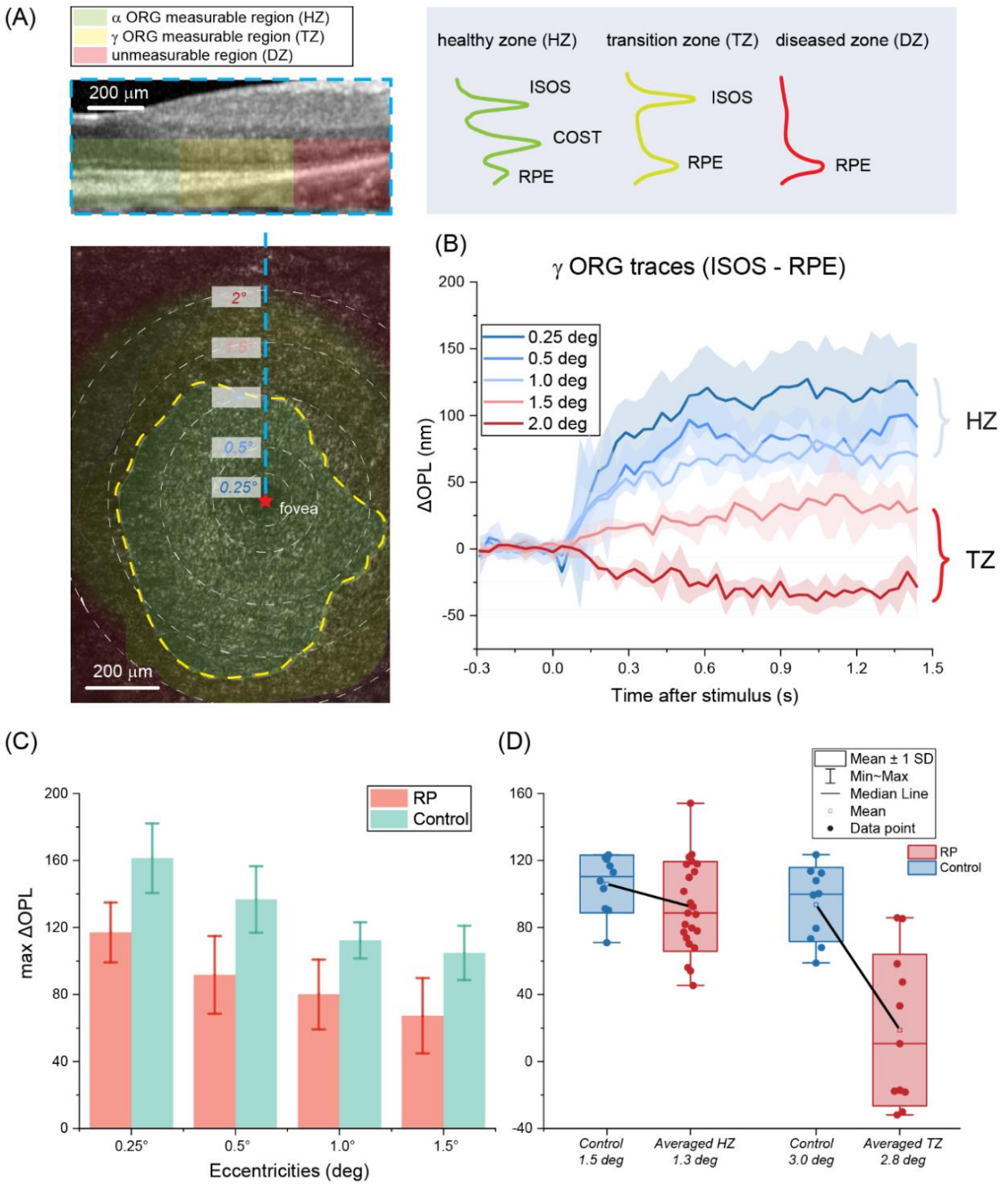


Figure 5.10 Clinical application of the γ ORG in RP patients. (A) Illustrates the definition of healthy zone (HZ), transition zone (TZ), and diseased zone (DZ) based on a representative A-line profile and an ISOS *en face* image, where the yellow dashed circle denotes the boundary of HZ at

approximately 1.4deg in the temporal meridian (blue dash vertical line). (B) Shows the corresponding γ ORG traces, with blue bins indicating the HZ and red bins the TZ. (C) Compares the saturated γ ORG amplitudes in the HZ of RP patients versus matched eccentricities in controls, while (D) presents box-and-whisker plots highlighting differences in both the HZ and TZ between RP patients and normal subjects.

Chapter 6. ORG in Acute zonal outer occult retinopathy (AZOOR) patient with advanced scotoma

6.1 Introduction

In this chapter, we extend CoORG to acute zonal occult outer retinopathy (AZOOR), an uncommon retinal disorder characterized by rapidly expanding central or pericentral scotomata[191,192], often with minimal structural findings on conventional fundus imaging and subtle OCT abnormalities. AZOOR presents diagnostic challenges because psychophysical tests identify functional deficits without revealing cellular-level information, while structural OCT often fails to detect early functional losses. Consequently, AZOOR serves as an ideal model for evaluating CoORG's ability to precisely map residual photoreceptor function. After briefly reviewing the clinical characteristics and hypothesized autoimmune origins of AZOOR, we present structural *en face* and ORG maps from patients with advanced central scotomata. These maps uncover discrete islands of preserved cone activity within or immediately adjacent to structurally ambiguous OCT regions. By analyzing stimulus ORG curves and separating early receptor potential, photoisomerization, and phototransduction, we could illustrate CoORG's potential utility in monitoring subclinical progression or therapeutic intervention. Lastly, we contrast these findings with other visual-field functional assessments, highlighting CoORG's unique capability to detect functional deficits in occult outer retinal disease at depth dimension.

6.2 Clinical background and study outline

Scotomas are areas of diminished or lost vision within the visual field, often due to retinal or optic nerve abnormalities. They can vary in size, location, and impact on visual sensitivity[193]. Clinical presentation is assessed with Amsler grids and perimetry; further assessments are done by angiography, FAF, OCT, and multifocal electroretinography (mERG). Acute zonal outer occult retinopathy (AZOOR) is an ocular inflammatory disorder characterized by acquired central/paracentral scotomas and photopsias. The pathophysiology of such scotomas remains unclear, although it is suggested photoreceptor outer segments (OS) may be compromised in zonal outer retinopathies [194,195]. ERG and conventional perimetry assess response aggregates of cells at multiple levels of visual processing and are insufficient for identifying the specific locus of visual pathway compromise. Adaptive optics microperimetry (AOMP) combines cellular-level resolution with retinal tracking for precise scotoma localization[196]. ORG is an emerging, noninvasive measure of light-induced retinal activity[56] and offers a complementary method to localize visual function to specific outer retinal layers. In healthy retinas, the cone ORG shows a rapid decrease in OS length upon stimulus onset, followed by slower OS elongation that saturates in magnitude. The OS contraction is attributed to the early receptor potential consequent to photoisomerization, while elongation is linked to the amplification stages of phototransduction. We present a case of AZOOR where multimodal high-resolution imaging demonstrates the locus of vision loss initiates as early as phototransduction.

6.3 Multimodal structural findings in an advanced-scotoma AZOOR eye

A 79-year-old patient presented with acquired scotomas in the left eye. AZOOR was suspected. Repeated ERGs confirmed progressive vision loss. Figure 6.1 shows FAF, SLO and the

corresponding Spectralis OCT B-scan where a foveal punctate abnormality and peripheral fragmented outer retinal laminations are noted. A commercial AOSLO[197] (Robotrak Inc., China) was used to obtain a high-resolution cellular-scale montage of cone photoreceptors (Figure 6.1D) that demonstrates abnormal cone structure: a) a dark annulus surrounding a central island (Figure 6.1D, lower left) in the confocal image and few clumps of putative cone inner segments in the phase-contrast image (Figure 6.1D, lower right), suggesting abnormal cone waveguiding near the fovea, b) an absence of normal cone packing and reflectivity peripherally.

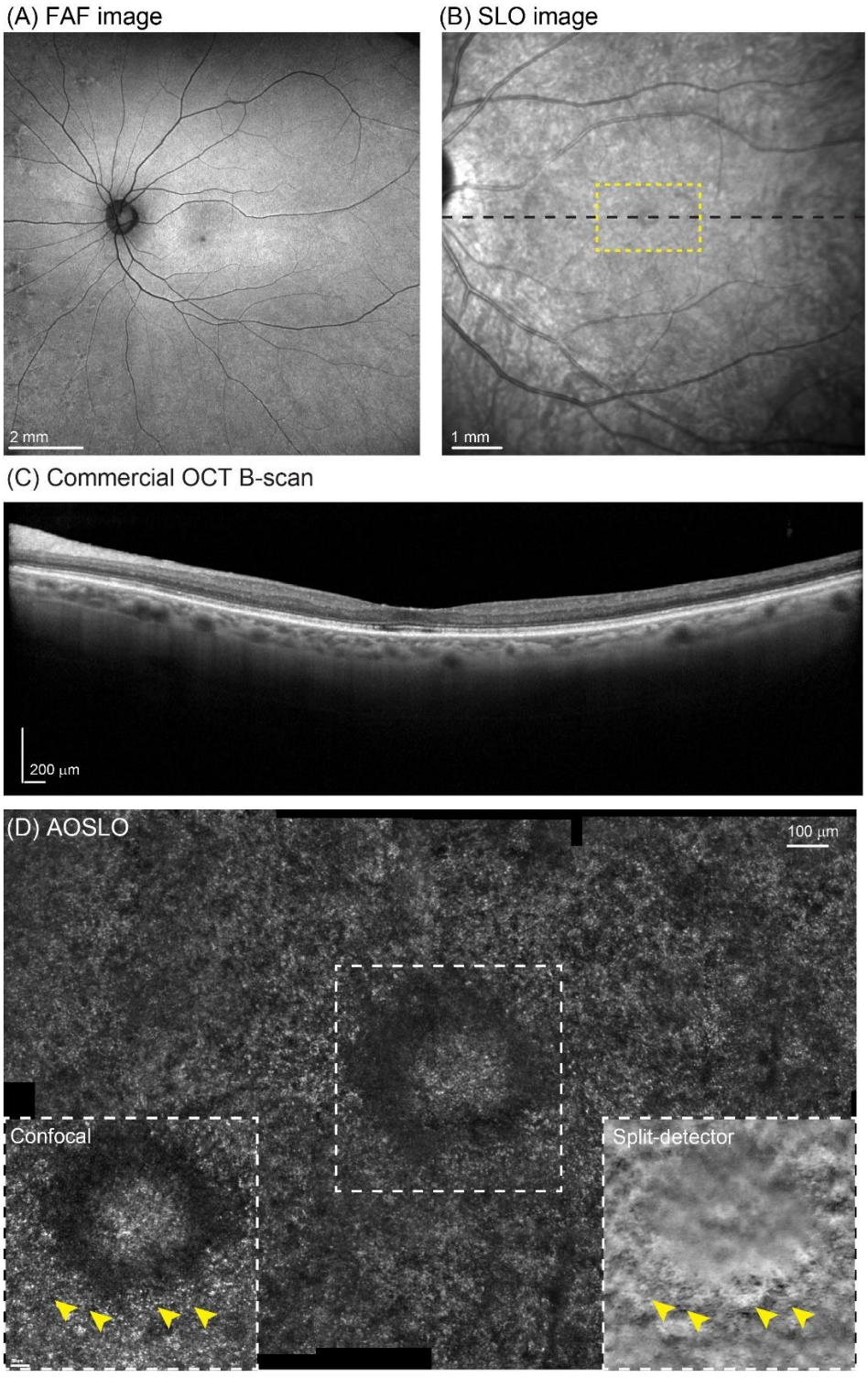


Figure 6.1 Multimodal structural characterization of the AZOOR patient. (A) fundus autofluorescence (FAF), (B) scanning laser ophthalmoscopy (SLO), and (C) OCT B-scan acquired along the black dashed line in (B). Panel (D) shows an AOSLO cone photoreceptor montage

spanning the central 6°. The zoomed-in foveal AOSLO images corresponding to the white dashed rectangle in (D), where both confocal reflectance and non-confocal split-detector (phase-contrast) images are shown in lower left and right, respectively. In the split-detector image, circular structures corresponding to putative inner segments are visible, where corresponding confocal images show ambiguous reflections (yellow arrows).

6.4 Functional assessments with ORG

The macular integrity assessment (MAIA) test revealed lower visual sensitivity and several absolute scotomas (Figure 6.2A) in the macula. The average threshold sensitivity was 7.6 dB (range, 0–36 dB), compared to a normal of 32.9 dB in normal controls [198]. AOMP was used to track the retina in real-time and target seven regions of interest (ROIs) around the fovea with 3 arc-min, 543 ± 11nm stimuli displayed for 200 ms, approximately 74× smaller than a standard perimetry Goldmann III stimulus. Three ROIs within the central island had near-normal sensitivity while four peripheral ROIs showed absolute scotomas, consistent with the MAIA (Figure 6.2A). ORG at the same ROIs within the island of preserved vision indicated a light-evoked increase in cone OS length, but with reduced magnitude and kinetics compared to normal controls (Figure 6.2B). In ROIs where AOMP indicated absolute scotomas, the ORG revealed a light-evoked decrease in cone OS length consistent with normal photoisomerization, but no ensuing elongation attributed to phototransduction amplification. In a normal ORG, the fast-rising elongation phase truncates the early shrinkage, which explains the longer latency of OS contraction observed in the absolute scotoma. This pattern is replicated in the ORG *en face* image (Figure 6.2A), where OS elongation occurs in the central island of preserved vision, while the absolute scotomas showed consistent OS shrinkage. All areas where ORGs are reported also have intact outer retinal structure, with reflections arising from ISOS-EZ, COST and RPE. These observations remained uniform at two visits, spaced 6 months apart.

Reduced ERG a-wave in AZOOR patients suggested that dysfunction in the photoreceptor OS is the dominant cause of vision loss[195]. This study characterizes the fine spatial distribution of vision loss by precisely co-localizing ORG-based functional losses in the photoreceptor layer to reduced sensitivity in the scotoma. Specifically, initial OS shrinkage indicates an intact photoisomerization machinery that is responsible for the early receptor potential[56]. Disrupted phototransduction amplification downstream of photoisomerization is evident by lack of OS elongation in areas of absolute scotomas. ORG is thus an effective tool to delineate the earliest affected stages of the visual pathway in zonal outer retinopathies.

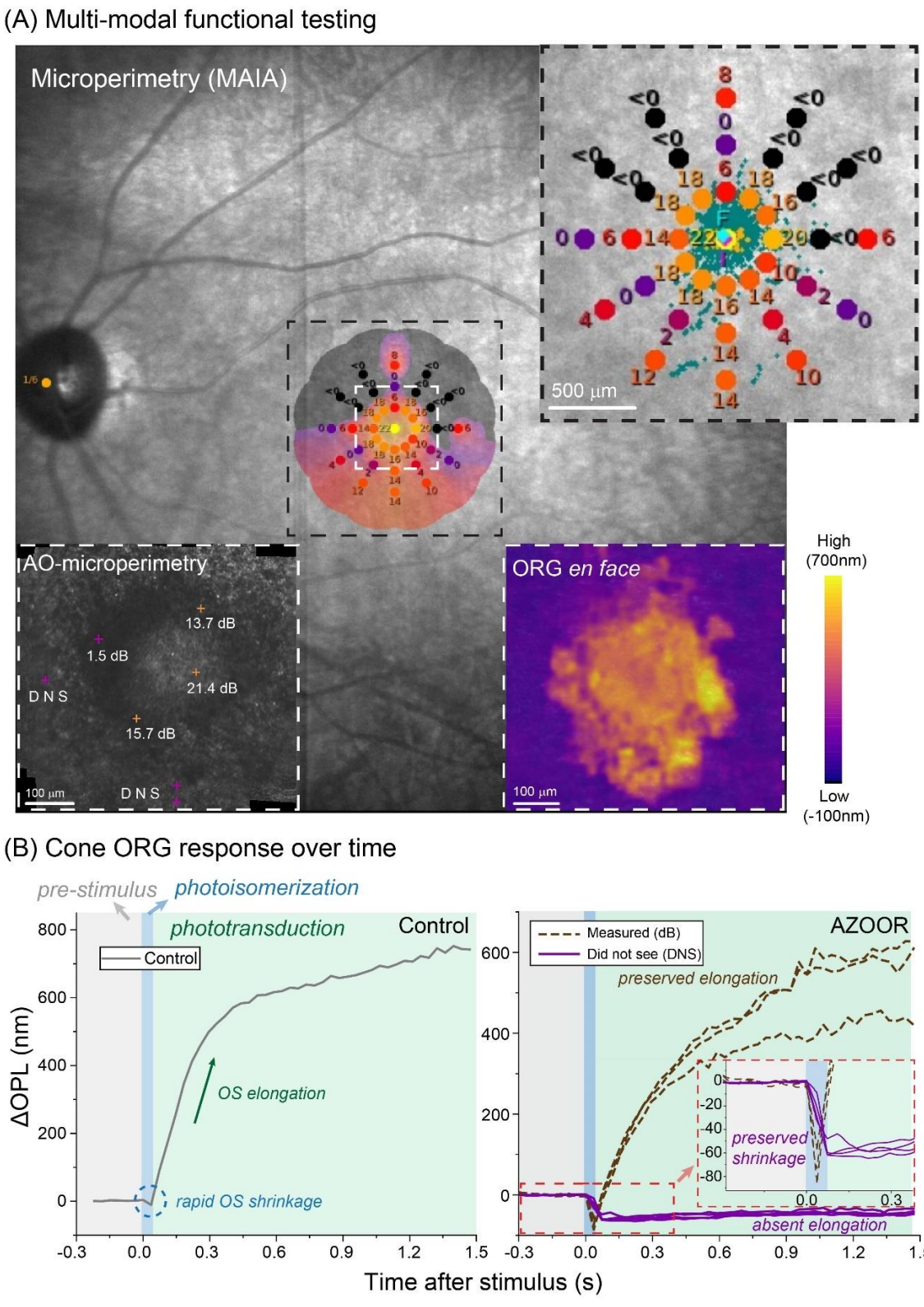


Figure 6.2 Functional characterization of the AZOOR patient. (A) The multi-modal functional testing including MAIA microperimetry sensitivity map; adaptive optics microperimetry (AOMP),

where three orange crosses mark test locations within the central island and four dark purple crosses indicate locations outside the island (DNS: “did not see”); the ORG en face map in same location as AOMP, where ORG magnitude is derived from the saturated amplitude of the last 0.3 seconds of the ORG traces in (B). (B) ORG traces, represented as the change in OS length over time (optical path length, ΔOPL) in a normal control & AZOOR patient for ROIs corresponding to the locations in AOMP of panel A. The ORG traces of ROIs in the central island of the AZOOR patient are indicated by the dashed line. The zoomed-in view of the early OS contraction is inserted into the AZOOR ORG plot. In panel (B), the three distinct stages of the ORG are delineated with shading: pre-stimulus (gray), photoisomerization (blue), and phototransduction (green).

Chapter 7. Conclusions and future work

This dissertation establishes optoretinography as a practical, high-throughput, patient friendly paradigm for functional retinal imaging for basic science and clinical applications. Chapter 2 introduced the CoORG system, a line-scan SD-OCT platform designed without AO, yet capable of achieving micrometer-level axial resolution and nanometer-scale phase sensitivity across a multi-degree imaging field. Rigorous optical power and stimulus calibrations, combined with an automated segmentation and registration pipeline, ensured robust session-to-session repeatability. To address the cellular-level contrast loss inherent to the absence of hardware-based aberration correction, a two-stage digital aberration-correction (DAC) algorithm was developed and validated extensively on synthetic phantoms, AO-based datasets, and in-focus foveal volumes. This DAC algorithm effectively restored cone visibility across the field while preserving phase accuracy, enabling reliable extraction of functional response such as ORG.

Given these advancements, Chapter 3 provided a comprehensive population-level characterization of cone ORG. Repeated measurements in 16 emmetropic adults revealed a quasi-logarithmic scaling of max ΔOPL with retinal photon density and linear scaling with OS length, alongside high within-subject reproducibility (<4% coefficient of variation). Mapping ORG responses across retinal meridians demonstrated a gradual fovea-to-periphery decline consistent with established cone morphology. Age-related attenuation emerged primarily through photon-density reduction. These findings establish a normative atlas against which disease-related deviations can be quantified. Chapters 4 and 5 extended CoORG into inherited retinal degenerations, illustrating its clinical utility in retinitis pigmentosa (RP). CoORG distinguished two distinct functional stages of RP based on transition-zone onset, identified a four-fold reduction in OS length-dependent optical

path length change in advanced disease, and detected longitudinal functional deterioration more sensitively than standard structural measures. These results confirm CoORG's potential as an objective, spatially resolved biomarker of photoreceptor viability.

Furthermore, Chapter 6 presented a case study of acute zonal occult outer retinopathy (AZOOR) characterized by advanced central scotoma, highlighting ORG's clinical value in retinal disorders that exhibit significant functional deficits despite subtle structural changes. In this AZOOR patient, standard visual-field testing revealed a dense central scotoma, yet structural imaging identified discrete regions of preserved cones within the otherwise dysfunctional macular area - boundaries not clearly delineated by conventional OCT alone. ORG traces within these structurally ambiguous zones showed relatively normal photoisomerization responses, yet markedly impaired phototransduction, suggesting selective disruption of photoreceptor function and indicating the locus of vision loss. These findings highlight ORG's unique capability to differentiate partial photoreceptor dysfunction from complete photoreceptor loss in occult outer-retinal diseases.

Collectively, this thesis transitions ORG from an experimental laboratory technique toward a clinically applicable imaging modality. By integrating expanded-field, patient-friendly imaging hardware with sophisticated digital aberration correction and standard quantitative analysis, CoORG bridges the gap between high-resolution photoreceptor physiology and routine ophthalmic care. This technology now supports the generation of normative databases, refined disease staging, and precise longitudinal monitoring, paving the way for future technological advancements, larger epidemiological studies, and targeted mechanistic experiments. Ultimately, these developments position CoORG as a robust, early-stage, functional outcome measure for evaluating emerging retinal therapies.

Having demonstrated the clinical viability and broad applicability of CoORG, the next critical step is to explore further enhancements and novel applications. The following sections outline promising future directions designed to expand CoORG's capability and impact.

Next-generation CoORG system: from refractive to reflective optics. The current CoORG platform, built around a lens-based, line-scan SD-OCT, demonstrated that clinically useful ORG signals can be captured without AO, delivering micrometer axial resolution and nanometer-level phase sensitivity over a 5° field. However, this refractive approach inherently suffers from chromatic focal shifts, Fresnel losses, and limited isoplanatic patches, collectively constraining lateral resolution and signal-to-noise ratio. Analogous to our mirror-based AO-ORG system [63], a natural evolution is to replace refractive lenses with off-axis spherical mirrors, effectively re-engineering the refractive relays into reflective ones. Mirror-based optics offer multiple decisive advantages: zero chromatic aberration, enabling multiple wavelengths (e.g., 840 nm imaging, 980 nm wavefront sensing, and visible stimuli) to share a common focus, no off-axis lens aberrations, thus reducing the need for extensive digital aberration correction; improved photon throughput due to reflective coatings (>97%) and the absence of antireflective surfaces, translating into an ~2 dB gain in laser power and ~15% improvement in ORG SNR; suppression of problematic back-reflections by lens tilting, which eliminates ghost fringes and broadband versatility, enabling straightforward transition to additional wavelengths or alternative OCT modalities. Together, these mirror-based upgrades will offer higher sensitivity, larger imaging field ORG mapping and hybrid OCT imaging modes, without compromising clinical ease-of-use.

Expanding the more biological and clinical scope of CoORG. The next priority is to scale CoORG's clinical utility, both in terms of population diversity and disease scope. The initial normative study established baseline ORG characteristics in a cohort of 16 emmetropic adults,

quantifying how photon density, outer-segment length, and aging modulate cone physiology. Moving forward, a broader normative database comprising at least 150 subjects spanning pediatric (8–18 y), emmetropic adult, high-myopic (>–6 D), and presbyopic (>55 y) groups will be collected. In parallel, we will extend CoORG's applications to diseases lacking reliable functional biomarkers, such as age-related macular degeneration (AMD), where coarse-field ORG can sensitively map emerging dysfunction at drusen margins to guide early interventions. Other inherited conditions, like Stargardt disease with different gene mutations such as in ABCA4[199] and late-infantile neuronal ceroid lipofuscinosis (TPP1)[200], offer opportunities to assess CoORG sensitivity to distinct pathological mechanisms, including lipofuscin-mediated toxicity and lysosomal storage defects. Integration with genetic testing and adaptive-optics microperimetry will further create comprehensive genotype–structure–function atlases, facilitating patient stratification and monitoring for emerging gene and cell therapies. The wide-field, patient-friendly characteristics of CoORG thus make rapid screening and longitudinal monitoring clinically feasible, overcoming limitations inherent to AO-only devices.

Mechanistic insights and advanced stimulation paradigms. Beyond clinical translation, CoORG provides a powerful tool to explore the underlying biophysical mechanisms of the multicomponent ORG waveform. Although this dissertation identified three reproducible ORG phases, Comp0 (a rapid ~2-ms contraction analogous to the early receptor potential) [56], Comp1 (a fast osmotic pressure-induced elongation), and Comp2 (a slower, sustained osmotic swelling)[167,201], their precise molecular origins are still under investigation. Future research will exploit the upgraded mirror-based CoORG optics with advanced stimulation protocols. Paired-flash paradigms, involving a second probe flash delivered shortly after the initial stimulus, will help probe mechanisms of phototransduction and the visual cycle underlying the ORG. Pulse-train

stimulation at varied frequencies (e.g., 1 – 2 Hz) might shed light on differentiate hidden mechanism, elucidating the temporal summation limits of Comp1 and Comp2. Rod-targeted ORG, achieved by shifting stimulus wavelength and imaging eccentric regions beyond 10°, will enable characterization of rods, cells critical for peripheral vision and often the first to degenerate in inherited retinal dystrophies. Multichannel detection enabled by mirror-based optics will permit simultaneous rod–cone recordings, uncovering potential inter-photoreceptor interactions [202]. Such mechanistic insights will transform ORG-derived signals from empirical biomarkers into precise, quantitative readouts of photoreceptor molecular physiology.

BIBLIOGRAPHY

1 Sherman, S. E. in *History of Ophthalmology: Sub auspiciis Academiae Ophthalmologicae Internationalis* 221-228 (Springer, 1989).

2 Besenczi, R., Tóth, J. & Hajdu, A. A review on automatic analysis techniques for color fundus photographs. *Computational and structural biotechnology journal* **14**, 371-384 (2016).

3 Niemeijer, M., Van Ginneken, B., Staal, J., Suttorp-Schulten, M. S. & Abràmoff, M. D. Automatic detection of red lesions in digital color fundus photographs. *IEEE Transactions on medical imaging* **24**, 584-592 (2005).

4 Bernardes, R., Serranho, P. & Lobo, C. Digital ocular fundus imaging: a review. *Ophthalmologica* **226**, 161-181 (2011).

5 Panwar, N. *et al.* Fundus photography in the 21st century—a review of recent technological advances and their implications for worldwide healthcare. *Telemedicine and e-Health* **22**, 198-208 (2016).

6 Yannuzzi, L. A. *et al.* Fluorescein angiography complication survey. *Ophthalmology* **93**, 611-617 (1986).

7 Novotny, H. R. & Alvis, D. L. A method of photographing fluorescence in circulating blood in the human retina. *Circulation* **24**, 82-86 (1961).

8 Zhang, C. & Arditi, D. Automated progress control using laser scanning technology. *Automation in construction* **36**, 108-116 (2013).

9 Marshall, G. F. & Stutz, G. E. *Handbook of optical and laser scanning*. (Taylor & Francis, 2012).

10 Webb, R. H. & Hughes, G. W. Scanning laser ophthalmoscope. *IEEE Transactions on Biomedical Engineering*, 488-492 (2007).

11 Quigley, H. A. & Addicks, E. M. Quantitative studies of retinal nerve fiber layer defects. *Archives of Ophthalmology* **100**, 807-814 (1982).

12 Webb, R. H., Hughes, G. W. & Delori, F. C. Confocal scanning laser ophthalmoscope. *Applied optics* **26**, 1492-1499 (1987).

13 Von Rückmann, A., Fitzke, F. & Bird, A. Distribution of fundus autofluorescence with a scanning laser ophthalmoscope. *British Journal of Ophthalmology* **79**, 407-412 (1995).

14 Schmitz-Valckenberg, S., Holz, F. G., Bird, A. C. & Spaide, R. F. Fundus autofluorescence imaging: review and perspectives. *Retina* **28**, 385-409 (2008).

15 Holz, F. G. *et al.* Progression of geographic atrophy and impact of fundus autofluorescence patterns in age-related macular degeneration. *American journal of ophthalmology* **143**, 463-472. e462 (2007).

16 Owens, S. L. Indocyanine green angiography. *The British journal of ophthalmology* **80**, 263 (1996).

17 Stanga, P. E., Lim, J. I. & Hamilton, P. Indocyanine green angiography in chorioretinal diseases: indications and interpretation: an evidence-based update. *Ophthalmology* **110**, 15-21 (2003).

18 Patel, S. N., Shi, A., Wibbelsman, T. D. & Klufas, M. A. Ultra-widefield retinal imaging: an update on recent advances. *Therapeutic advances in ophthalmology* **12**, 2515841419899495 (2020).

19 Singer, M. *et al.* Ultra-widefield imaging of the peripheral retinal vasculature in normal subjects. *Ophthalmology* **123**, 1053-1059 (2016).
20 Rosser, D., Laidlaw, D. & Murdoch, I. The development of a "reduced logMAR" visual acuity chart for use in routine clinical practice. *British Journal of Ophthalmology* **85**, 432-436 (2001).
21 Holladay, J. T. Visual acuity measurements. *Journal of Cataract & Refractive Surgery* **30**, 287-290 (2004).
22 Johnson, C. A. Psychophysical factors that have been applied to clinical perimetry. *Vision research* **90**, 25-31 (2013).
23 Brown, K. T. The electroretinogram: its components and their origins. *Vision research* **8**, 633-IN636 (1968).
24 Marmor, M. *et al.* ISCEV Standard for full-field clinical electroretinography (2008 update). *Documenta Ophthalmologica* **118**, 69-77 (2009).
25 Sutter, E. E. & Tran, D. The field topography of ERG components in man—I. The photopic luminance response. *Vision research* **32**, 433-446 (1992).
26 Hood, D. C., Odel, J. G., Chen, C. S. & Winn, B. J. The multifocal electroretinogram. *Journal of Neuro-Ophthalmology* **23**, 225-235 (2003).
27 Hood, D. C. *et al.* ISCEV standard for clinical multifocal electroretinography (mfERG)(2011 edition). *Documenta Ophthalmologica* **124**, 1-13 (2012).
28 Creel, D. J. Visually evoked potentials. *Handbook of clinical neurology* **160**, 501-522 (2019).
29 Sincich, L. C., Sabesan, R., Tuten, W. S., Roorda, A. & Harmening, W. M. Functional imaging of cone photoreceptors. *Human color vision*, 71-104 (2016).
30 Tuten, W. S., Tiruveedhula, P. & Roorda, A. Adaptive optics scanning laser ophthalmoscope-based microperimetry. *Optometry and Vision Science* **89**, 563-574 (2012).
31 Grover, S., Fishman, G. A., Anderson, R. J., Alexander, K. R. & Derlacki, D. J. Rate of visual field loss in retinitis pigmentosa. *Ophthalmology* **104**, 460-465 (1997).
32 Berson, E. L., Sandberg, M. A., Rosner, B., Birch, D. G. & Hanson, A. H. Natural course of retinitis pigmentosa over a three-year interval. *American journal of ophthalmology* **99**, 240-251 (1985).
33 Kantola, L., Piccolino, M. & Wade, N. J. The action of light on the retina: Translation and commentary of Holmgren (1866). *Journal of the history of the neurosciences* **28**, 399-415 (2019).
34 Dewar, J. The Physiological Action of Light1. *Nature* **15**, 433-435 (1877).
35 Audiat, J., Auger, D., and Fessard, Á. *C. R. Soc. Biol.* **107**, 1218 (1931).
36 Lüthy, H. The ultraviolet absorption of the living nerve fiber. *Helvetica Physiologica et Pharmacologica Acta* **4**, 20-22 (1946).
37 Hill, D. & Keynes, R. Opacity changes in stimulated nerve. *The Journal of physiology* **108**, 278 (1949).
38 Hill, D. K. The effect of stimulation on the opacity of a crustacean nerve trunk and its relation to fibre diameter. *The Journal of physiology* **111**, 283-303 (1950).
39 Hill, D. The volume change resulting from stimulation of a giant nerve fibre. *The Journal of physiology* **111**, 304 (1950).
40 Cohen, L. B., Keynes, R. & Hille, B. Light scattering and birefringence changes during nerve activity. *Nature* **218**, 438-441 (1968).

41 Cohen, L. B. & Keynes, R. D. Evidence for structural changes during the action potential in nerves from the walking legs of Maia squinado. *The Journal of physiology* **194**, 85-86p (1968).
42 Cohen, L. B. & Keynes, R. D. Changes in light scattering associated with the action potential in crab nerves. *The Journal of physiology* **212**, 259-275 (1971).
43 Hill, B. C., Schubert, E. D., Nokes, M. A. & Michelson, R. P. Laser interferometer measurement of changes in crayfish axon diameter concurrent with action potential. *Science* **196**, 426-428 (1977).
44 Hofmann, K., Uhl, R., Hoffmann, W., Kreutz, W. & mechanism. Measurements of fast light-induced light-scattering and-absorption changes in outer segments of vertebrate light sensitive rod cells. *Biophysics of structure* **2**, 61-77 (1976).
45 Korenbrot, J. I. & Cone, R. A. Dark ionic flux and the effects of light in isolated rod outer segments. *Journal of General Physiology* **60**, 20-45 (1972).
46 Harary, H., Brown, J. & Pinto, L. Rapid light-induced changes in near infrared transmission of rods in Bufo marinus. *Science* **202**, 1083-1085 (1978).
47 Mulligan, J. B., MacLeod, D. I. & Statler, I. C. in *Vision Science and Its Application Topical Meeting.*
48 Liang, J., Williams, D. R. & Miller, D. T. Supernormal vision and high-resolution retinal imaging through adaptive optics. *JOSA A* **14**, 2884-2892 (1997).
49 Roorda, A. & Williams, D. R. The arrangement of the three cone classes in the living human eye. *Nature* **397**, 520-522 (1999).
50 Carroll, J., Kay, D. B., Scoles, D., Dubra, A. & Lombardo, M. Adaptive Optics Retinal Imaging - Clinical Opportunities and Challenges. *Curr Eye Res* **38**, 709-721 (2013).
51 Jonnal, R. S. *et al.* A Review of Adaptive Optics Optical Coherence Tomography: Technical Advances, Scientific Applications, and the FutureReview of Adaptive Optics Optical Coherence Tomography. *Investigative Ophthalmology & Visual Science* **57**, OCT51-OCT68 (2016).
52 Pircher, M. & Zawadzki, R. J. Review of adaptive optics OCT (AO-OCT): principles and applications for retinal imaging [Invited]. *Biomedical optics express* **8**, 2536-2562 (2017).
53 Wynne, N., Carroll, J. & Duncan, J. L. Promises and pitfalls of evaluating retinal diseases with adaptive optics scanning light ophthalmoscopy (AOSLO). *Prog Retin Eye Res*, 100920 (2020).
54 Choma, M. A., Ellerbee, A. K., Yang, C., Creazzo, T. L. & Izatt, J. A. Spectral-domain phase microscopy. *Optics letters* **30**, 1162-1164 (2005).
55 Pandiyan, V. P. *et al.* High-speed adaptive optics line-scan OCT for cellular-resolution optoretinography. *Biomedical optics express* **11**, 5274-5296 (2020).
56 Pandiyan, V. P. *et al.* The optoretinogram reveals the primary steps of phototransduction in the living human eye. *Science advances* **6**, eabc1124 (2020).
57 Liu, Y. *et al.* Ultrafast adaptive optics for imaging the living human eye. *Nature Communications* **15**, 10409 (2024).
58 Lassoued, A. *et al.* Cone photoreceptor dysfunction in retinitis pigmentosa revealed by optoretinography. *Proceedings of the National Academy of Sciences* **118**, e2107444118 (2021).
59 Wendel, B. J. *et al.* Multimodal High-Resolution Imaging in Retinitis Pigmentosa: A Comparison Between Optoretinography, Cone Density, and Visual Sensitivity. *Invest Ophthalmol Vis Sci* **65**, 45 (2024).

60 Cooper, R. F., Tuten, W. S., Dubra, A., Brainard, D. H. & Morgan, J. I. Non-invasive assessment of human cone photoreceptor function. *Biomedical optics express* **8**, 5098-5112 (2017).
61 Cooper, R. F., Brainard, D. H. & Morgan, J. I. Optoretinography of individual human cone photoreceptors. *Optics express* **28**, 39326-39339 (2020).
62 Zhang, F., Kurokawa, K., Lassoued, A., Crowell, J. A. & Miller, D. T. Cone photoreceptor classification in the living human eye from photostimulation-induced phase dynamics. *Proceedings of the National Academy of Sciences* **116**, 7951-7956 (2019).
63 Pandiyan, V. P., Jiang, X., Kuchenbecker, J. A. & Sabesan, R. Reflective mirror-based line-scan adaptive optics OCT for imaging retinal structure and function. *Biomedical optics express* **12**, 5865-5880 (2021).
64 Warner, R., Brainard, D. & Morgan, J. Repeatability and reciprocity of the cone optoretinogram. *Biomedical Optics Express* **13**, 6561-6573 (2022).
65 Gaffney, M., Connor, T. B. & Cooper, R. F. Intensity-based optoretinography reveals sub-clinical deficits in cone function in retinitis pigmentosa. *Frontiers in Ophthalmology* **4** (2024).
66 Xu, P., Cooper, R. F., Jiang, Y. Y. & Morgan, J. I. Parafoveal cone function in choroideremia assessed with adaptive optics optoretinography. *Scientific Reports* **14**, 8339 (2024).
67 Huang, D. *et al.* Optical coherence tomography. *science* **254**, 1178-1181 (1991).
68 Drexler, W. & Fujimoto, J. G. State-of-the-art retinal optical coherence tomography. *Progress in retinal and eye research* **27**, 45-88 (2008).
69 Drexler, W. *et al.* Enhanced visualization of macular pathology with the use of ultrahigh-resolution optical coherence tomography. *Archives of ophthalmology* **121**, 695-706 (2003).
70 Schmitt, J. M. Optical coherence tomography (OCT): a review. *IEEE Journal of selected topics in quantum electronics* **5**, 1205-1215 (2002).
71 Fercher, A. F., Hitzenberger, C. K., Kamp, G. & El-Zaiat, S. Y. Measurement of intraocular distances by backscattering spectral interferometry. *Optics communications* **117**, 43-48 (1995).
72 Häusler, G. & Lindner, M. W. " Coherence radar" and" spectral radar"-new tools for dermatological diagnosis. *Journal of biomedical optics* **3**, 21-31 (1998).
73 De Boer, J. F. *et al.* Improved signal-to-noise ratio in spectral-domain compared with time-domain optical coherence tomography. *Optics letters* **28**, 2067-2069 (2003).
74 Liu, B. & Brezinski, M. E. Theoretical and practical considerations on detection performance of time domain, Fourier domain, and swept source optical coherence tomography. *Journal of biomedical optics* **12**, 044007-044007-044012 (2007).
75 Izatt, J. A. *et al.* Micrometer-scale resolution imaging of the anterior eye in vivo with optical coherence tomography. *Archives of ophthalmology* **112**, 1584-1589 (1994).
76 Pircher, M. & Zawadzki, R. J. Review of adaptive optics OCT (AO-OCT): principles and applications for retinal imaging. *Biomedical optics express* **8**, 2536-2562 (2017).
77 Wojtkowski, M. *et al.* Ultrahigh-resolution, high-speed, Fourier domain optical coherence tomography and methods for dispersion compensation. *Optics express* **12**, 2404-2422 (2004).

78 Zhang, Y. *et al.* High-speed volumetric imaging of cone photoreceptors with adaptive optics spectral-domain optical coherence tomography. *Optics Express* **14**, 4380-4394 (2006).
79 Leitgeb, R. A., Werkmeister, R. M., Blatter, C. & Schmetterer, L. Doppler optical coherence tomography. *Progress in retinal and eye research* **41**, 26-43 (2014).
80 Thouvenin, O., Apelian, C., Nahas, A., Fink, M. & Boccara, C. Full-field optical coherence tomography as a diagnosis tool: recent progress with multimodal imaging. *Applied Sciences* **7**, 236 (2017).
81 Bonin, T., Franke, G., Hagen-Eggert, M., Koch, P. & Hüttmann, G. In vivo Fourier-domain full-field OCT of the human retina with 1.5 million A-lines/s. *Optics letters* **35**, 3432-3434 (2010).
82 Grieve, K. *et al.* Assessment of sentinel node biopsies with full-field optical coherence tomography. *Technology in cancer research & treatment* **15**, 266-274 (2016).
83 Dubois, A., Moneron, G., Grieve, K. & Boccara, A.-C. Three-dimensional cellular-level imaging using full-field optical coherence tomography. *Physics in Medicine & Biology* **49**, 1227 (2004).
84 Scholler, J. *et al.* Dynamic full-field optical coherence tomography: 3D live-imaging of retinal organoids. *Light: Science & Applications* **9**, 140 (2020).
85 Jiang, X., Liu, T., Pandiyan, V. P., Slezak, E. & Sabesan, R. Coarse-scale optoretinography (CoORG) with extended field-of-view for normative characterization. *Biomedical Optics Express* **13**, 5989-6002 (2022).
86 Chen, K., Song, W., Han, L. & Bizheva, K. Powell lens-based line-field spectral domain optical coherence tomography system for cellular resolution imaging of biological tissue. *Biomedical Optics Express* **14**, 2003-2014 (2023).
87 Fechtig, D. J. *et al.* Line-field parallel swept source MHz OCT for structural and functional retinal imaging. *Biomedical optics express* **6**, 716-735 (2015).
88 Fechtig, D. J., Schmoll, T., Grajciar, B., Drexler, W. & Leitgeb, R. A. Line-field parallel swept source interferometric imaging at up to 1 MHz. *Optics Letters* **39**, 5333-5336 (2014).
89 Nienhaus, J. *et al.* Live 4D-OCT denoising with self-supervised deep learning. *Scientific Reports* **13**, 5760 (2023).
90 Norren, D. V. & Vos, J. J. Spectral transmission of the human ocular media. *Vision research* **14**, 1237-1244 (1974).
91 Stockman, A., Sharpe, L. T. & Fach, C. The spectral sensitivity of the human short-wavelength sensitive cones derived from thresholds and color matches. *Vision research* **39**, 2901-2927 (1999).
92 Teng, P.-y. Caserel-an open source software for computer-aided segmentation of retinal layers in optical coherence tomography images. *Zenodo, DOI* **10** (2013).
93 Stevenson, S. B. & Roorda, A. in *Ophthalmic Technologies XV.* 145-151 (SPIE).
94 Liu, Z., Kocaoglu, O. P. & Miller, D. T. 3D imaging of retinal pigment epithelial cells in the living human retina. *Investigative ophthalmology & visual science* **57**, OCT533-OCT543 (2016).
95 Hillmann, D. *et al.* Aberration-free volumetric high-speed imaging of in vivo retina. *Scientific reports* **6**, 35209 (2016).

96 Adie, S. G., Graf, B. W., Ahmad, A., Carney, P. S. & Boppart, S. A. Computational adaptive optics for broadband optical interferometric tomography of biological tissue. *Proceedings of the National Academy of Sciences* **109**, 7175-7180 (2012).
97 St, L. & Wold, S. Analysis of variance (ANOVA). *Chemometrics and intelligent laboratory systems* **6**, 259-272 (1989).
98 Akpek, E. K. & Smith, R. A. Overview of age-related ocular conditions. *Am J Manag Care* **19**, S67-75 (2013).
99 Panda-Jonas, S., Jonas, J. B. & Jakobczyk-Zmija, M. Retinal photoreceptor density decreases with age. *Ophthalmology* **102**, 1853-1859 (1995).
100 Winn, B., Whitaker, D., Elliott, D. B. & Phillips, N. J. Factors affecting light-adapted pupil size in normal human subjects. *Investigative ophthalmology & visual science* **35**, 1132-1137 (1994).
101 Rozema, J. J. & Ní Dhubhghaill, S. Age‐related axial length changes in adults: a review. *Ophthalmic and Physiological Optics* **40**, 710-717 (2020).
102 Ooto, S. *et al.* Effects of age, sex, and axial length on the three-dimensional profile of normal macular layer structures. *Investigative ophthalmology & visual science* **52**, 8769-8779 (2011).
103 Demirkaya, N. *et al.* Effect of age on individual retinal layer thickness in normal eyes as measured with spectral-domain optical coherence tomography. *Investigative ophthalmology & visual science* **54**, 4934-4940 (2013).
104 Maden, G. *et al.* The distribution of the photoreceptor outer segment length in a healthy population. *Journal of Ophthalmology* **2017**, 4641902 (2017).
105 Curcio, C., Millican, C. L., Allen, K. & Kalina, R. Aging of the human photoreceptor mosaic: evidence for selective vulnerability of rods in central retina. *Investigative ophthalmology & visual science* **34**, 3278-3296 (1993).
106 Song, H., Chui, T. Y. P., Zhong, Z., Elsner, A. E. & Burns, S. A. Variation of cone photoreceptor packing density with retinal eccentricity and age. *Investigative ophthalmology & visual science* **52**, 7376-7384 (2011).
107 Kessel, L., Lundeman, J. H., Herbst, K., Andersen, T. V. & Larsen, M. Age-related changes in the transmission properties of the human lens and their relevance to circadian entrainment. *Journal of Cataract & Refractive Surgery* **36**, 308-312 (2010).
108 Richdale, K., Bullimore, M. A. & Zadnik, K. Lens thickness with age and accommodation by optical coherence tomography. *Ophthalmic and Physiological Optics* **28**, 441-447 (2008).
109 Le Goff, M. & Bishop, P. Adult vitreous structure and postnatal changes. *Eye* **22**, 1214-1222 (2008).
110 Kennedy, C. J., Rakoczy, P. E. & Constable, I. J. Lipofuscin of the retinal pigment epithelium: a review. *Eye* **9**, 763-771 (1995).
111 Owsley, C. Aging and vision. *Vision research* **51**, 1610-1622 (2011).
112 Liem, A., Keunen, J., Van Norren, D. & Van de Kraats, J. Rod densitometry in the aging human eye. *Investigative ophthalmology & visual science* **32**, 2676-2682 (1991).
113 Burns, M. E. & Arshavsky, V. Y. Beyond counting photons: trials and trends in vertebrate visual transduction. *Neuron* **48**, 387-401 (2005).
114 Baylor, D. A., Lamb, T. D. & Yau, K.-W. Responses of retinal rods to single photons. *The Journal of physiology* **288**, 613-634 (1979).

115 Hoon, M., Okawa, H., Della Santina, L. & Wong, R. O. Functional architecture of the retina: development and disease. *Progress in retinal and eye research* **42**, 44-84 (2014).
116 Palczewski, K. *et al.* Crystal structure of rhodopsin: AG protein-coupled receptor. *science* **289**, 739-745 (2000).
117 Araque, A., Parpura, V., Sanzgiri, R. P. & Haydon, P. G. Tripartite synapses: glia, the unacknowledged partner. *Trends in neurosciences* **22**, 208-215 (1999).
118 Hillmann, D. *et al.* In vivo optical imaging of physiological responses to photostimulation in human photoreceptors. *Proceedings of the National Academy of Sciences* **113**, 13138-13143 (2016).
119 Zhang, P. *et al.* In vivo optophysiology reveals that G-protein activation triggers osmotic swelling and increased light scattering of rod photoreceptors. *Proceedings of the National Academy of Sciences* **114**, E2937-E2946 (2017).
120 Ma, G., Son, T., Kim, T.-H. & Yao, X. Functional optoretinography: concurrent OCT monitoring of intrinsic signal amplitude and phase dynamics in human photoreceptors. *Biomedical Optics Express* **12**, 2661-2669 (2021).
121 Azimipour, M. *et al.* Optoretinogram: optical measurement of human cone and rod photoreceptor responses to light. *Optics letters* **45**, 4658-4661 (2020).
122 Tomczewski, S. *et al.* Light-adapted flicker optoretinograms captured with a spatio-temporal optical coherence-tomography (STOC-T) system. *Biomedical Optics Express* **13**, 2186-2201 (2022).
123 Wongchaisuwat, N. *et al.* Optical Coherence Tomography Split-Spectrum Amplitude-Decorrelation Optoretinography Detects Early Central Cone Photoreceptor Dysfunction in Retinal Dystrophies. *Translational Vision Science & Technology* **13**, 5-5 (2024).
124 Hee, M. R. *et al.* Optical coherence tomography of the human retina. *Archives of ophthalmology* **113**, 325-332 (1995).
125 Marmor, M. F., Holder, G. E., Seeliger, M. W. & Yamamoto, S. Standard for clinical electroretinography (2004 update). *Documenta ophthalmologica* **108**, 107-114 (2004).
126 Schmitz-Valckenberg, S. *et al.* Fundus autofluorescence imaging. *Progress in retinal and eye research* **81**, 100893 (2021).
127 Hendrickson, A., Possin, D., Vajzovic, L. & Toth, C. A. Histologic development of the human fovea from midgestation to maturity. *American journal of ophthalmology* **154**, 767-778. e762 (2012).
128 Distler, C. & Dreher, Z. Glia cells of the monkey retina—II. Müller cells. *Vision research* **36**, 2381-2394 (1996).
129 Ko, F. *et al.* Associations with retinal pigment epithelium thickness measures in a large cohort: results from the UK Biobank. *Ophthalmology* **124**, 105-117 (2017).
130 Spahr, H. *et al.* Imaging pulse wave propagation in human retinal vessels using full-field swept-source optical coherence tomography. *Optics letters* **40**, 4771-4774 (2015).
131 Dowling, J. E. Foveal receptors of the monkey retina: fine structure. *Science* **147**, 57-59 (1965).
132 Scoles, D. *et al.* In vivo imaging of human cone photoreceptor inner segments. *Investigative ophthalmology & visual science* **55**, 4244-4251 (2014).
133 Hoang, Q., Linsenmeier, R., Chung, C. & Curcio, C. Photoreceptor inner segments in monkey and human retina: mitochondrial density, optics, and regional variation. *Visual neuroscience* **19**, 395-407 (2002).

134 Janel, S. *et al.* Stiffness tomography of eukaryotic intracellular compartments by atomic force microscopy. *Nanoscale* **11**, 10320-10328 (2019).
135 Reichenbach, A. & Bringmann, A. Glia of the human retina. *Glia* **68**, 768-796 (2020).
136 Sunness, J. S. The natural history of geographic atrophy, the advanced atrophic form of age-related macular degeneration. *Mol Vis* **5**, 25 (1999).
137 Sayegh, R. G. *et al.* Geographic atrophy and foveal-sparing changes related to visual acuity in patients with dry age-related macular degeneration over time. *American journal of ophthalmology* **179**, 118-128 (2017).
138 Scoles, D. *et al.* Photoreceptor inner segment morphology in best vitelliform macular dystrophy. *Retina* **37**, 741-748 (2017).
139 Schmetterer, L. *et al.* Endpoints for clinical trials in ophthalmology. *Progress in Retinal and Eye Research* **97**, 101160 (2023).
140 Van Gelder, R. N. *et al.* Regenerative and restorative medicine for eye disease. *Nature medicine* **28**, 1149-1156 (2022).
141 Scalabrino, M. L. *et al.* Late gene therapy limits the restoration of retinal function in a mouse model of retinitis pigmentosa. *Nature Communications* **14**, 8256 (2023).
142 Tao, L. W., Wu, Z., Guymer, R. H. & Luu, C. D. Ellipsoid zone on optical coherence tomography: a review. *Clinical & experimental ophthalmology* **44**, 422-430 (2016).
143 Scoles, D. *et al.* Assessing photoreceptor structure associated with ellipsoid zone disruptions visualized with optical coherence tomography. *Retina* **36**, 91-103 (2016).
144 Birch, D. G. *et al.* Spectral-domain optical coherence tomography measures of outer segment layer progression in patients with X-linked retinitis pigmentosa. *JAMA ophthalmology* **131**, 1143-1150 (2013).
145 Hariri, A. H. *et al.* Quantification of ellipsoid zone changes in retinitis pigmentosa using en face spectral domain–optical coherence tomography. *JAMA ophthalmology* **134**, 628-635 (2016).
146 Birch, D. G. *et al.* Rates of decline in regions of the visual field defined by frequency-domain optical coherence tomography in patients with RPGR-mediated X-linked retinitis pigmentosa. *Ophthalmology* **122**, 833-839 (2015).
147 Delori, F. C. *et al.* In vivo fluorescence of the ocular fundus exhibits retinal pigment epithelium lipofuscin characteristics. *Investigative ophthalmology & visual science* **36**, 718-729 (1995).
148 Robson, A. G. *et al.* Serial imaging and structure-function correlates of high-density rings of fundus autofluorescence in retinitis pigmentosa. *Retina* **31**, 1670-1679 (2011).
149 Cabral, T. *et al.* Retrospective analysis of structural disease progression in retinitis pigmentosa utilizing multimodal imaging. *Scientific Reports* **7**, 10347 (2017).
150 Pole, C. & Ameri, H. Fundus autofluorescence and clinical applications. *Journal of Ophthalmic & Vision Research* **16**, 432 (2021).
151 Cleland, S. C. *et al.* Quantification of geographic atrophy using spectral domain OCT in age-related macular degeneration. *Ophthalmology Retina* **5**, 41-48 (2021).
152 Vámos, R. *et al.* The structure and function of the macula in patients with advanced retinitis pigmentosa. *Investigative ophthalmology & visual science* **52**, 8425-8432 (2011).
153 Ratnam, K., Carroll, J., Porco, T. C., Duncan, J. L. & Roorda, A. Relationship between foveal cone structure and clinical measures of visual function in patients with inherited retinal degenerations. *Investigative ophthalmology & visual science* **54**, 5836-5847 (2013).

154 Battaglia Parodi, M. *et al.* Correlation of SD-OCT findings and visual function in patients with retinitis pigmentosa. *Graefe's Archive for Clinical and Experimental Ophthalmology* **254**, 1275-1279 (2016).
155 Grover, S., Fishman, G. A. & Brown Jr, J. Patterns of visual field progression in patients with retinitis pigmentosa. *Ophthalmology* **105**, 1069-1075 (1998).
156 Holder, G. E. Pattern electroretinography (PERG) and an integrated approach to visual pathway diagnosis. *Progress in retinal and eye research* **20**, 531-561 (2001).
157 Birch, D. G., Anderson, J. L. & Fish, G. E. Yearly rates of rod and cone functional loss in retinitis pigmentosa and cone-rod dystrophy. *Ophthalmology* **106**, 258-268 (1999).
158 Lee, J. Y., Care, R. A., Kastner, D. B., Della Santina, L. & Dunn, F. A. Inhibition, but not excitation, recovers from partial cone loss with greater spatiotemporal integration, synapse density, and frequency. *Cell reports* **38** (2022).
159 Gerth, C., Wright, T., Héon, E. & Westall, C. A. Assessment of central retinal function in patients with advanced retinitis pigmentosa. *Investigative ophthalmology & visual science* **48**, 1312-1318 (2007).
160 Pierce, E. A. *et al.* Gene editing for CEP290-associated retinal degeneration. *N. Engl. J. Med* **390**, 1972-1984 (2024).
161 Lorenz, B. *et al.* Single Center Experience with Voretigene Neparvovec Gene Augmentation Therapy in RPE65 Mutation–Associated Inherited Retinal Degeneration in a Clinical Setting. *Ophthalmology* **131**, 161-178 (2024).
162 Roska, B. & Sahel, J.-A. Restoring vision. *Nature* **557**, 359-367 (2018).
163 Levin, L. A. *et al.* Translational roadmap for regenerative therapies of eye disease. *Med* **4**, 583-590 (2023).
164 Rosin, B., Banin, E. & Sahel, J.-A. Current status of clinical trials design and outcomes in retinal gene therapy. *Cold Spring Harbor Perspectives in Medicine* **14**, a041301 (2024).
165 Cehajic-Kapetanovic, J. *et al.* Initial results from a first-in-human gene therapy trial on X-linked retinitis pigmentosa caused by mutations in RPGR. *Nature Medicine* **26**, 354-359 (2020).
166 Russell, S. *et al.* Efficacy and safety of voretigene neparvovec (AAV2-hRPE65v2) in patients with RPE65-mediated inherited retinal dystrophy: a randomised, controlled, open-label, phase 3 trial. *The Lancet* **390**, 849-860 (2017).
167 Pandiyan, V. P., Nguyen, P. T., Pugh Jr, E. N. & Sabesan, R. Human cone elongation responses can be explained by photoactivated cone opsin and membrane swelling and osmotic response to phosphate produced by RGS9-catalyzed GTPase. *Proceedings of the National Academy of Sciences* **119**, e2202485119 (2022).
168 Busskamp, V., Picaud, S., Sahel, J.-A. & Roska, B. Optogenetic therapy for retinitis pigmentosa. *Gene therapy* **19**, 169-175 (2012).
169 Maguire, A. M., Bennett, J., Aleman, E. M., Leroy, B. P. & Aleman, T. S. Clinical perspective: treating RPE65-associated retinal dystrophy. *Molecular Therapy* **29**, 442-463 (2021).
170 Cai, C. X., Locke, K. G., Ramachandran, R., Birch, D. G. & Hood, D. C. A comparison of progressive loss of the ellipsoid zone (EZ) band in autosomal dominant and x-linked retinitis pigmentosa. *Investigative ophthalmology & visual science* **55**, 7417-7422 (2014).
171 Tee, J. J. *et al.* Natural history study of retinal structure, progression, and symmetry using ellipzoid zone metrics in RPGR-associated retinopathy. *American Journal of Ophthalmology* **198**, 111-123 (2019).

172 Micevych, P. S. *et al.* Cone structure and function in RPGR-and USH2A-associated retinal degeneration. *American journal of ophthalmology* **250**, 1-11 (2023).
173 Hood, D. C. *et al.* Thickness of receptor and post-receptor retinal layers in patients with retinitis pigmentosa measured with frequency-domain optical coherence tomography. *Investigative ophthalmology & visual science* **50**, 2328-2336 (2009).
174 Sayo, A. *et al.* Significant relationship of visual field sensitivity in central 10 to thickness of retinal layers in retinitis pigmentosa. *Investigative Ophthalmology & Visual Science* **59**, 3469-3475 (2018).
175 Sun, L. W. *et al.* Assessing photoreceptor structure in retinitis pigmentosa and Usher syndrome. *Investigative Ophthalmology & Visual Science* **57**, 2428-2442 (2016).
176 Aizawa, S. *et al.* Correlation between visual function and photoreceptor inner/outer segment junction in patients with retinitis pigmentosa. *Eye* **23**, 304-308 (2009).
177 Cideciyan, A. V. & Jacobson, S. G. Negative electroretinograms in retinitis pigmentosa. *Investigative ophthalmology & visual science* **34**, 3253-3263 (1993).
178 Huang, W.-C., Liu, P.-K. & Wang, N.-K. in *Retinitis Pigmentosa* 111-122 (Springer, 2022).
179 Chan, H. & Brown, B. Investigation of retinitis pigmentosa using the multifocal electroretinogram. *Ophthalmic and Physiological Optics* **18**, 335-350 (1998).
180 Sujirakul, T. *et al.* Multimodal imaging of central retinal disease progression in a 2-year mean follow-up of retinitis pigmentosa. *American journal of ophthalmology* **160**, 786-798. e784 (2015).
181 Sullivan, L. S. *et al.* Prevalence of disease-causing mutations in families with autosomal dominant retinitis pigmentosa: a screen of known genes in 200 families. *Investigative ophthalmology & visual science* **47**, 3052-3064 (2006).
182 Smith, T. B. *et al.* Structure-function modeling of optical coherence tomography and standard automated perimetry in the retina of patients with autosomal dominant retinitis pigmentosa. *PLoS One* **11**, e0148022 (2016).
183 Duncan, J. L. *et al.* Baseline visual field findings in the RUSH2A study: associated factors and correlation with other measures of disease severity. *American journal of ophthalmology* **219**, 87-100 (2020).
184 Mitchell, P., Liew, G., Gopinath, B. & Wong, T. Y. Age-related macular degeneration. *The Lancet* **392**, 1147-1159 (2018).
185 Aboshiha, J., Dubis, A. M., Carroll, J., Hardcastle, A. J. & Michaelides, M. The cone dysfunction syndromes. *British Journal of Ophthalmology* **100**, 115-121 (2016).
186 Chew, E. Y. Complement inhibitors for the treatment of geographic atrophy. *The Lancet* **402**, 1396-1398 (2023).
187 Khanani, A. M. *et al.* Efficacy and safety of avacincaptad pegol in patients with geographic atrophy (GATHER2): 12-month results from a randomised, double-masked, phase 3 trial. *The Lancet* **402**, 1449-1458 (2023).
188 Liao, D. S. *et al.* Complement C3 inhibitor pegcetacoplan for geographic atrophy secondary to age-related macular degeneration: a randomized phase 2 trial. *Ophthalmology* **127**, 186-195 (2020).
189 Liu, T. *et al.* Longitudinal changes in optoretinography provide an early and sensitive biomarker of outer retinal disease. *American Journal of Ophthalmology* (2025).
190 Hartong, D. T., Berson, E. L. & Dryja, T. P. Retinitis pigmentosa. *The Lancet* **368**, 1795-1809 (2006).

191 Gass, J. D., Agarwal, A. & Scott, I. U. Acute zonal occult outer retinopathy: a long-term follow-up study. *American journal of ophthalmology* **134**, 329-339 (2002).
192 Monson, D. M. & Smith, J. R. Acute zonal occult outer retinopathy. *Survey of ophthalmology* **56**, 23-35 (2011).
193 Fletcher, D. C. & Schuchard, R. A. Preferred retinal loci relationship to macular scotomas in a low-vision population. *Ophthalmology* **104**, 632-638 (1997).
194 Spaide, R. F., Koizumi, H. & Freund, K. B. Photoreceptor outer segment abnormalities as a cause of blind spot enlargement in acute zonal occult outer retinopathy–complex diseases. *American journal of ophthalmology* **146**, 111-120 (2008).
195 Jacobson, S. G. *et al.* Pattern of retinal dysfunction in acute zonal occult outer retinopathy. *Ophthalmology* **102**, 1187-1198 (1995).
196 Tuten, W. S. *et al.* Visual function at the atrophic border in choroideremia assessed with adaptive optics microperimetry. *Ophthalmology Retina* **3**, 888-899 (2019).
197 Yin, Q. *et al.* A compact fundus image guided adaptive optics scanning laser ophthalmoscope (AOSLO) imaging system with active eye tracking designed for clinical use. *Investigative Ophthalmology & Visual Science* **65**, 3397-3397 (2024).
198 Molina-Martín, A., Piñero, D. P. & Pérez-Cambrodí, R. J. Normal values for microperimetry with the MAIA microperimeter: sensitivity and fixation analysis in healthy adults and children. *European journal of ophthalmology* **27**, 607-613 (2017).
199 Tsybovsky, Y., Molday, R. S. & Palczewski, K. The ATP-binding cassette transporter ABCA4: structural and functional properties and role in retinal disease. *Inflammation and retinal disease: complement biology and pathology*, 105-125 (2010).
200 Gardner, E. *et al.* Mutation update: Review of TPP1 gene variants associated with neuronal ceroid lipofuscinosis CLN2 disease. *Human Mutation* **40**, 1924-1938 (2019).
201 Weiss, C. E., Liu, T., Pandiyan, V. P., Pugh, E. N. & Sabesan, R. Characterizing recovery kinetics of the cone optoretinogram (ORG) with the paired-flash paradigm. *Investigative Ophthalmology & Visual Science* **65**, 3365-3365 (2024).
202 Li, H. *et al.* Optoretinography reveals rapid rod photoreceptor movement upon photoisomerization. *bioRxiv*, 2025.2003. 2022.644466 (2025).